Numerical Simulations of Probes in Magnetised Plasma

Thesis submitted in accordance with the requirements of
the University of Liverpool for the degree of Doctor in Philosophy by

Samuel Stanislaus Murphy-Sugrue

November 2017

Abstract

Langmuir probes are a powerful plasma diagnostic tool, providing highly localised measurements of the plasma potential, electron temperature and plasma density. Accurate measurements of these quantities are required to estimate erosion and sputtering rates of material surfaces, to determine transport rates in the scrape-off layer (SOL) and to provide inputs and boundary conditions for simulation codes modelling the edge plasma. Models have been developed to simulate flush mounted Langmuir probes and ball-pen probes in VSim, a Particle-In-Cell simulation code. These models allow probe measurements of simulated plasmas to be compared to the specified simulation parameters, providing a bridge between theory and experiment.

VSim was used to simulate particle collection by Langmuir probes mounted flush with the surface of the divertor tiles. The influence of the gap in between divertor tiles and the embedded flush mounted probe was studied. Simulations found the gap exposed the side of the probe directly to plasma with the effect of increasing the collection area of the MAST probes by 20 %. Simulated probes were found to overestimate the electron temperature for oblique angles between the magnetic field and the probe surface. This was due to finite electron Larmor orbit effects that enabled electrons to reach the probe surface without the necessary parallel energy to overcome the negative potential of the probe. The extent of this effect was found to depend on the ratio of the electron Larmor radius and the Debye length.

Three dimensional simulations of the ball-pen probe have been carried out for the first time. The ability of the ball-pen probe to make direct plasma potential measurements was tested. It was found that the probe floats at a potential closer to the plasma potential than a standard Langmuir probe, but a measurement of the electron temperature is still required to determine the plasma potential from ball-pen probe measurements. Simulations verified that simultaneous floating measurements from a ball-pen probe and a Langmuir probe can be used to make fast electron temperature measurements. The transport mechanism that allows electrons and ions to reach the recessed collector relies upon E x B drifts. Electrons are able to reflect off the tunnel wall sheath multiple times before arriving at the collector.

The ball-pen probe was tested under a new regime of operation. Various ball-pen probes were used to diagnose a low temperature, strongly magnetised plasma, in which both the ions and electrons were magnetised. Two variations of a 2 mm and 4 mm diameter collector were used, one had a flat design, the other conical. The BPP was found to float at a potential consistently lower than that of an emissive probe. The ball-pen probes reached a peak floating potential once the collectors were recessed inside the tunnel and the ions were magnetised. No significant difference in the value of the peak floating potential was observed, for any collector, once the field strength reached at least 250 mT. As the magnetic field strength increased, the floating potential of the collector was found to be increasingly sensitive to recession depth. The recession depth becomes an import design consideration for ball-pen probes in low temperature plasmas.

Contents

Abstract iii

Contents v

List of Figures ix

List of Tables xv

Acknowledgements xvii

Declaration xix

1 Introduction 1
- 1.1 Introduction . . . 1
- 1.2 Nuclear Fusion . . . 1
- 1.3 Tokamaks . . . 3
  - 1.3.1 Divertor Configuration . . . 4
- 1.4 Diagnostics of the SOL and Divertor . . . 6
- 1.5 Plasma Physics . . . 7
  - 1.5.1 Single Particle Description of a Plasma . . . 8
- 1.6 Thesis Outline . . . 11

2 Langmuir Probes and Sheath Physics 13
- 2.1 Introduction . . . 13
- 2.2 Sheath Physics . . . 14
- 2.3 Ideal Probe Theory . . . 18
- 2.4 The Pre-sheath in Magnetised Plasmas . . . 21
- 2.5 Probes in Magnetised Plasma . . . 23
- 2.6 Langmuir Probes in Tokamaks . . . 29
- 2.7 Underlying Assumptions of Probe Theory . . . 30
- 2.8 Advanced Probe Designs . . . 31
- 2.9 Summary . . . 32

3 Particle In Cell Model 33
- 3.1 Introduction . . . 33
- 3.2 General Method . . . 35
  - 3.2.1 Calculating the Charge Density . . . 38
  - 3.2.2 Calculating the Potential . . . 39

3.2.3 Calculating the Electric Field . . . 40
3.2.4 The Particle Mover . . . 41
3.3 Consquences of the Computational Grid . . . 42
3.3.1 Stability Conditions . . . 42
3.3.2 Finite Sized Particles . . . 43
3.4 Particle Injection . . . 45
3.4.1 Particle Loading and Injection . . . 45
3.4.2 Temperature Conserving Source Function . . . 47
3.4.3 Generating a Velocity from a Source Function . . . 51
3.5 Langmuir Probe Simulations . . . 52
3.5.1 Reproducing Ideal Probe Theory . . . 52
3.5.2 Source Function for Magnetised Plasmas . . . 55
3.5.3 Floating Wall Conditions . . . 57
3.5.4 Assumptions in the Model . . . 58
3.6 Summary . . . 58

4 Flush Mounted Probes on MAST **61**
4.1 Introduction . . . 61
4.2 Overview of FMP theory . . . 62
4.2.1 Summary of Previous Particle-In-Cell Simulations of Flush-Mounted Probes . . . 65
4.3 The Simulation Model . . . 67
4.4 Validating the Model . . . 69
4.5 Incorporating the Gaps . . . 73
4.6 Ion Collection and Estimation of the Electron Density . . . 75
4.7 Electron Collection and Electron Temperature Estimation . . . 78
4.8 Analysing Experimental Data . . . 84
4.9 Discussion . . . 87

5 Ball-Pen Probe Simulations **89**
5.1 Introduction . . . 89
5.2 The Ball-Pen Probe Design and Theory . . . 90
5.3 Empirical Confirmation of the Ball-pen Probe Method . . . 93
5.4 The Simulation Model . . . 96
5.5 Transport Mechanism . . . 98
5.6 Does the Probe Measure the Plasma Potential? . . . 101
5.7 Can the probe be used to make Electron Temperature measurements? . . . 103
5.8 Ball-Pen Probe Design Considerations . . . 103
5.8.1 Effects of Probe Diameter . . . 103
5.8.2 Effect of Probe Recession . . . 105
5.9 Conclusions and Future Work . . . 106

6 Probes in Low Temperature Plasma **109**
6.1 Introduction . . . 109
6.2 Emissive Probe Theory . . . 112
6.3 High Impedance Circuitry for Ball-Pen Probe Floating Potential Measurements . . . 114
6.4 Results . . . 116

6.5 Conclusions 123

7 Conclusions and Future Work **127**
7.1 Conclusions 127
7.2 Future Work 129

Bibliography **131**

List of Figures

1.1 A schematic of a tokamak. Courtesy of the JET image database. 4
1.2 Toroidal cross-section of the currents and subsequent magnetic fields leading to the formation of the X-point. Taken from [8]. 5
1.3 A schematic of the motion of a charged particle in the presence of an external magnetic field with no external electric field. The particle free-streams along the magnetic field and gyrates in the x-y plane perpendicular to the field. . . 9
1.4 The enlargement of the particles orbit as it moves upwards and the contraction as it moves downwards causes the particle to drift in a direction perpendicular to both the electric and magnetic fields. 10

2.1 A schematic of the variation of electric potential, plasma velocity and particle density with distance from the wall in a plasma. Taken from [21]. 15
2.2 A schematic of the I-V curve obtained with a single Langmuir probe. Taken from [27]. 19
2.3 The structure of the sheath in front of a material surface in a magnetised plasma. Particles enter the magnetic pre-sheath with parallel velocity exceeding the Bohm velocity. In the magnetic pre-sheath the particles velocity is turned so that it is sonic perpendicular to the surface on entrance to the Debye sheath. 22
2.4 The probe of dimension d has a collection length associated with it (L_{col}) where $L_{col} >> d$. Taken from [34]. 25
2.5 There are various resistances associated with the probe circuit. Taken from [37]. 26
2.6 The pin-plate probe consisting of a tungsten pin located in front of a tungsten plate. Taken from [37]. 28
2.7 In a strongly magnetised plasma the effective collection area of the probe is reduced from its surface area ($A_{surface}$) to the projection of that surface perpendicular to the magnetic field (A_{proj}). 29
2.8 Various advanced probe designs include: a) The ball-pen probe, taken from [49]; b) The segmented tunnel probe, taken from [47]; c) The retarding field energy analyser, taken from [44] and d) The emmisive probe taken from [114]. 32

3.1 A representation of a two dimensional grid. The particle (grey circle) moves through the domain and deposits charge on the grid points. The area of the rectangle is proportional to the amount of charge deposited at each grid point. 37
3.2 A flow chart of the essential steps of the PIC algorithm 38

3.3 A graphical representation of the Leap-Frog scheme. Particle positions are known at integer time steps while velocities are known at half-integer time steps. 41
3.4 The effective shape of a particle at position x as seen by the grid. At the earlier time the majority of the particles charge is deposited to the X_J grid point as this is the particles nearest grid point. At a later time the particle has advanced and now deposits most of its charge to grid point X_{J+1}. 44
3.5 The velocity distribution of particles generated by the Maxwellian source function. Velocities are expressed in terms of the thermal velocity (v_{th}). . . . 46
3.6 The initial velocity distribution of the particles compared to the final distribution. Velocities for particle injection were sampled from a Maxwellian distribution. 47
3.7 The simulation domain used to determine the temperature conserving source function. Particles born into the source region cannot escape the simulation. Before reflecting off the $x = LS$ plane, source particles are cloned. This clone escapes the source region and replenishes particles lost in the bulk plasma. A slight decline in plasma density is observed outside the source region compared to the density inside the source region. This is due to the effects of the source sheath. 48
3.8 The velocity distribution of particles in different regions of the plasma at the end of the simulation. The Maxwellian distribution is conserved. 49
3.9 The velocity distribution of particles that exit the source region. 50
3.10 The Emmert source function only replenishes the high energy tail of the distribution. It is identical to the distribution of particles that escape the source region. 50
3.11 The domain for the 1D probe simulations used to test the source function. Particles are injected at the injection plane with velocities sampled from the Emmert distribution. 51
3.12 The log of the electron current against probe bias voltage for the Emmert source function. The gradient of the natural log plot is equivalent to the reciprocal of the electron temperature. Using the Emmert source function to inject new particles allows the probe to measure the correct source temperature. 54
3.13 The log of the electron current against probe bias voltage for the Maxwellian source function.The gradient of the natural log plot is equivalent to the reciprocal of the electron temperature. Using the Maxwellian source function to inject new particles results in the probe measuring a temperature that is lower than the specified source temperature. 54

3.14 A comparison of the electron velocity distributions. Red - The distribution of electrons at the beginning of both simulations. Green - The electron distribution at the end of the simulation using a Maxwellian source function. Blue - The electron distribution at the end of the simulation using the Emmert source function. 55
3.15 A typical two dimensional simulation domain. A buffer region of width ≥ 1 ρ_i is added to the start of the simulation to avoid deleting gyrating particles. Particles are injected on the boundary of the buffer region and the simulation domain. 57
3.16 The green circle represents the floating potential and current drained by the probe using the heavy particle floating boundary condition. 58

4.1 A FMP I-V characteristic. Taken from [66]. 62
4.2 Model of the sheath in front of a FMP. Taken from [72]. 64
4.3 A representation of the particle-in-cell simulation domain used to model the particle collection of FMPs. Taken from [73]. 65
4.4 The simulation domain. Particles are injected in the source region to replenish those lost to the wall. The magnetic field makes an angle θ to the probe surface. An additional Larmor buffer region is included to ensure only particles with parallel velocity moving away from the probe are deleted. The red lines, labelled p and w, are the regions where the density is calculated in front of the probe and wall respectively. These densities are shown in figure 4.5. 69
4.5 The ion density (green) and electron density (blue) along a line perpendicular to the wall. Densities are normalised with respect to the density at the entrance to the MPS. Solid lines represent the density in front of the centre of the probe, dashed lines represent the density in front of the floating walls. The vertical lines represent an approximate entrance to the DS, where quasi-neutrality breaks down. 70
4.6 The ion current (green, solid) and electron current (red, dashed) reaching the wall. The currents are normalised by I_0. The edges of the probe are shown in dashed, vertical lines. 71
4.7 The ion density (green, solid) and electron density (blue, dashed) in front of the wall. The densities are normalised by the density at the entrance to the MPS. The edges of the probe are shown in dashed, vertical lines. 72
4.8 The potential profile along the wall. 72
4.9 The ion current collected by the probe at different bias voltages. 73
4.10 The product of parameter a extracted from the I-V characteristic multiplied by $\sqrt{\sin\theta}$ and the length of the probe (in units of λ_D) against $\cot\theta$. 74
4.11 The ion current (green, solid) and electron current (red, dashed) reaching the wall. The currents are normalised by I_0. The edges of the probe (wall) are shown in black (grey), dashed, vertical lines. 74

4.12 The ion density (green, solid) and electron density (blue, dashed) in front of the wall. The densities are normalised by the density at the entrance to the MPS. The edges of the probe (wall) are shown in black (grey), dashed, vertical lines. 75
4.13 The potential structure in front of the wall in a VSim simulation incorporating the gaps. The probe is biased negatively with respect to the surrounding floating walls (shown in grey), therefore the probe's DS is thicker than that of the walls. The thickness of the sheath is exaggerated in this figure due to the difference in scaling of the x and y-axes. 76
4.14 A model of the sheath in front of the FMP. The sheath is modelled as a rectangle. The floating wall has a sheath of thickness Δ_0. For $V_{probe} < V_F$ the probe has an enhanced sheath thickness of Δ and a lateral expansion of δ. 76
4.15 A plot of the ion current as a function of voltage applied to the probe. Top, dashed line represents the ion current in the gap model. Bottom, solid line is the current in the no-gap model. 77
4.16 The product of the sheath expansion parameter a obtained from the I-V characteristic multiplied by the probe length L and the gap length g (both in units of λ_D) and $\sqrt{\sin\theta}$ as a function of $\cot\theta$. 79
4.17 The parallel velocity distribution of electrons that are absorbed by a probe biased -28 V relative to the floating potential. Positive velocities are directed towards the probe. Region A represents electrons that have insufficient parallel energy to reach the probe but are assisted by their gyromotion. Region B is composed of a mixture of electrons that do have sufficient parallel energy to reach the probe and those that reached the probe due to their gyromotion before having time to reflect in the sheath. Region C consists of electrons that would make it to the probe regardless of finite orbit effects. The line between regions B and C is for illustrative purposes only. This boundary is not clearly defined. 80
4.18 A plot of the parallel velocity of an electron that reaches the probe due to finite orbit effects as it moves through the bulk plasma, into the sheath, before reaching the probe surface. The two vertical dashed lines represent a region of width 1 ρ_e away from the probe. The electrons parallel velocity rapidly drops in the sheath, becoming negative within the marked region. At this point its orbital motion brings it to the probe. 81
4.19 The electron temperature is derived from the gradient of the log of the electron current against the probe bias voltage. The solid, red line is obtained by taking the log of the entire electron current reaching the probe. This overestimates the electron temperature. The dashed, blue line is obtained by considering only the portion of the electron current that arrived at the probe with speed $\geq 2v_{th}$. This accurately measures the source temperature. 82

4.20 The relative error in the electron temperature measurement ($T_e^{measured}/T_e^{source}$) as a function of λ_D/ρ_e. 83
4.21 The relative error in the electron temperature measurement ($T_e^{measured}/T_e^{source}$) as a function of θ. The green line is a fitted function of the form $h(\cos\theta/\sqrt{\sin\theta})+1$. Where h is a constant. 84
4.22 Fits to the MAST data for the three models. 86

5.1 A schematic of the initial design of the BPP proposed by Adamek [49]. The probe is orientated such that the axis of the tunnel is perpendicular to the magnetic field. 91
5.2 A BPP with a flat cylindrical collector. Also referred to as a Katsumata-type probe. d is the diameter of the probe and h the retraction depth. 93
5.3 Top: The orginal BPP designs by Adamek. Bottom: Measurements made by the BPP on the CASTOR tokamak. Figure c shows two I-V traces for the probe collector at different recession depths. Figure d displays the floating potential and the measured value of α_{BPP} for the collector as a function of recession depth. Images taken from [49]. 94
5.4 On the left - The BPP simulation domain as viewed from above looking along the x-axis. The collector sits at the bottom of the tunnel (maximum x). On the right - A cross-section of the domain. h is the recession depth. Grey surfaces are floating. The collector can either be biased to a potential or allowed to float. 97
5.5 Electrons and ions orbit in opposite directions. Orbit of the ions takes them deep into the right hand side of the probe. 98
5.6 On the left - cross section of the electric potential. On the right - cross section of the resulting electric field in the z direction. Recession depth, $h = 1.1$ mm. Particles follow the magnetic field lines into and out of the plane shown. Their orbits can take them into contact with the walls, running parallel to the magnetic field, resulting in the potential structure shown. . . 99
5.7 The trajectory of electrons and ions in the x-y plane is shown in green and blue respectively. Red lines show the walls of the probe. The electron follows the field across the periodic simulation domain until it enters the tunnel. Once in the tunnel the electron reflects back and forth due to the sheath potential. Vertical lines represent the electron leaving the simulation on one side of the periodic boundary and re-emerging on the other side. Ions simply travel down the tunnel due to their orbit whilst travelling parallel to the field. $h = 1.1$ mm. 100
5.8 The parallel velocity distribution for electrons at the top and bottom ($h = 1.1$ mm) of the BPP tunnel. The distribution narrows deep into the probe as the more energetic electrons are able to overcome the sheath potential and hit the wall. 100

5.9 The plasma potential across the simulation domain, the dashed line shows the location of the BPP tunnel entrance. 102
5.10 The potential structure across the simulation domain. The floating potential of the probe varies with tunnel diameter as does the value of R. The potential structure near $x = 0$ is a result of the source sheath, an artefact of particle injection in this region. 104

6.1 Schematic of the experimental system equipped with a transparent conductive oxide electrode (TCO), a mass flow controller (MFC), a matching unit (MU), a current sensor (Ip) and a voltage probe (Vp). The plasma was diagnosed with a ball-pen probe (BPP) and an emissive probe. 111
6.2 Schematic of the circuit used to heat the emissive probe and measure the floating potential using a voltage probe (V.P). 114
6.3 Representation of the probe circuit to measure the floating potential. 114
6.4 A potential divider is used to determine the correct floating potential of the probe. 115
6.5 The measured value of the BPP floating potential with increasing resistance of R_2 in the potential divider circuit. As R_2 increases so does the measured floating potential. 115
6.6 The voltage follower circuit used to provide high impedance. This is required in order to make accurate measurements of V_F. 116
6.7 The plasma potential as measured by the emissive probe and the Langmuir probe for a variety of plasma powers and pressures. 117
6.8 The floating potential of the 2 mm tapered BPP collector as a function of recession depth for different field strengths. The circled region represents the peak potential reached by the probe for the magnetic field strengths equal to or above 81 mT. The probe does not operate as a BPP below this field strength. 117
6.9 The floating potential of the 2 mm flat BPP collector as a function of recession depth for different field strengths. The plasma pressure was 0.45 Pa and 9.6 Pa for the left and right plots respectively. 119
6.10 The results of PIC simulations of the BPP with the 2 mm, flat collector. . . 120
6.11 The floating potential of the two 4 mm BPP collectors as a function of recession depth for different field strengths. On the left - floating potentials of the tapered collector. On the right - floating potentials of the flat collector. 120
6.12 The peak floating potential of the various BPP collectors and the emissive probe at different magnetic flux densities. 121
6.13 The current reaching the 2 mm collector at different recession depths for various magnetic field strengths. 122
6.14 I-V curves for the 2 mm collector at different recession depths with a magnetic field strength of 81 mT. Absolute values for the current have been taken. 123

List of Tables

4.1 Typical plasma parameters used in the simulations of FMPs on MAST. . . . 69
4.2 Electron density and temperature values extracted from the MAST data for each model along with a reduced chi-squared value (χ^2_ν) to estimate the goodness of the fit for each model. 87

5.1 Typical plasma parameters used in the simulations of the BPP. 97

6.1 Typical plasma parameters used in the simulations of the BPP. 119

Acknowledgements

Firstly, I would like to thank my two supervisors, James Harrison and James Bradley for their endless enthusiasm and patience. The work presented here would not have been possible without their guidance. I would also like to thank Paul Bryant for the huge amounts of feedback he has provided and the direction he gave to this project.

During the course of my PhD I have been fortunate enough to work with Nick Walkden and Sarah Elmore. Their knowledge and expertise was extremely helpful and led to many fruitful conversations. It was a pleasure to work with Brandon Harris, his experimental expertise enabled the work of Chapter 6.

I would like to thank the EPSRC for funding this PhD and CCFE for providing me with the facilities to carry out my research. I would also like to acknowledge the access I have had to high powered computer facilities. This work made use of the facilities of the N8 HPC Centre of Excellence, provided and funded by the N8 consortium and EPSRC (Grant No.EP/K000225/1). The Centre is co-ordinated by the Universities of Leeds and Manchester.

I have made some great friends amongst the CCFE student community, their presence made CCFE an enjoyable place to work and provided much needed humour and relief throughout the course of my PhD. I would like to thank them for tolerating my puns and pranks and for the interesting lunch time conversations we shared.

Finally, I would like to thank my parents for their unwavering support throughout all my years of education. They taught me to always try my best and to persevere.

Declaration

I declare that the work presented in this thesis, other than contributions cited or acknowledged in the text, is my own.

Samuel Murphy-Sugrue, July 2017.

Chapter 1

Introduction

1.1 Introduction

Rising populations and economic growth in Asia and Africa will lead to a large increase in the global energy demand over the next century. It is projected that there will be a 30% increase in energy demand by 2040, leading to an increase in consumption of all modern fuels [1]. The elevated dependence on fossil fuels is problematic. According to the BP Statistical Review of World Energy [2], known reserves of oil will be depleted by 2066, natural gas by 2069 and coal by the early 22nd century based on 2015 rates of consumption. Not only are fossil fuel reserves dwindling but their continued use is in direct contradiction to global commitments of reducing CO_2 emissions to tackle climate change. Alternative energy sources are required that are both sustainable and low emitters of CO_2. Nuclear fission is a promising solution, producing no CO_2 during operation [3] and with a fuel source that will last over 150 years based on known uranium reserves and current reactor requirements [4]. Fission is capable of providing base load power but its adoption has been hindered by poor public approval, high construction and decommissioning costs and fear of nuclear proliferation. Renewable energy sources such as wind and solar are capable of generating electricity with no CO_2 emissions during operation but have problems with low energy density and intermittency. They can therefore not be relied upon to supply base load power. To date, fission is the only proven technology capable of meeting base load power demands whilst minimising the emissions of greenhouse gases [5]. An abundant energy source is desired that can reliably provide electricity, with low CO_2 emissions and without the risks of nuclear proliferation. This has led to an international effort to develop nuclear fusion as an energy source.

1.2 Nuclear Fusion

Nuclear fusion is a technology with the potential to meet humanity's energy demands, emitting no CO_2 and producing minimal amounts of short lived radioactive waste in the process. Fusion is the process by which two light nuclei combine to form a heavier nucleus and some by-products. At attainable energies of today's machines, the fusion

reaction with the highest probability of occurrence is the reaction between deuterium and tritium, producing a neutron and helium ash as shown below:

$$^{2}_{1}\mathrm{D} + ^{3}_{1}\mathrm{T} \rightarrow ^{4}_{2}\mathrm{He} + ^{1}_{0}\mathrm{n} + 17.6MeV \tag{1.1}$$

The neutron carries the majority of the released energy (14.1 MeV) with the alpha particle carrying the rest. In a fusion power plant the neutron would travel out of the plasma into a blanket that slows and absorbs the neutron, converting it's kinetic energy into heat. This heat would be used to convert water into steam as in a conventional reactor.

Deuterium and tritium are both isotopes of hydrogen, the former found in abundance on Earth whilst the latter can be bred from lithium. Both naturally occurring isotopes of lithium react with neutrons to form tritium as shown below:

$$^{6}_{3}\mathrm{Li} + ^{1}_{0}\mathrm{n} \rightarrow ^{4}_{2}\mathrm{He} + ^{3}_{1}\mathrm{T} + 4.8MeV \tag{1.2}$$

$$^{7}_{3}\mathrm{Li} + ^{1}_{0}\mathrm{n} \rightarrow ^{4}_{2}\mathrm{He} + ^{3}_{1}\mathrm{T} + ^{1}_{0}\mathrm{n} - 2.466MeV \tag{1.3}$$

making lithium an ideal component of the blanket material for breeding tritium. There are enough supplies of deuterium and lithium to provide energy from fusion for millions of years based on current energy demands [6]. Not only is the fuel abundant but only a few grams of it is required to be in the reactor during operation. In the case of loss of control of a fusion reaction, the reaction ceases immediately, there is no capability for a runaway chain reaction to take place. Fusion is therefore inherently safe.

In order for fusion to occur, the fuel must be heated to millions of degrees so that the positively charged nuclei can become sufficiently close to allow the strong nuclear force to overcome the repulsive Coulomb forces. There exist three ways of containing the hot fuel long enough for fusion to occur. The first is gravitational confinement, a process exclusively used in stars, the second is magnetic confinement and the third, inertial confinement. In inertial confinement fusion (ICF), a pellet of fuel is compressed, often by a laser, raising the temperature and density of the fuel so that the conditions required for fusion are met. Magnetic confinement fusion (MCF) uses strong magnetic fields to confine the hot fusion fuel long enough for fusion to occur. The research detailed in this thesis is only relevant to MCF and so the rest of the chapter will focus on this branch of fusion.

In MCF, a gas mixture of deuterium-tritium (DT) fuel is heated to millions of degrees at which point it forms a charged state of matter known as a plasma. The nuclei of the gaseous fuel becomes separated from the electrons, leading to a more complex interaction amongst the particles. These interactions will be described later in the chapter. Numerous techniques have been developed to magnetically confine fusion plasmas such as tokamaks, stellarators, pinch devices, and mirror devices. Of these the tokamak is the most developed and extensively studied.

1.3 Tokamaks

The word tokamak is an abbreviation of a Russian phrase that translates to "Toroidal chamber with magnetic coils". The first tokamak was built at the Kurchatov institute in Moscow and began operating in 1958. Out of all of the approaches to fusion, tokamaks currently hold the world record for highest fusion gain (Q ≈ 0.7) defined as the fusion power output divided by the power used to heat the plasma. This record is held by JET [7]. The worlds largest tokamak, ITER is currently under construction in Saint Paul-lez-Durance, southern France. A huge international project with 35 nations collaborating. It is designed to achieve a net energy gain, producing more energy from fusion than was put in to operate the machine and heat the fuel. If this is achieved it will be a world first. ITER is intended to be a proof of principle device which will pave the way for a commercial demonstration power plant, DEMO.

In order to confine the plasma, a tokamak uses a helical magnetic field. This is formed from the superposition of a toroidal field and a poloidal field. The toroidal field is created by magnetic coils that surround the toroidal chamber. The poloidal field is created by driving a toroidal current through the plasma in addition to toroidal magnetic coils used to control and shape the plasma. The toroidal current creates a poloidal magnetic field that encircles the plasma. The toroidal current is induced in the plasma by a solenoid located at the centre of the torus. Ramping the current in the solenoid produces a time-varying magnetic flux. This time-varying flux then induces a current in the surrounding plasma. The plasma is the secondary coil in the transformer circuit with the solenoid the primary coil. The induced current aids in both plasma confinement and heating. Ohmic heating raises the temperature of the plasma due to it's resistivity, although this effect diminishes at high temperatures, as the electrical resistance of a plasma decreases with increasing temperature. The helical field produced by this superposition is not enough to confine the plasma for adequate amounts of time. Additional poloidal field coils are required in order to stabilise and shape the plasma. A schematic of the magnetic field of a tokamak is shown in figure 1.1.

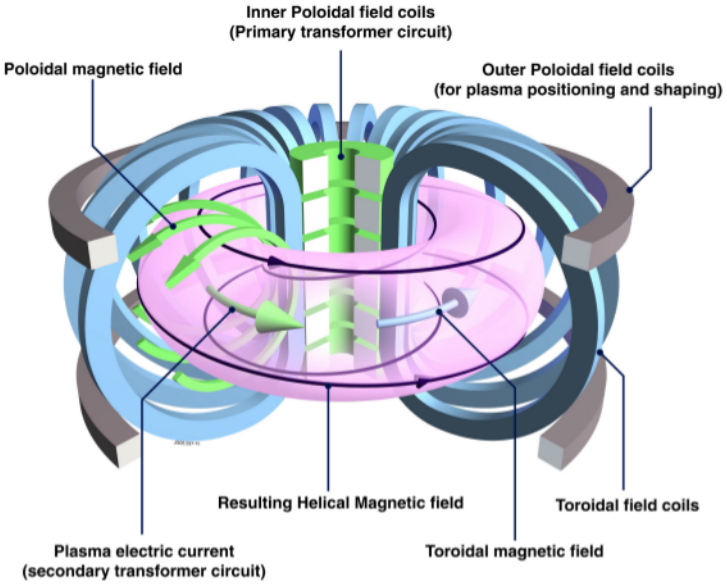

FIGURE 1.1: A schematic of a tokamak. Courtesy of the JET image database.

The charged particles of a fusion plasma are confined to the helical magnetic field lines. In the ideal case of perfect confinement, particles would remain confined to these field lines, encircling the torus without coming into contact with the walls of the tokamak. However, in reality, cross-field transport, driven by collisions, turbulence and particle drifts, causes the plasma to drift outwards towards the walls. Impinging plasma particles can displace atoms in the wall. In order to prevent damage to important vessel components and avoid contamination of the core plasma, the flow of plasma to the surface of the machine must be controlled. Early machines designed part of the first wall to protrude from the surface, deliberately bringing the plasma into contact with a specific part of the wall. This region of the wall was known as the limiter. Although limiter based tokamaks were able to control where the damage to the wall was occurring, they were still hindered by the ease at which impurities from the limiter could enter the bulk plasma. Impurities act to lower the plasma temperature by radiative cooling. A partially ionised impurity ion will radiate away energy as trapped electrons complete energy transitions. Reducing levels of impurities in the core, especially high Z impurities, is crucial to maintaining sufficiently high temperatures for fusion to occur. An alternative to the limiter was sought, which led to the development of the divertor.

1.3.1 Divertor Configuration

A divertor is a region of the tokamak where the plasma is intentionally brought into contact with the vessel wall in a controlled manner. This is advantageous as it allows the plasma-surface interaction to occur far away from the core plasma, reducing the probability of impurities reaching the core plasma [8]. A divertor relies upon the creation of an X-point in the plasma, a null point in the poloidal field. This null point is created

by running a current in the same direction as the toroidal plasma current. This current also creates a poloidal field which interacts with the plasma poloidal field to create a small region of null field. A schematic for the fields responsible for the X-point are shown in figure 1.2.

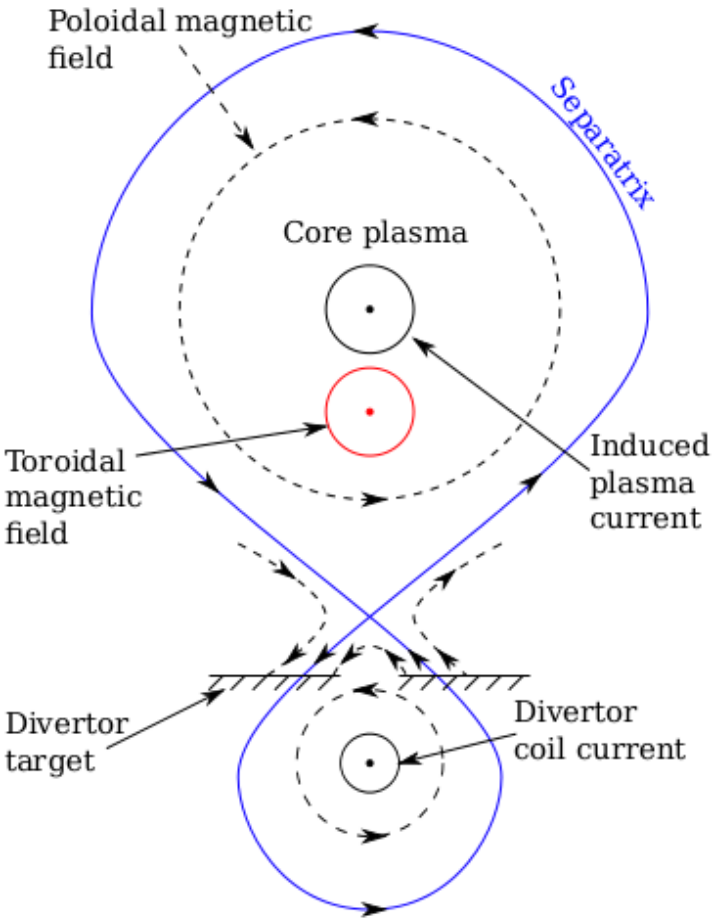

FIGURE 1.2: Toroidal cross-section of the currents and subsequent magnetic fields leading to the formation of the X-point. Taken from [8].

Particles begin in the core plasma and follow closed magnetic field lines that do not end on a material surface. Cross-field transport drives particles outwards towards the vessel walls. The separatrix defines the boundary between open and closed magnetic field lines. Particles that travel beyond the separatrix now follow open field lines. These field lines end on a material surface. This region of open field lines is called the Scrape-Off-Layer (SOL). In the case of a diverted tokamak, these field lines will take the particles to the divertor target. The target is a material surface situated on the lower legs of the X-point. The target can be designed to tolerate the high flux of heat and particles from the impinging plasma. As well as constraining the plasma exhaust to a limited region of the machine and reducing impurity build up in the core, the divertor configuration also allows the tokamak plasma to operate in high confinement mode (H-mode). This

is a regime of reduced particle transport, allowing the core to obtain a higher plasma pressure [9] which could lead to increased energy production from a fusion power plant.

1.4 Diagnostics of the SOL and Divertor

The SOL is the boundary layer between the core plasma and the material surface of the tokamak wall. Early fusion experiments focused on the core plasma, where the fusion reactions take place, with the edge a secondary concern. However, it was soon realised that understanding the physics of the edge plasma was crucial to achieving a sustained fusion reaction [10]. Particle transport in the SOL governs the levels of impurities reaching the core plasma from the material surface. It also regulates the levels of fusion ashes (mostly helium) in the core plasma. This by-product of the fusion reaction must be removed from the core plasma to avoid dilution of the fusion fuel. Another crucial role of the SOL is determining the heat load on to the tokamak walls. At present, no material is capable of surviving the predicted heat and particle loads reaching the wall of DEMO and beyond that, an operational fusion power plant [11]. If fusion is to become a commercial success, this problem must be overcome. This challenge is being tackled from two angles. From the material science side, new materials, such as composites are being developed that have properties enabling them to survive the harsh conditions of a fusion reactor. Low activation materials, resistant to erosion and able to tolerate high heat loads are required. Walls that are able to self-heal such as liquid metal walls are also being investigated as a potential solution [11]. As well as developing materials that can handle such extreme conditions, alternative divertor configurations are being explored that aim to reduce heat and particle loads on to the divertor surface, thus easing the demands placed upon the materials. The Super-X divertor configuration aims to reduce power loads to the divertor target by extending the length of the divertor legs below the X-point [12]. This increases the connection length, a measure of the distance along the magnetic field between a point upstream where a plasma particle enters the SOL, to a point downstream where the open field line closes on the divertor target. Increasing the time it takes the plasma to reach the divertor is advantageous as it increases the capability of radiative cooling to reduce the plasma temperature before it hits the divertor target. The theoretical prediction of reduced target power load using the Super-X configuration is backed up by detailed SOLPS simulations [13]. This configuration will be tested on MAST-Upgrade, which will begin operations in 2018.

The edge region of the tokamak is clearly of importance and the physics of it must be understood. A wide range of edge diagnostics have been developed in order to measure the plasma conditions, including probe diagnostics, optical systems, spectroscopic instruments and bolometers. Of these, the most frequently employed are Langmuir probes. A Langmuir probe is a small electrode, placed into contact with the plasma, that is biased to a potential by an external circuit. The bias voltage applied to the probe is swept and the current the probe drains from the plasma at each voltage is

recorded. These measurements allow the local electron density (n_e) and electron temperature (T_e) to be determined. Optical diagnostics include Thomson Scattering (TS), optical cameras and infra-red cameras. TS provides electron temperature and density measurements by using the dipole radiation emitted from the electrons as they move in an oscillating electric field produced by a high power laser sent into the plasma. The scattered light is collected and used to diagnose the plasma. This light is a broadened line centred around the original laser wavelength. The width of the broadening gives a measure of the electron temperature and the area under the spectrum gives the electron density. Optical and infra-red cameras are used to track the motion of filaments and dust particles in the plasma, infra-red cameras can also be used to measure the heat flux to the divertor target. Spectroscopic instruments interrogate the radiation leaving the plasma in the visible to x-ray region and provide information on the impurities present in the plasma, as well as ion temperature measurements. Bolometric systems are frequently used to measure the total radiated power from the divertor plasma. Langmuir probes will be the focus of this thesis. More information about Langmuir probes can be found in Chapter 2.

1.5 Plasma Physics

Plasma constitutes the vast majority of matter in the known universe, it is the main component of the stars and fills the interstellar medium between them. It is estimated that around 97 $\rightarrow$ 99% of standard (non-dark) matter exists in the plasma state [14] but plasma is not so abundant on Earth. The reason for this can be seen from the Saha equation which describes approximately the expected fraction of ionisation for a gas in thermal equilibrium at a given temperature T due to ionising collisions [14]:

$$\frac{n_i}{n_n} \approx 2.4 \times 10^{21} \frac{T^{3/2}}{n_i} \exp\left[-\frac{\epsilon_i}{k_B T}\right] \tag{1.4}$$

where $n_{i,n}$ is the number density of ions and neutrals, ϵ_i is the ionisation energy and k_B is Boltzmann's constant. For typical conditions on Earth, nitrogen in the air has a density of roughly 3×10^{25} m^{-3}, a temperature of 300 K and an ionisation energy of 14.5 eV. At these conditions, the approximate fraction of ionised nitrogen atoms is then a negligible amount

$$\frac{n_i}{n_n} \approx 10^{-122} \tag{1.5}$$

In order for fusion to occur, temperatures inside a tokamak must exceed 10 MK. At these high temperatures the fuel is sufficiently ionised to adopt the plasma state. The plasma state is defined as a collection of ions, electrons and neutral particles that exhibit collective behaviour due to long range Coulomb forces that act between the charged particles. Despite being composed of charged particles, the plasma as a whole remains approximately neutral. This is true on large scales as the number of electrons present in the plasma is equal to the positive charge of the ions that lost the electrons during

ionisation. It is also true on small scales as any charge imbalances that are brought about by random thermal fluctuations are quickly neutralised by the movement of the electrons. The low mass of the electron means it is able to respond very quickly to any charge imbalances, either moving towards regions of net positive charge or being repelled away from regions of net negative charge. This approximate neutrality is a property of the plasma known as quasineutrality.

1.5.1 Single Particle Description of a Plasma

The most fundamental way to describe a plasma is to examine the trajectories of individual plasma particles as they respond to electric and magnetic fields. Charged particles in electromagnetic fields experience a Lorentz force (F_L) and hence their motion can be described by

$$m_i \frac{d\mathbf{v}_i}{dt} \;=\; \mathbf{F}_L \;=\; q_i(\mathbf{E} + \mathbf{v}_i \times \mathbf{B}) \tag{1.6}$$

For the straightforward case with no electric fields present and a magnetic field orientated along the z-axis the motion can be broken into components

$$m\dot{v_x} = qBv_y \quad m\dot{v_y} = -qBv_x \quad m\dot{v_z} = 0 \tag{1.7}$$

The particle streams along the magnetic field with a velocity $v_\parallel$ while the x and y velocity components are coupled together. By taking derivatives of equation 1.7 it is possible to decouple the components perpendicular to the magnetic field.

$$\ddot{v_x} = -\left(\frac{qB}{m}\right)^2 v_x \quad = -\omega_c^2 v_x \tag{1.8}$$

where ω_c is the cyclotron frequency at which the charged particle gyrates around the magnetic field line. Taking real solutions gives

$$\begin{aligned} v_x &= v_\perp \cos \omega_c t \\ v_y &= v_\perp \sin \omega_c t \end{aligned} \tag{1.9}$$

where the equation for v_y is obtained by solving equation 1.8 and substituting the solution into equation 1.7. Integrating these equations then gives the trajectory of the particles

$$\begin{aligned} x &= x_0 + \frac{v_\perp}{\omega_c} \sin \omega_c t \\ y &= y_0 - \frac{v_\perp}{\omega_c} \cos \omega_c t \\ z &= z_0 + v_\parallel t \end{aligned} \tag{1.10}$$

The particles travel parallel to the magnetic field lines whilst performing orbital motion around the field with a radius equal to the Larmor radius (ρ_L) where

$$\rho_L = \frac{v_\perp}{\omega_c} \quad = \frac{v_\perp m}{qB} \tag{1.11}$$

The ions and electrons orbit around a guiding center, a fixed point (x_0, y_0, z_0) as shown in figure 1.3. The particles gyrate in a direction such that the generated magnetic field from the particle motion opposes the applied magnetic field. Hence the ions and electrons orbit the field in different directions due to their opposing charges and at different frequencies due to their relative mass difference, the ions having the larger orbit.

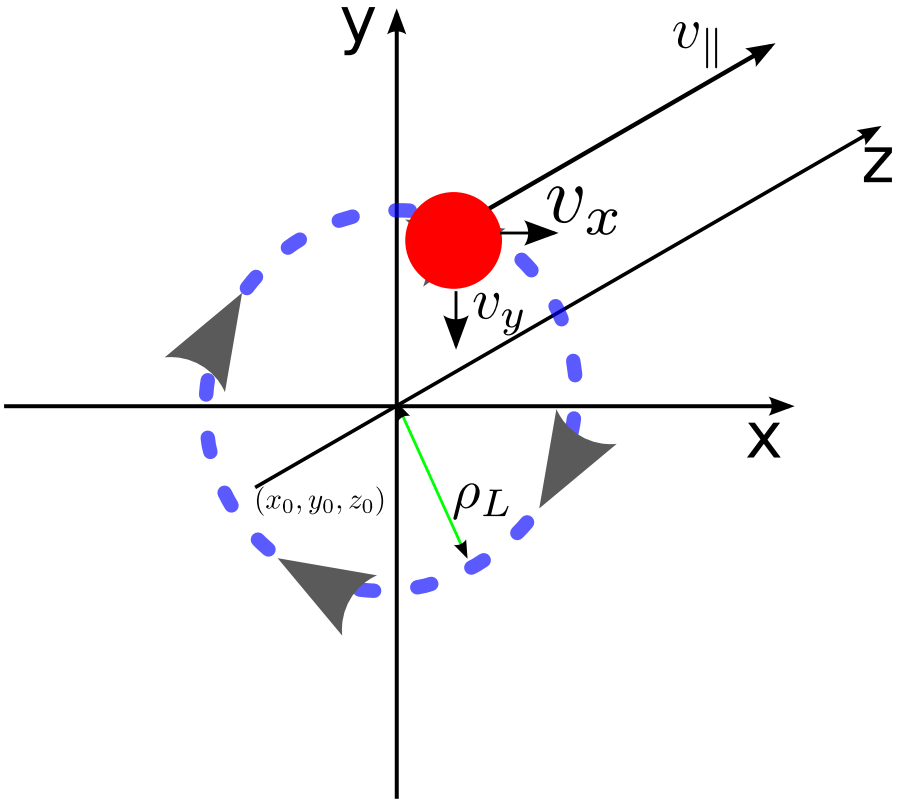

FIGURE 1.3: A schematic of the motion of a charged particle in the presence of an external magnetic field with no external electric field. The particle free-streams along the magnetic field and gyrates in the x-y plane perpendicular to the field.

The free streaming of particles along the magnetic field lines combined with their Larmor orbits give the particles a helical trajectory. The presence of other external forces such as gravity, an applied electric field or a gradient in the magnetic field can cause the guiding center of the particles to drift. The motion of the particles is then composed of the usual gyration around field lines plus an additional drift term of the guiding center. This can be seen by introducing an electric field along the x-axis, perpendicular to the

magnetic field. We now have

$$\begin{aligned} \ddot{v_x} &= \omega_c \dot{v_y} = -\omega_c^2 v_x \\ \ddot{v_y} &= -\omega_c \dot{v_x} = -\omega_c^2 \left(\frac{E_x}{B} + v_y \right) \end{aligned} \tag{1.12}$$

Solving the second order differential equation for v_y gives

$$v_y = v_\perp \sin \omega_c t + \frac{E_x}{B} \tag{1.13}$$

The y velocity now consists of two parts, the original Larmor motion of the particle plus an additional drift of it's guiding centre, perpendicular to both the applied magnetic field and the electric field acting on the particle. The drift motion of the guiding centre due to an electric field is called an E x B drift. Physically this drift arises as the charged particle is accelerated by the electric field during the upward half of it's orbit, increasing the Larmor radius and de-accelerated during the downward swing of its orbit, reducing the Larmor radius. The continuous expansion and contraction of the particles orbit causes it to drift, this is illustrated in figure 1.4.

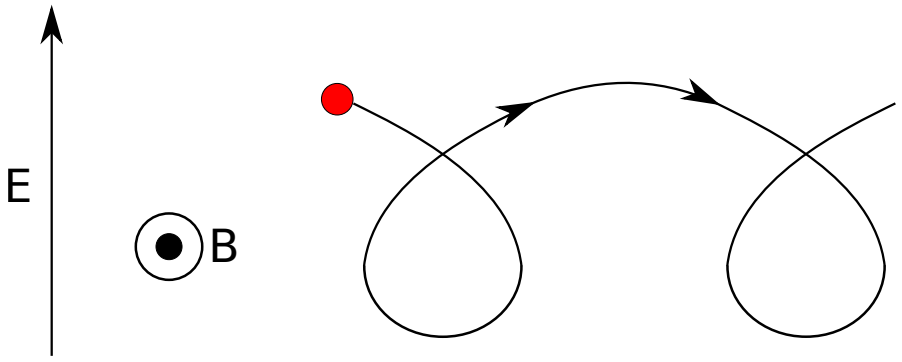

FIGURE 1.4: The enlargement of the particles orbit as it moves upwards and the contraction as it moves downwards causes the particle to drift in a direction perpendicular to both the electric and magnetic fields.

The drift speed and direction is independent of the particles charge and mass. The ions and electrons orbit the field lines in opposite directions but also gain energy and lose energy from the electric field in opposite directions and so both species drift in the same direction. Therefore there is no net current created by the E x B drift.

A complete description of the plasma would be obtained by taking into account the interactions between each particle and every other particle in the system and then by solving equation 1.6 for every particle. However, it is not feasible to carry out this many calculations on even the most powerful of todays supercomputers, even for a very sparse plasma. In order to model a plasma, a statistical formulation is required and so the phase space distribution function, $f_{(x,v,t)}$ is introduced. This distribution function represents the probability density of finding a particle with position x and velocity v at time t. The evolution of the phase space distribution function for a collisionless plasma

is governed by the Vlasov equation

$$\frac{\partial f}{\partial t} + \mathbf{v} \cdot \nabla f + \frac{q}{m}(\mathbf{E} + \mathbf{v} \times \mathbf{B}) \cdot \nabla_v f = 0 \tag{1.14}$$

Solving this equation, or equations derived from it, is the principal aim of many codes designed to simulate the behaviour of a plasma in order to test theoretical models and guide experimental work. Numerical solutions to this equation require discretisation techniques to represent the continuous spatial domain of a plasma on a computer. Various approaches to the numerical solution of the Vlasov equation have been developed. These are discussed further in Chapter 3.

1.6 Thesis Outline

The remainder of this thesis is outlined as follows. Chapter 2 reviews the physics of the sheath and Langmuir probe theory. The complications in the interpretation of Langmuir probe data that arise in the presence of a magnetic field are detailed. Chapter 3 describes the Particle-In-Cell methodology and introduces the simulation model, created in the VSim simulation code, which was used to carry out the work presented in subsequent chapters. Chapter 4 provides an overview of flush-mounted probe theory and presents a series of simulations used to investigate the effect of a gap in between the probe and the divertor tiles. The capability of the ball-pen probe to make direct plasma potential and electron temperature measurements is investigated in Chapter 5. Chapter 6 presents results from experiments carried out in a low temperature, strongly magnetised plasma. Ball-pen probes and an emissive probe were used to make measurements of the plasma potential. The main conclusions of this work are summarised in Chapter 7 which also details possible extensions to this work.

Chapter 2

Langmuir Probes and Sheath Physics

2.1 Introduction

Langmuir probes are the oldest type of plasma diagnostic device and are still one of the most frequently employed tools used to obtain information about conditions inside a plasma. In relation to tokamaks, Langmuir probes are the most reported edge diagnostic in the literature [15]. The main advantage of using probes is that they can make highly localised measurements, almost all other diagnostics give volume averaged measurements. Readings from Langmuir probes are an essential input into simulation codes that aim to simulate the edge region of a tokamak, as the probes measure plasma conditions at solid surfaces, which is typically the most important output from modelling codes. These codes require inputs with high spatial and temporal resolution [16]. The probes take their name from the Nobel prize winning scientist Irving Langmuir [17] who coined the term plasma and whose paper published in 1926 with H.M. Mott-Smith provided a means to measure plasma parameters by obtaining a Current-Voltage curve (I-V curve) using a probe [18]. The probe in its simplest form is a metallic electrode, electrically biased with respect to a reference electrode which is then inserted into a plasma to draw an ion or electron current. Electrical probes are used to diagnose a wide range of plasmas from space plasmas with low-density and weak magnetic fields to those at the edge of nuclear fusion devices with hostile conditions to material surfaces and strong magnetic fields. The use of probes requires direct contact to be made between the probe and the plasma and so their use is limited by the conditions in which they can survive. This restricts the use of probes to the edge of tokamak devices where the plasma is less dense and cooler [19].

Langmuir probes are a powerful diagnostic capable of providing local measurements of the plasma potential (Ψ), electron density (n_e) and electron temperature (T_e) with a good time resolution of approximately 10^{-3} seconds [20]. They are fairly easy both to design and build and acquiring data from them is straightforward. Despite their

simplicity in construction and operation, probes do have a downside compared to other diagnostics. As probes are in contact with the plasma, they perturb it, changing the local density and potential in the surrounding plasma. This complicates the interpretation of probe data. The role of probe theory is to determine the unperturbed values of the plasma which would exist in the absence of the probe. However theoretical models used to interpret the data can be very complicated and in some cases non-existent. No general model exists that is capable of relating the measured current-voltage curves with the actual plasma properties under all possible physical conditions. An overview of the general probe method will be given followed by complications that arise, specifically in the presence of magnetic fields.

2.2 Sheath Physics

In order to understand particle collection by a Langmuir probe it is essential to realise the role played by the plasma sheath. An electrostatic sheath forms whenever a material object comes into contact with a plasma. The sheath dominates the transport of ions and electrons to the material surface [21]. The difference in mobility between electrons and ions is the foundation for the formation of a sheath. For example, consider the case of a divertor tile coming into contact with plasma. Before contact with the plasma, there is no net charge on the tile, the tile is neutral. As the plasma reaches the tile, electrons in the plasma will rush to the tile ahead of the ions. This occurs because electrons are much less massive than ions and so move around much faster in the plasma. This process can not go on indefinitely. A net negative charge builds up on the tile which leads to the formation of a potential barrier. This barrier repels electrons and attracts ions [22]. The potential barrier continues to increase, reducing the electron flux until a steady state is obtained once the electron flux becomes equal to the ion flux. The potential of the tile at steady state is the floating potential (V_F). The tile is said to be floating. The potential a floating object reaches depends on the plasma potential, the temperature of the electrons and ions and the mass ratio of the charged particles. This will be derived in section 2.3.

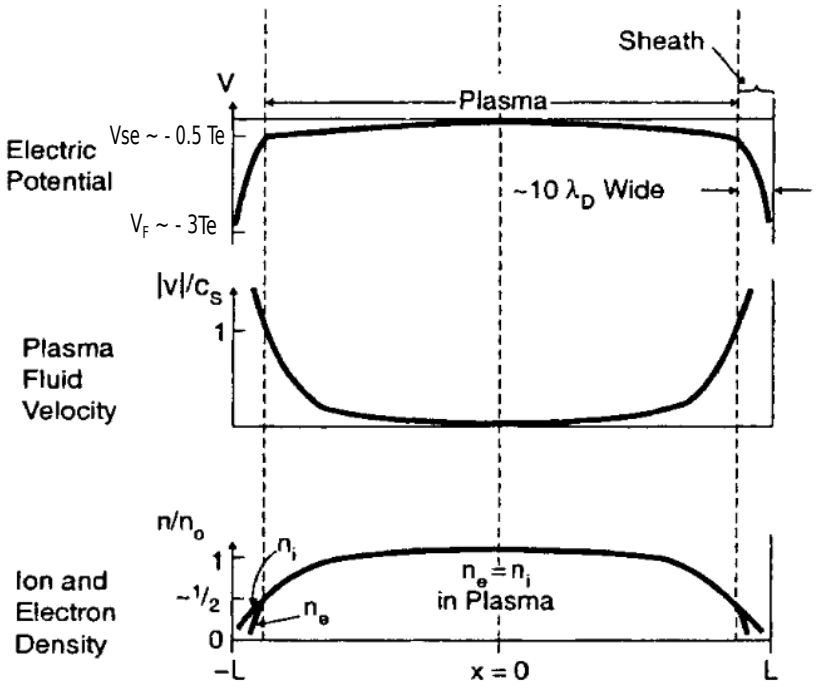

FIGURE 2.1: A schematic of the variation of electric potential, plasma velocity and particle density with distance from the wall in a plasma. Taken from [21].

The floating tile is a region of charge in an otherwise quasineutral plasma. The behaviour of the plasma in response to the presence of this charge is governed by the Poisson equation [23]

$$\nabla^2\psi = -\frac{e}{\epsilon_0}(n_i - n_e) \tag{2.1}$$

where ψ is the potential at a given point in the plasma, e the electron charge, n_i the ion density, assuming singly charged ions and n_e the electron density. The electrons mobility allows them to react quickly to the charge and they adopt a Boltzmann distribution

$$n_e = n_\infty \exp\left(\frac{\psi}{T_e}\right) \tag{2.2}$$

where n_∞ is the plasma density in the bulk plasma, for both electrons and ions, far from the external charge and T_e is the electron temperature in eV. ψ is the potential relative to the plasma potential at the location of n_∞. Over fast timescales the ions can be considered stationary. Substituting equation 2.2 into equation 2.1 gives

$$\nabla^2\psi = -\frac{en_i}{\epsilon_0}\left(1 - \exp\left(\frac{\psi}{T_e}\right)\right) \tag{2.3}$$

By expanding the exponential term and asssuming $T_e >> \psi$ we find

$$\nabla^2\psi \approx \frac{en_i}{\epsilon_0 T_e}\psi = \frac{\psi}{\lambda_D^2} \tag{2.4}$$

where λ_D is the Debye length. Expanding equation 2.4 we find

$$\psi = \psi_0 \exp\left(-\frac{x}{\lambda_D}\right) \tag{2.5}$$

where x is the distance from the charge. The potential of the charge drops off exponentially with distance into the plasma. The Debye length is then the distance over which the charge can penetrate into the plasma. This thin layer where the potential from the charge is able to influence the plasma is known as the sheath. The sheath is a transition layer in the plasma between an external charge and the bulk plasma. In the sheath, quasineutrality no longer holds. The sheath acts to shield the rest of the plasma from the external charge. In the case of a floating tile, with potential negative with respect to the plasma potential, the charge from the tile will be contained in the sheath region. Ions are accelerated in the sheath towards the tile while the electrons are de-accelerated. In order for the sheath to be stable, the ions must enter the sheath with sufficient velocity such that $v \geq c_s$ where c_s is the plasma sound speed. This is the well known Bohm Criterion [24]. It is possible to derive this result by considering a one dimensional, unmagnetised plasma in contact with a material surface as shown in figure 2.1. In the bulk plasma, we take the plasma potential to be zero. We assume the ions are born stationary and cold, far from the material surface, in the bulk plasma. It is assumed the electrons have a Maxwellian distribution so that their density profile can be described by the Boltzmann relation

$$n_e = n_{se} \exp\left[\frac{(\psi - \psi_{se})}{T_e}\right] \tag{2.6}$$

where n_{se} is the electron density at the sheath entrance and ψ_{se} the plasma potential at the sheath entrance. This is a valid approximation as most electrons are reflected in the sheath and so the Maxwellian distribution is maintained. There is a potential drop between the bulk plasma and the sheath entrance, in other words, ψ_{se} is negative relative to the plasma potential. This potential drop occurs in a region of plasma known as the pre-sheath. It is this drop in potential that accelerates the ions so that they satisfy the Bohm Criterion. For the ions we apply conservation of energy which leads to

$$\frac{1}{2} m_i v^2 = -e\psi \tag{2.7}$$

This equation is valid at all points in the plasma. From particle conservation, in the absence of sources and sinks, we have

$$n_i v_i = n_{se} v_{se} \rightarrow n_i = \frac{n_{se} v_{se}}{v_i} \tag{2.8}$$

From energy conservation we have

$$v_{se} = \left(-\frac{2e\psi_{se}}{m_i}\right)^{1/2} \qquad v_i = \left(-\frac{2e\psi}{m_i}\right)^{1/2} \tag{2.9}$$

Plugging this into equation 2.8 gives

$$n_i = n_{se}\left(\frac{\psi_{se}}{\psi}\right)^{1/2} \tag{2.10}$$

Substituting equations 2.10 and 2.6, for the ion density and electron density respectively, into Poissions equation, equation 2.1, we get

$$\frac{d^2\psi}{dx^2} = -\frac{e}{\epsilon_0}n_{se}\left[\left(\frac{\psi_{se}}{\psi}\right)^{1/2} - \exp\left[\frac{(\psi-\psi_{se})}{T_e}\right]\right] \tag{2.11}$$

This is valid in both the bulk plasma and the sheath. We now define a variable Δ such that

$$\Delta = \psi_{se} - \psi \tag{2.12}$$

In the sheath region $\psi < \psi_{se}$ therefore $\Delta > 0$. We can now carry out an expansion of the two terms on the right hand side of equation 2.11.

$$\left(\frac{\psi_{se}}{\psi}\right)^{1/2} = \left(\frac{\Delta}{\psi}+1\right)^{1/2} \approx 1 + \frac{\Delta}{2\psi} = 1 - \frac{\Delta}{2|\psi_{se}|} \tag{2.13}$$

Here we take a point just inside the sheath such that $\psi \approx \psi_{se}$. The second substitution and expansion gives

$$\exp\left[\frac{(\psi-\psi_{se})}{T_e}\right] = \exp\left[\frac{-\Delta}{T_e}\right] \approx 1 - \frac{\Delta}{T_e} \tag{2.14}$$

We can now substitute equations 2.12, 2.13 and 2.14 into equation 2.11.

$$\frac{d^2\Delta}{dx^2} = \frac{e}{\epsilon_0}n_{se}\left[\frac{\Delta}{T_e} - \frac{\Delta}{2|\psi_{se}|}\right] \tag{2.15}$$

This will only provide non-oscillatory solutions when

$$\frac{1}{T_e} \geq \frac{1}{2|\psi_{se}|} \tag{2.16}$$

Which, with the use of equation 2.9 can be recast as

$$v_{se} \geq \sqrt{\frac{eT_e}{m_i}} \tag{2.17}$$

which is the Bohm criterion with $c_s = \sqrt{\frac{eT_e}{m_i}}$. Ions are accelerated in the pre-sheath which penetrates deep into the plasma. The potential drop across the pre-sheath that is required for this acceleration can be estimated. From energy conservation

$$\frac{1}{2}m_i c_s^2 = e\left(\Psi - \psi_{se}\right) \tag{2.18}$$

Such that $\psi_{se} = \Psi - 0.5T_e$. This gives a pre-sheath potential drop of 0.5 T_e. In deriving

this value for c_s it was assumed that the ions are cold. By relaxing this assumption and having ions with a finite temperature, a new value for the sound speed can be obtained [25]

$$c_s = \sqrt{\frac{e(T_e + T_i)}{m_i}} \tag{2.19}$$

2.3 Ideal Probe Theory

The method for obtaining probe data is relatively simple. The probe is immersed in plasma and then biased to a potential (V_{probe}) by an external circuit. The collected current (I_p) is then recorded at different probe voltages allowing an I-V curve to be produced. The plasma parameters are then deduced from this I-V characteristic. Charged particles are drawn to the probe by the surrounding electric field which extends a few Debye lengths into the plasma, in the sheath region. The theory developed by Langmuir and Mott-Smith allows the plasma parameters to be deduced for unmagnetised plasmas with a Maxwellian distribution of ions and electrons. This theory will be discussed before moving on to fusion relevant plasma conditions.

When a probe is inserted into a plasma it is bombarded by neutral particles and the charged electrons and ions. Absent of any electric forces, the impact rate per m^2 for each species is given by their random thermal flux (Γ) which can be expressed as

$$\Gamma_s = \frac{1}{4} n_s \langle v_s \rangle \tag{2.20}$$

where n_s is the number density of that particular species and $\langle v_s \rangle$ the average speed. For a Maxwellian distribution of particles, at a temperature T_s, this can be expressed as

$$\Gamma_s = \frac{1}{4} n_s \sqrt{\frac{8eT_s}{\pi m_s}} \tag{2.21}$$

During probe operation, the probe voltage is swept from negative to positive while the current collected by the probe is recorded in order to produce the I-V curve. Data for the entire curve is typically obtained in microseconds but this can be reduced. Advanced probe techniques are capable of completing a voltage sweep in $\approx 10^{-8}$ s for an unmagnetised plasma [26]. The current collected by the probe will be composed of ions or electrons or a combination of both depending on the applied potential of the probe. For $V_{probe} = V_F$, no net current is drawn from the plasma as the electron flux reaching the probe is balanced by the ion flux. For $V_{probe} > V_F$ the electron flux exceeds the ion flux and therefore a net current will flow into the plasma while for $V_{probe} < V_F$ the ion flux exceeds the electron flux therefore a net current flows out of the plasma. For this thesis, the sign convention declares current entering the plasma as a negative current and current leaving the plasma as positive current. An ideal I-V curve is shown in figure 2.2. The curve is described as ideal because it is a theoretical prediction of an I-V curve

in an unperturbed plasma. Experimental I-V curves deviate from the ideal case, as will be discussed.

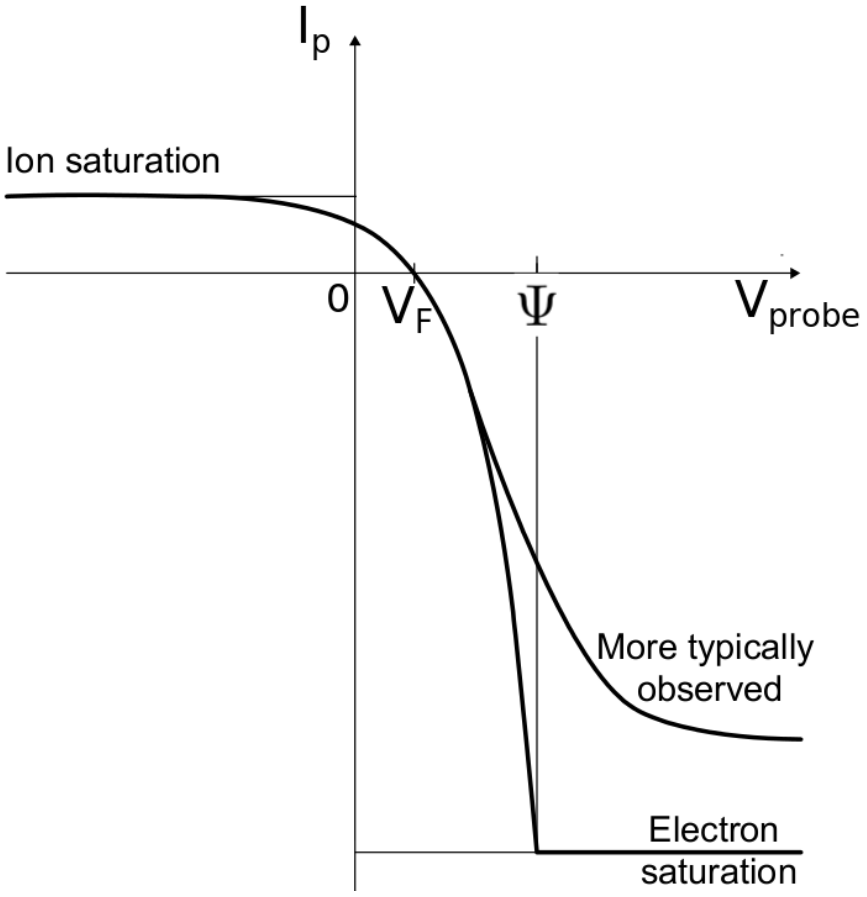

FIGURE 2.2: A schematic of the I-V curve obtained with a single Langmuir probe. Taken from [27].

If no bias voltage is applied to the probe, the probe is allowed to float and will quickly charge up negative until it reaches the floating potential (V_F). At the floating potential, the probe collects zero net current from the plasma. The floating potential is labelled on figure 2.2. It is less than the plasma potential (Ψ) as a negative bias is required to retard the flow of electrons and accelerate ions in order to balance the two fluxes. While $V_{probe} < \Psi$ the probe is biased negatively with respect to the plasma potential therefore ion collection to the probe is unhindered and so ions are collected at a saturated rate. If the probe bias is sufficiently negative all electrons are repelled and the current collected by the probe is then the ion saturation current approximated by the Bohm current

$$I_{sat}^{+} = n_{se} e c_s A \tag{2.22}$$

where n_{se} is the density at the sheath edge, e is the fundamental charge and A the area of the exposed probe tip. The ion flux is independent of the applied potential so making the probe more negative will not result in an increase in probe current.

As the bias voltage increases (becomes more positive), the sheath potential drop is reduced allowing electrons at the high energy tail of the distribution to reach the probe. This region of the curve is known as the transition region. As $V_{probe} \rightarrow \Psi$ more and more electrons are able to reach the probe as less kinetic energy is needed to overcome the potential. For a Maxwellian distribution of electrons and neglecting effects such as secondary electron emission, the electron current able to reach the probe in the transition region is given by

$$I^- = \frac{1}{4} n_{se} e A \sqrt{\frac{8eT_e}{\pi m_e}} \exp\left[\frac{(V_{probe} - \psi_{se})}{T_e}\right] \tag{2.23}$$

The term $\sqrt{\frac{8eT_e}{\pi m_e}}$ will be denoted as c_e from now on. This is just the random thermal flux of the electrons reduced by the Boltzmann factor. The total current reaching the probe in this region will be made up of ions and electrons. At $V_{probe} = V_F$ the net current to the probe is zero, $I^+ = I^-$. By equating equation 2.22 and equation 2.23 a value for the floating potential is found

$$V_F = \psi_{se} - \frac{T_e}{2} ln\left[\left(2\pi \frac{m_e}{m_i}\right)\left(1 + \frac{T_i}{T_e}\right)\right] \tag{2.24}$$

In a hydrogen plasma V_F is typically found to be $\approx -3T_e$ relative to the plasma potential. As the probe bias continues to rise it will eventually be equal to the plasma potential. At this point there is no potential difference between the probe and the plasma, therefore there are no electric fields and so the sheath disappears. The charged particles now reach the surface of the probe due to their thermal motion and so the probe collects the thermal flux of both electrons and ions. No electrons are repelled any more. Increasing the potential of the probe will act to repel the ions and a negative sheath of electrons now forms around the positive probe to shield out the positive charge. This sheath is very thin and the electric field outside of it is again zero. If the probe bias is sufficiently positive, no ions can reach the probe and the probe collects the electron saturation current. This is just the random thermal flux of electrons that enter the sheath

$$I^-_{sat} = \frac{1}{4} n_{se} e c_e A \tag{2.25}$$

For a hydrogen plasma, with no magnetic fields, the ratio of the electron saturation current to ion saturation current is given by

$$\frac{I^-_{sat}}{I^+_{sat}} \approx 40 \tag{2.26}$$

Therefore, at bias voltages where $V_{probe} > \Psi$, the ion contribution to the total current is negligible. For this reason Langmuir probe measurements cannot be used to determine the ion temperature.

Once the probe has been swept, an I-V curve can be constructed. In the transition region, the electron current contribution (I^-) can be obtained by deducting the ion

saturation current from the total current. By rearranging equation 2.23 it can be seen that

$$\ln(I^-) = \ln(I^-_{sat}) + \frac{(V_{probe} - \psi_{se})}{T_e} \tag{2.27}$$

The electron temperature can than be obtained by plotting $ln(I^-)$ against V_{probe}, the inverse of the gradient giving T_e in eV [28]. Once T_e is known, the plasma density can be extracted from the measurement of the ion saturation current, using equation 2.22. This gives the plasma density at the sheath entrance. From equation 2.6, it follows that the plasma density at the entrance to the sheath is related to the plasma density in the bulk plasma by the following equation

$$n_{se} = n_\infty \exp(-1/2) \approx 0.61 n_\infty \tag{2.28}$$

Extracting the plasma density from equation 2.22 does require a measurement of T_i , which is not possible to measure using a standard Lamguir probe. Often the assumption of $T_i = T_e$ is used, the validity of this assumption is assessed in section 2.7. As well as retarding field energy analysers discussed in section 2.7, other advanced probe techniques have been to developed to measure T_i, these are discussed in section 2.8. Floating potential measurements can be made directly by not biasing the probe or can be inferred from the I-V curve as shown in figure 2.2. In theory the plasma potential can also be read from the I-V curve, characterised by the sharp knee. However, in practise, the knee is rounded and so equation 2.24 is used to determine Ψ. The above equations have all assumed the simplest case of a collisionless sheath with no magnetic field present. All plasma-surface interactions have been neglected. I-V curves obtained in tokamak plasmas differ from figure 2.2 because these assumptions are not always valid. The magnetic field has a strong influence on the dynamics of charged particles and hence the collection of those particles by the probe. The effects of a magnetic field on probe interpretation is discussed in section 2.5.

2.4 The Pre-sheath in Magnetised Plasmas

For an unmagnetised plasma, the boundary layer between the plasma and a contacting surface consists of a quasi-neutral pre-sheath, which acts to accelerate ions up to the Bohm speed and the Debye sheath, where quasineutrality no longer holds. Often in experimental plasmas, such as tokamak experiments, a magnetic field is applied to the plasma to aid in confinement. The presence of the magnetic field affects particle dynamics and changes the constitution of the boundary layer. A numerical model was developed by Chodura [29] to study the effect of an oblique magnetic field, where the angle (θ) between the field and the tangent to the surface satisfies $\theta \neq 90°$. This angle is shown in figure 2.3. It was found that there exists three distinct regions between the bulk plasma and the material surface as shown in figure 2.3. The first region is the

familiar pre-sheath which extends far into the plasma. The second region is the Magnetic Pre-Sheath (MPS) which is also quasi-neutral. The size of the MPS scales with the ion Larmor radius and is influenced by the angle between the magnetic field and the surface normal. There is no MPS at normal incidence. The final layer is the familiar electrostatic Debye sheath where quasi-neutrality breaks down.

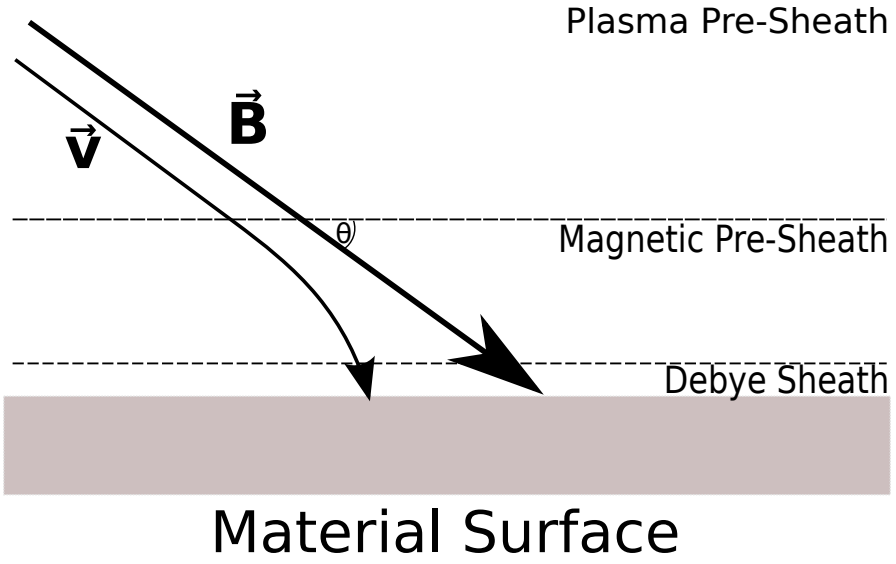

FIGURE 2.3: The structure of the sheath in front of a material surface in a magnetised plasma. Particles enter the magnetic pre-sheath with parallel velocity exceeding the Bohm velocity. In the magnetic pre-sheath the particles velocity is turned so that it is sonic perpendicular to the surface on entrance to the Debye sheath.

Chodura found that the role of the pre-sheath in a magnetised plasma is to accelerate ions such that their parallel velocity along the magnetic field lines ($v_{\parallel}$) exceeds the Bohm speed on entering the MPS. This is known as the Bohm-Chodura criterion

$$v_{\parallel} \geq c_s \tag{2.29}$$

Chodura also discovered that the ions velocity was turned from being sonic parallel to the field lines on exiting the pre-sheath to being sonic normal to the surface at the Debye sheath entrance. The role of the MPS is to turn the flow of ions so that they satisfy the Bohm criterion on entrance to the Debye sheath. The mechanism for this depends on the presence of an electric field in the MPS, the gradient of which results in a polarisation drift [30]. A potential drop (V_{MPS}) across the MPS region is responsible for the electric field. The magnitude of this potential drop depends on the angle of attack [31]

$$V_{MPS} = -T_e \ln(\sin\theta) \tag{2.30}$$

The total potential drop (V_F) between the plasma and a floating wall, however, does not depend on the presence of the magnetic field and so the floating potential of an object in a magnetised plasma is still given by equation 2.24. The total potential drop is the sum of the potential drop across the MPS and the potential drop across the Debye sheath

(V_{DS})

$$V_F = V_{MPS} + V_{DS} \tag{2.31}$$

It was realised in [31], that for increasingly lower values of θ, the potential drop across the MPS grows until a critical angle is reached (θ_c), at which point $V_{MPS} = V_F$. For a hydrogen plasma, with $T_e = T_i$, $V_F = -2.49\ T_e$. The MPS potential drop will become equal to this once $\theta \leq \theta_c = 4.75°$. The potential drop in the MPS represents the change in potential required to turn the ion flow from being sonic parallel to the field lines, to sonic normal to the surface. For small θ, there is not enough potential drop across the MPS available to turn the ions towards the surface, the ions therefore exit the MPS with a subsonic velocity normal to the surface. This regime is relevant to fusion devices, with angles of incidence as low as 1° reported in C-mod [32]. Stangeby hypothesised the disappearance of the Debye sheath for angles of incidence below the critical angle. This hypothesis was confirmed by kinetic simulations [33]. For these angles, the electron current to the wall is limited by the magnetic field, with electrons tied to the field lines, whilst the larger ion Larmor radius allows ions to reach the wall more readily. An ambipolar flow to the wall can be maintained without the need for a strong ion acceleration and so the Debye sheath is unnecessary. In extreme cases where $\theta < \left(\frac{m_e}{m_i}\right)^{0.5}$, the larger orbit of the ions means they are the more mobile species, reaching the wall faster and causing it to charge up positively. A more complex sheath arises in this case. The angle at which this would occur in a hydrogen plasma is $\approx \theta < 1°$. This regime is currently not applicable to fusion devices as it requires an extremely high degree of alignment of the divertor tiles but it may become relevant with future devices that strive to reduce θ in order to minimise heat and particle flux density to the divertor.

2.5 Probes in Magnetised Plasma

Fusion devices, such as tokamaks, use strong magnetic fields to confine the plasma long enough for fusion to occur. The presence of a magnetic field changes the dynamics of particles moving in the sheath and so has an impact on measurements made by probes. Probes are used at the edge of tokamaks, to diagnose the plasma at the plasma-surface interface. It is important that the affects of magnetic fields on probe readings are understood in order to correctly interpret probe data. The magnetic field restricts the motion of charged particles. They are free to stream along the field lines (parallel to B) but their cross-field motion is now restricted. Charged particles orbit the magnetic field lines in circular orbits with radius equivalent to the Larmor radius (ρ_L) given by

$$\rho_L = \frac{v_\perp m}{eB} \tag{2.32}$$

Where $v_\perp$ is the velocity of the charged particle perpendicular to the magnetic field, m its mass and B the strength of the magnetic field. In an unmagnetised plasma, the dynamics of charged particles are determined by the electric field of the plasma sheath

and pre-sheath but with a magnetic field particles can no longer free stream to the probe. The situation is now two dimensional as particles are restricted to following the magnetic field lines. Particle transport to the probe is now restricted by cross-field diffusion and the size of the probe starts to become important. The extent of how probe measurements are effected by the addition of a magnetic field depends on the relative size of the probe dimension d to that of the Larmor radius. Due to their lower mass, the electrons have a much smaller Larmor radius than the ions and so are effected more by the presence of a magnetic field. The probe is described to be in the weak field regime when B is low enough such that

$$\rho_{L,ion} > \rho_{L,electron} > d \tag{2.33}$$

In this regime, particles are still able to intercept the probe as they orbit the field lines and so particle collection is unaffected. The field-free results from ideal theory, as previously discussed, should still apply. As the strength of the field is increased, the Larmor radius decreases. Eventually the dimensions of the probe exceed the Larmor radius of the electrons such that

$$\rho_{L,ion} > d > \rho_{L,electron} \tag{2.34}$$

this is known as the strong field regime. The ions with their larger mass are relatively unaffected by the magnetic field in this regime, on the other hand, the collection of electrons to the probe is restricted as electrons are constrained to orbit the field lines. Electrons will only be collected by the probe if their field line ends on the probe itself, so flow to the probe is dominated by cross-field transport processes which allow charged particles to move from one field line to another. The flux of particles exiting the flux tube connected to the probe ($\Gamma_{\parallel}$) must be balanced by a flux of particles entering the flux tube via cross-field diffusion ($\Gamma_{\perp}$). It takes a long length of flux tube to balance the two fluxes because parallel transport along the field line occurs much faster than perpendicular transport. This length over which the fluxes become balanced is known as the probe collection length L_{col} and is illustrated below [34].

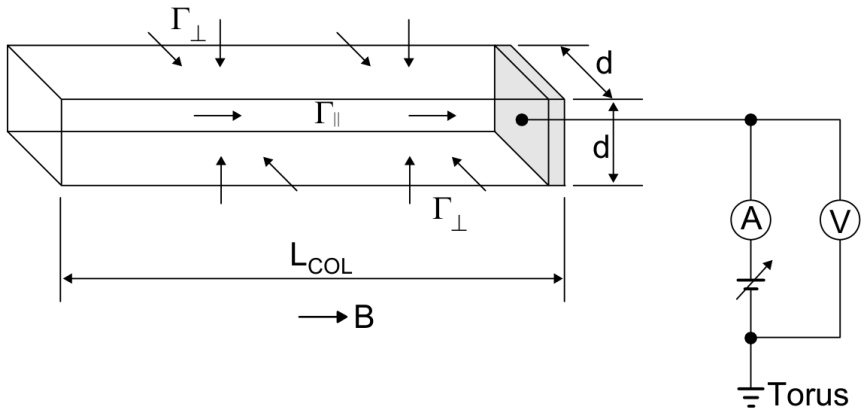

FIGURE 2.4: The probe of dimension d has a collection length associated with it (L_{col}) where $L_{col} >> d$. Taken from [34].

L_{col} is a measure of the distance in which a probe disturbs the plasma it is in. During net electron collection the current drawn by the probe is higher, therefore the collection length increases to balance the higher parallel flux. One consequence of the probe collection length is that measurements from the probe are no longer localised but are averaged over the entire collection length. Electron collection is no longer well described by the random electron flux equation 2.25 in a magnetised plasma. The most striking evidence that magnetic fields affect probe readings is from observing a dramatic reduction in the electron saturation current to ion saturation current ratio. Bohm predicted values as low as 10 [35] and this was confirmed experimentally by Sugawara [27]. Values for this ratio have been recorded in tokamaks to be even as low as unity [15]. In JET it was demonstrated that artificially high values of T_e were obtained when fitting an exponential to regions of the I-V curve where $V_{probe} > V_F$ [36]. However no significant change in T_e was observed when using regions below the floating potential. It is now standard procedure to only fit the exponential to regions below the floating potential for probes in magnetised plasma. The more points that are used in the temperature fit from bias voltages greater than V_F, the higher the measured temperature [15]. The reason for this is attributed to collisions that occur between the electrons and ions along the collection tube. Regions of increased potential (potential hills) are required, both cross-field and parallel to the field, to attract electrons to the probe. As a result, ions in the probe flux tube find themselves in a retarding field and so obey the Boltzmann relation such that $n_i \propto \exp(-V/T_i)$. Therefore a density depression exists just in front of the probe. The electron current to the probe is proportional to the plasma density in front of the probe. A reduced plasma density results in a reduced electron current as compared to the unmagnetised case. The collisions between the ions and electrons constitutes a resistance in what is known as the probe circuit shown in figure 2.5.

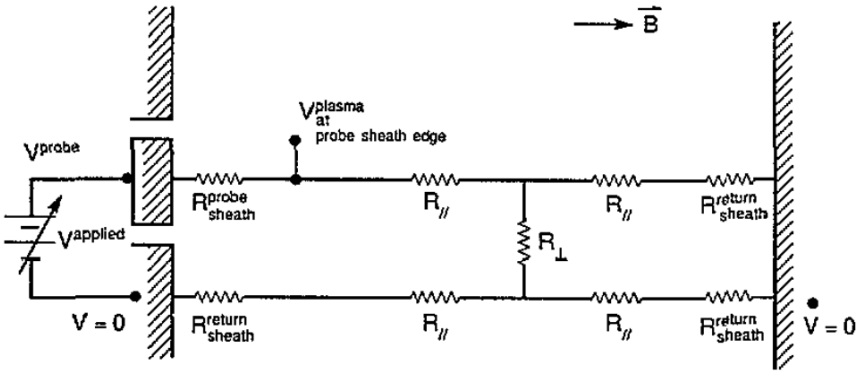

FIGURE 2.5: There are various resistances associated with the probe circuit. Taken from [37].

In an unmagnetised plasma the only source of resistance is the sheath resistance R_{sheath}^{probe} and the return sheath resistance R_{sheath}^{return}. The return sheath completes the probe circuit and is located in between the plasma and the material wall bounding the plasma. The return sheath is present in any probe circuit. Single probe theory is a good approximation in the unmagnetised case provided that the collection area of the return sheath is much greater than the collection area of the probe sheath. If this is true it can be assumed that $R_{sheath}^{return} = 0$ as resistance is inversely proportional to area. In the case when $B = 0$, the area of the return sheath is essentially the surface area of the vessel wall and so this requirement is met. No other sources of resistance are present so the probe bias only appears across the probe sheath. The I-V characteristic is defined by

$$I = I_{sat}^{+}\left[1 - \exp\left(\frac{V - V_F}{T_e}\right)\right] \tag{2.35}$$

where V is the value of the voltage drop across the sheath. $V = V_{probe} - V_s$ with V_{probe} being the applied probe voltage and V_s the plasma potential at the edge of the probe sheath. With no other sources of resistance present, the entirety of the applied voltage to the probe is contained in the sheath and so $V_s = 0$. Adding a magnetic field introduces new sources of resistance including the parallel resistance $R_{\|}$ and perpendicular resistance $R_{\perp}$. The applied voltage to the probe is now shared between the probes sheath resistance and all other sources of resistance in the circuit and because of this it is no longer valid to assume $V_s = 0$. Without knowing the value for V_s it is not possible to use 2.35 to derive T_e. In principle it could be possible to model all the other sources of resistance within the circuit in order to calculate the probe-sheath resistance which would then give V_s but cross-field transport mechanisms are not well understood.

$R_{\perp}$ is the resistance associated with cross field transport and could have different values for ions and electrons. It can not be modelled due to the lack of understanding of cross-field transport mechanisms. $R_{\|}$ is the resistance associated with parallel transport. Sources include friction caused by collisions with neutral particles and friction between the oppositely charged electrons and ions. The inability to model perpendicular resistance also prevents us from modelling the two other resistances in the circuit. R_{sheath}^{return}

depends on the area of the return sheath which in turn depends on the ratio of parallel to perpendicular transport. This ratio also determines whether or not the probe circuit extends to the other divertor target or closes back on itself. The path it takes will impact the parallel resistance. Because these resistances cannot be modelled it is not possible to calculate the value of V_s unless $R^{probe}_{sheath} >> R$ where R is all other forms of resistance in the circuit. If this is the case, single probe theory can be used to extract T_e when the plasma is magnetised.

Naturally the question arises - can Langmuir probes be used reliably in magnetised plasmas? Experiments with a pin-plate probe were conducted to test if the portion of the I-V curve below the floating potential could be used safely to derive T_e [38]. The pin-plate probe consisted of a Langmuir probe plate, with dimensions 10 mm x 5 mm and a pin probe of diameter 1 mm and a length of 5 mm, placed 2.5 mm in front of the plate. The pin was operated in floating mode for the duration of the experiment whilst the plate probe was swept as with a standard Langmuir probe. A schematic of the pin-plate probe is shown in figure 2.6. The floating potential of the pin was representative of the plasma potential outside the plate sheath, offset by a factor assumed to be constant. The experiments found that the potential on the floating pin remained almost constant for bias voltages on the plate that satisfied $V_{plate} < V_F^{plate}$. It can be concluded from this that for these bias voltages, the plate potential was entirely contained in the plate sheath and so $R^{probe}_{sheath} >> R$. As a result T_e can be extracted safely from this region. There was a slight increase of a few volts once V_{plate} was within a few T_e of floating i.e. $V_F - 3T_e \leq V_B \leq V_F$. This was attributed to either an extraneous effect or some of the probe bias appearing elsewhere in the probe circuit. If the later were true, the paper expects between a 15% $\rightarrow$ 20% error in the T_e measurement when using this region. For bias voltages such that $V_{plate} > V_F^{plate}$ it was found that the pin floating potential increased monotonically with the bias voltage applied to the plate. This is due to the formation of a potential hill which is established to drive the electron current to the probe against the friction of the ions in the probe collection tube. This potential hill results in a reduced plasma density in front of the probe which leads to a reduced electron current. The electron current in this region no longer behaves as a simple exponential. Including points from this region in the exponential fit will result in a spuriously high measurement of the electron temperature. In later work, Stangeby concluded that it is a reasonable assumption to use the region of the I-V curve below floating potential to yield a reliable value of T_e [37].

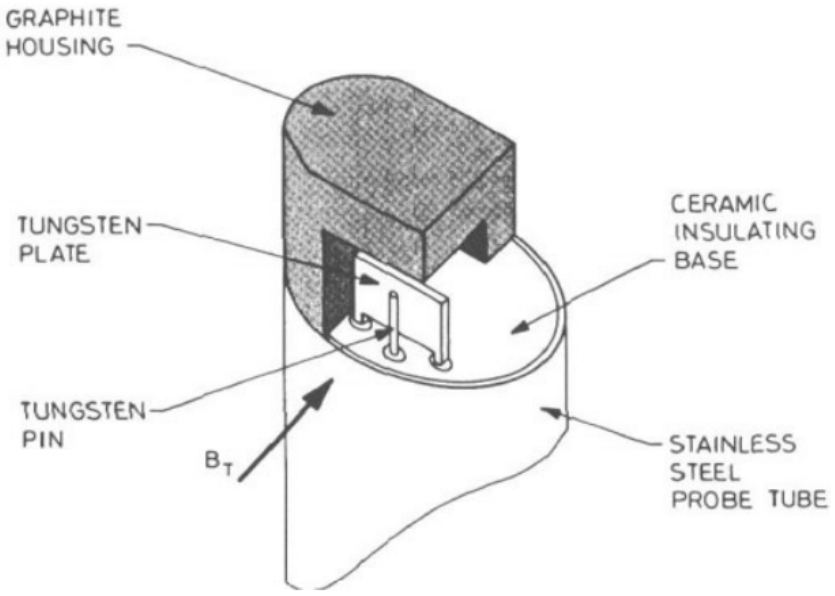

FIGURE 2.6: The pin-plate probe consisting of a tungsten pin located in front of a tungsten plate. Taken from [37].

Once a probe is operating in the strong field regime, the effects of the magnetic field must be taken into account in order to reliably measure the electron temperature. Increasing the field further leads to the 'very strong field' regime. This is defined at the point where

$$d > \rho_{L,ion} > \rho_{L,electron} \tag{2.36}$$

The motion of both electrons and ions is now strongly affected by the field. It is simple to see whether or not this regime is relevant to fusion. As a typical example, the magnetic field strength in the divertor region of JET is ≈ 3 T and the electrons and ions have a temperature of around 10 eV. This gives the ions a Larmor radius of ≈ 0.1 mm while probes are typically 2 mm long. The high temperatures in this region place a constraint on the size of the probes as they need to be large enough to dissipate the heat and avoid being melted, so making the probes smaller in order to simplify probe interpretation is not a viable option. In this regime, particles are only able to reach the probe from the direction parallel to the field so it appears to them that the probe has a plane geometry regardless of its actual geometry. This means the effective collection area of the probe (A_{eff}) is now reduced from its actual surface area ($A_{surface}$) to the projection of the surface (A_{proj}) in the direction of the field

$$A_{eff} = A_{proj} = A_{surface} sin(\theta) \tag{2.37}$$

where θ is the angle between the field and probe as shown in figure 2.7. The shape of the probe in this regime is not very important only its cross sectional area perpendicular to $\vec{B}$. As demonstrated by equation 2.22, the effective collection area of the probe must be known in order to determine the plasma density from measurements of the ion saturation

current. Experiments were carried out by Brown in a linear plasma device that contained two sets of diagnostics capable of measuring the electron density, Langmuir probes and a microwave interferometer [39]. The probe was able to give highly localised measurements of the plasma conditions. Both diagnostics were used simultaneously whilst the magnetic field strength was increased. As the field became stronger, the electron density derived from probe readings deviated from those obtained by the interferometry. The probes gave a lower value of n_e than measured by the interferometry. This can be explained by a reduction in the collection area of the probe due to the increased field which then results in a lower value for I_{sat}^{+}. If the effects of the magnetic field are not taken into account the plasma density will be underestimated and the electron temperature overestimated.

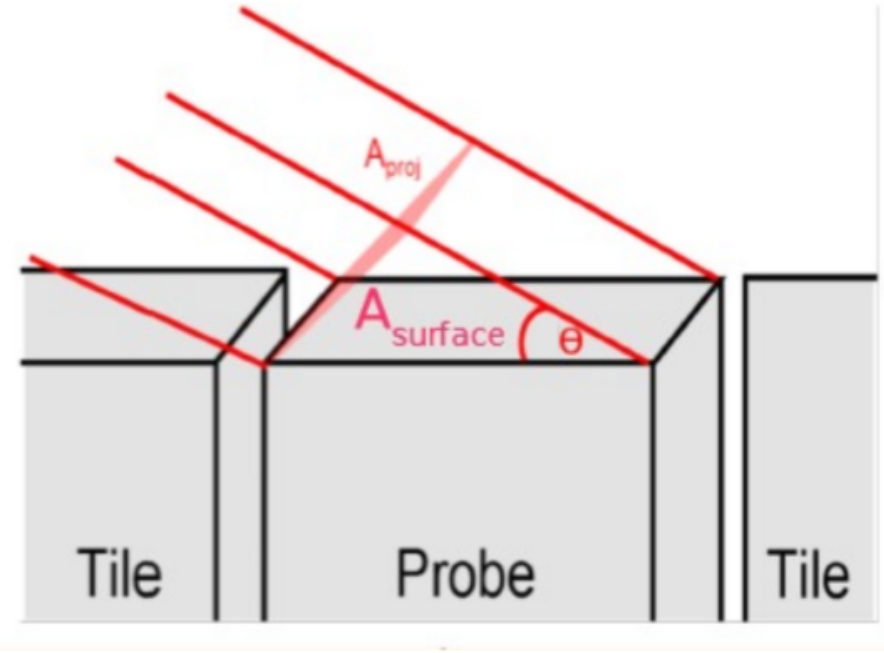

FIGURE 2.7: In a strongly magnetised plasma the effective collection area of the probe is reduced from its surface area ($A_{surface}$) to the projection of that surface perpendicular to the magnetic field (A_{proj}).

2.6 Langmuir Probes in Tokamaks

A tokamak plasma, with high temperature and density, is a hostile environment for a material surface. Any material placed into the plasma, such as a probe, will suffer damage from the high heat and particle flux impinging on it. This is also true of probes placed in the relatively cooler and less dense SOL region. Steps have to be taken to ensure the probes survive the plasma conditions so that useful measurements can be taken. It is also important that the probe does not contaminate the plasma, particularly with high Z impurities, which reduce the temperature of the plasma by radiative cooling. Various techniques have been developed to enhance the lifetime of tokamak probes. One technique is to place the probes in a reciprocating probe head. This head can be submersed into the SOL via a drive mechanism which is connected to

a support structure. The drive mechanism plunges the head into a region of the SOL, the probe then takes its measurements before being retracted back into the vacuum region away from the plasma. An additional benefit of the reciprocating system is that it allows the probe to diagnose the plasma at different depths in the SOL, allowing SOL profiles to be constructed. The probe head may be exposed to plasma for $\approx$ 100 ms during a typical plunge. It is advantageous for the probe head to be as light as possible so that it can be quickly accelerated into and out of the plasma. It must also be able to survive heat fluxes on the order of 10 MW/m^2 [16]. Graphite is the material of choice in many tokamaks as it is a low Z material capable of withstanding the hostile conditions presented by the plasma. Low Z impurities result in less cooling to the core due to radiative cooling. However, over time, damage to the probe is inevitable. Modular designs are often employed on modern tokamaks to aid in the task of probe replacement. Another technique is to use heat sink probes that are in good thermal contact with a large heat sink.

An alternative probe design is to align the probe so that its surface is flush with the surrounding divertor tiles. These Flush Mounted Probes (FMP) are one of the most robust probe designs and they are almost as resilient as the divertor tiles, sharing the same geometry relative to the magnetic field [40]. The grazing angle between the field and the FMP in the divertor region means the intense heat flux is spread out over a larger area thus reducing the damage to the probe. This grazing field line can lead to complications in interpreting the data obtained from FMPs as the projected area of the probe can become comparable to the sheath area for such small field line angles. This will be discussed further in Chapter 4.

2.7 Underlying Assumptions of Probe Theory

In deriving the equations of section 2.3 it was assumed the particles had a Maxwellian velocity distribution. A reciprocating probe was used on COMPASS to evaluate the velocity distribution of electrons within the last closed flux surface (LCFS) and the SOL. Evidence for a bi-Maxwellian distribution of electrons was found, corresponding to two Maxwellian distributions of electrons at different temperatures [41]. This has also been reported on CASTOR [42] and NSTX [43]. This can lead to errors in the electron temperature measurement, especially if the I-V curve is only swept up to the floating potential, in which case only the high energy tail of the electron distribution is sampled. In the far SOL, close to the walls, it was found that the electrons adopted a single Maxwellian distribution and so the assumption was valid in this region of the tokamak.

A value for T_i is required to obtain the plasma density from the ion saturation current. Due to difficulties in obtaining a measurement for this value it is often assumed to be the same as the measured T_e value. Retarding Field Energy Analysers (RFEA) can be used to obtain measurements of T_i, by using a series of charged plates and grids

to repel electrons and only collect the ions. The exponential drop off of the ion current, as the bias voltage is swept, can then be used to extract T_i. Two RFEAs were placed on MAST to measure the ion temperature [44]. A schematic of the RFEA is shown in figure 2.8. It was found that for low power L-mode plasma discharges, $T_I = T_e$ was a good assumption at the target and in the SOL. However, for higher power discharges and in H-mode, ratios of $T_i/T_e = 1 \rightarrow 3$ were observed so this assumption may not always hold.

2.8 Advanced Probe Designs

A whole range of advanced probe techniques have been developed in order to measure quantities such as the plasma potential, electron temperature, electron density and ion temperature without the limitations of standard Langmuir probes discussed above. Ball-pen probes and emissive probes, both shown in figure 2.8, aim to measure the plasma potential directly by reducing the ratio of the saturation currents to one such that the probe floats at the plasma potential [45]. These probes will be discussed in Chapters 5 and 6 respectively. BPPs and LPs can be used simultaneously to provide fast measurements of T_e, this will also be discussed in Chapter 5. A segmented tunnel probe has been developed that is capable of measuring the electron temperature without actually collecting any electrons [46]. The probe is U-shaped, consisting of a conducting tunnel and a conducting backplate. A schematic of the probe is shown in figure 2.8. Both conductors are biased sufficiently negatively to repel all electrons. The ion current collected by each conductor is measured. The ratio of the currents to each collector depends on the thickness of the sheath at the entrance to the tunnel which in turn depends on T_e. This relationship is derived from Particle-In-Cell modelling of the probe. By adding a conducting diaphragm around the entrance to the tunnel it is possible to prevent electrons from reaching one of the tunnel segments [47]. By sweeping the bias voltage across this segment, an exponential fall off in the ion current is observed. This data is hidden by the electron current for a standard probe. The rate at which the ion current decreases allows T_i measurements to be made. The segmented tunnel probe is one example of a family of probes that aim to shield the electrons from a collector so that the ion current can be analysed. These Ion Sensitive Probes (ISP) often exploit the difference in Larmor radii of the electrons and ions to inhibit electrons from reaching a part of the probe [48].

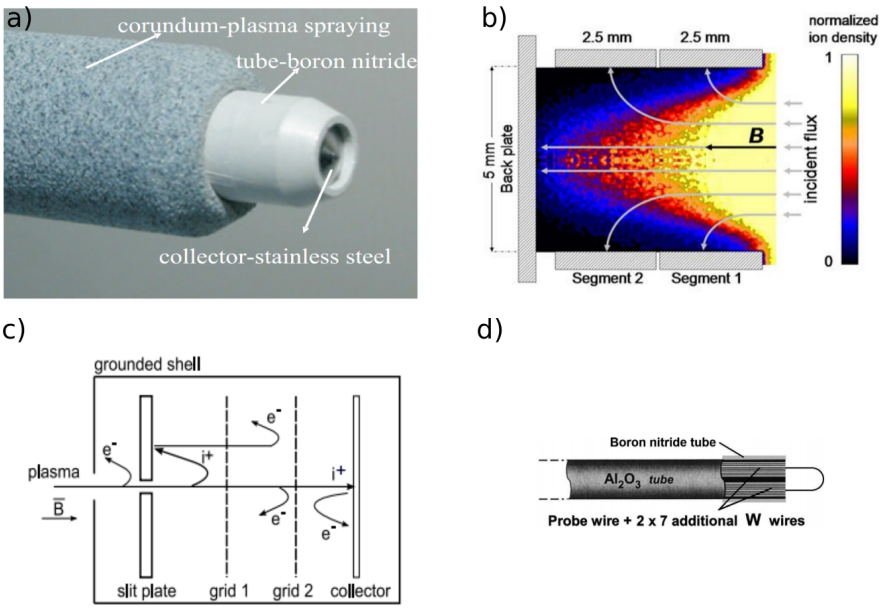

FIGURE 2.8: Various advanced probe designs include: a) The ball-pen probe, taken from [49]; b) The segmented tunnel probe, taken from [47]; c) The retarding field energy analyser, taken from [44] and d) The emmisive probe taken from [114].

2.9 Summary

Sheath theory has been introduced as this underpins measurements made by electric probes in plasmas. Standard Langmuir probe theory has been introduced and complications in probe interpretation arising from the presence of magnetic fields have been discussed, this will be explored further in Chapter 4. Various advanced probe techniques have been summarised, of these the BPP and emissive probe will be studied in Chapters 5 and 6 respectively.

Chapter 3

Particle In Cell Model

3.1 Introduction

Computer simulations are the third tool, alongside theory and experiment, that scientists can use to understand natural phenomena. For systems with many degrees of freedom such as a laboratory plasma with more than 10^{21} particles, simulations provide a means in which to model the system and develop an understanding of the physics. In the limit of numerical noise, simulations provide the user with perfect diagnostics, the ability to make measurements of desired quantities without disturbing the system. This is an invaluable asset for testing theoretical predictions. Simulations are therefore a powerful utensil that compliment experiments and theory. Deep insight into the physics of plasmas has been gained by the use of computer simulations. In 1964 Landau damping of electrostatic waves was observed in a computational plasma experiment by Dawson [50]. This phenomena had been predicted by theory but had no empirical observations to support it at the time. There have been huge increases in computational power since then and as that power has increased so has the capability of computer simulations to explore the natural world. Today a whole host of plasma simulation codes are used to study tokamak plasmas. The application of these codes range from simulating large volumes of a tokamak, providing macroscopic quantities such as plasma density and temperature to tracking individual particles in a small sample of the divertor region to determine their behaviour as they approach the plasma-surface boundary. Simulations can enhance theoretical understanding and provide measurements that would be impossible to make in a physical experiment.

In the ideal case of unlimited computing power and memory, simulation codes would model plasmas by following the trajectories of every particle in the plasma as they move due to self-consistent electric and magnetic fields. Each particle in the system would interact with every other particle via the electric field. The simulations would be advanced in infinitesimally small time steps. At each time step the force acting on each particle due to every other particle would be calculated, this force would then go into Newton's equations of motion to supply each particle with a new velocity and position. Interaction forces would then need to be re-calculated and the cycle repeated until the

simulation had run for the desired time. Even with the power of modern computers it is not possible to do this. A complete simulation of a tokamak plasma would be required to follow $\approx 10^{21}$ particles for millions of time steps, calculating the force at each time step. The amount of operations required to calculate these particle-particle interactions for n particles in the system scales on the order n^2. No computer is capable of handling this many particles. However it is still possible to capture all of the relevant physics without such stringent computing demands.

Various computational techniques have been developed to simulate plasmas: Particle-In-Cell (PIC) codes which follow the trajectories of individual particles in the plasma; Fluid models that treat the electrons and ions as separate fluids; Hybrid models that use a combination of fluid and PIC techniques to model the plasma; gyrokinetic models that average over the gyromotion of the charged particles and tree codes that are able to simulate weakly coupled plasmas without the use of a spatial grid [51]. Each method has certain advantages and disadvantages that determine where its use is applicable. These will be discussed below.

Out of the three categories PIC codes are considered to be the most fundamental way to model a plasma. Individual particles are tracked as they move across a spatial domain, responding to self consistent electric and magnetic fields, generated by the electric charge of the particles. The individual particles are in fact superparticles that represent many real particles. Rather than particle-particle interactions between every pair of particles in the simulation, superparticles deposit charge at discrete grid points along the domain. Other field quantities such as the electrostatic potential and electric field are then calculated from this charge density. The field is then interpolated back to the particles from the grid points in order to generate a new velocity and position. The discretisation of the field values as well as the use of superparticles allows modelling of the plasma from first principles. The essential physics of a real plasma can be captured with far fewer particles than are present in a real experiment. However, in order to reduce statistical noise in the simulations, large numbers of superparticles must be followed and there are certain stability criteria that must be met. As a result, PIC simulations are compute-intensive, the simulations take a long time to run and this restricts PIC simulations to studying small regions of plasma.

Fluid codes ease the computational burden by treating the ions and electrons as separate fluids rather than individual particles. The plasma is described by the density, mean velocity and mean energy of the electrons and ions. Fluid codes solve the fluid equations which arise by taking the moments of the governing kinetic equations. The fluid equations require closure conditions that must be approximated [52]. This method is applicable when the plasma is in thermal equilibrium [53]. As fluid codes are less demanding on computer resources they can be used to study the evolution of large-scale instabilities in tokamak plasmas.

Hybrid models exist that combine aspects of fluid and PIC codes. A common implementation of this technique is to treat the electrons as a fluid while modelling the ions

kinetically. In this case the electrons are a neutralising background with a Boltzmann distribution. This technique increases the size of the required time step, by orders of magnitude, as only the motion of the ions has to be tracked rather than the faster motion of the electrons. This also reduces the number of particles that have to be followed. As a result, these models can be run in less time but are useful if the user is only interested in the ion dynamics.

It is not possible to simulate a Langmuir probe without capturing the physics of the sheath [54]. The plasma sheath cannot be correctly modelled by fluid codes as the particle distributions inside the sheath are far from being in equilibrium [55]. The exact position of the sheath boundary is not well defined either as there is a smooth transition from the pre-sheath to the sheath near surfaces. PIC codes, on the other hand, make no assumptions about the distribution of the particles, they allow for any distribution function in phase space. By applying the fundamental equations, the PIC method is able to preserve most of the physics. An alternative method to PIC is to directly integrate the Vlasov equation, which in one dimension (1D) is given by

$$\frac{\partial f_s}{\partial t} + v\frac{\partial f_s}{\partial x} + \frac{q_s E}{m_s}\frac{\partial f_s}{\partial v} = 0 \tag{3.1}$$

where f_s is the phase space distribution function for a given species s. Direct Vlasov codes numerically solve the Vlasov equation on a phase space grid without the use of particles. The codes can be used for the same spatial regions and time scales as PIC codes but the algorithms are computationally expensive and suffer from numerical instability [56]. The benefits are that they do not suffer from numerical noise which effects PIC simulations due to the finite number of superparticles used [57]. Complex probe designs such as the Ball-pen probe, which will be discussed in Chapters 5 and 6, require the tracking of individual particles in order to interpret experimental data obtained by the probes. Therefore completely kinetic PIC simulations must be carried out. The rest of this chapter will proceed to describe the general PIC method before moving on to describe each step of the algorithm in more detail.

3.2 General Method

It is not possible, with modern day computers, to simulate a plasma by tracking all 10^{21} particles and calculating all the particle-particle interactions for each pair of particles in the system. The PIC scheme overcomes this problem by using single particles, called superparticles, to represent a given number of physical particles and by introducing a spatial grid as shown in figure 3.1. The superparticles have the same charge to mass ratio as their real particle equivalents and so follow the same trajectories as that of a real particle. For the remainder of this chapter the word particle is synonymous with superparticle. The spatial domain of the simulation is discretised into grid cells. For simplicity, equal length grid cells will be assumed but this is not a necessity for the PIC scheme. Non-uniform grid spacing is a technique that can be employed for

computational efficiency, in order to resolve regions where steep gradients in plasma parameters are expected to exist and not over-resolve other regions. At the boundaries of the cells, field values, namely the charge density, electrostatic potential and electric field are calculated. However, the particles see a continuous domain and are free to take any position within the simulation. The charge density at each grid point is determined by the locations of the particles. The other field values are calculated from this charge density. The mechanism in which particle positions across a continuous domain are converted to charge densities on a spatial grid and correspondingly the mechanism which translates field values from grid locations back to the individual particles is known as weighting and will be discussed in section 3.2.1. At the beginning of an electrostatic PIC simulation the grid is loaded with a particular distribution of particles depending on the plasma parameters to be modelled. It then follows an algorithm as depicted in figure 3.2. Each particle deposits charge to neighbouring grid points, Poisson's equation is solved to obtain a potential, the derivative of this is used to calculate the electric field and the field is mapped back to the particles which are then accelerated and moved. Once the particles have been moved, the PIC algorithm is complete, time is advanced by one time step and the whole cycle restarts by calculation of a new charge density based on the updated particle positions. This cycle will carry on until a certain time has been reached or steady-state has been obtained. The aforementioned steps are essential to any application of the PIC method to plasma simulations. Additional steps can also be added to the cycle based on the requirements of the user. These steps can include Monte Carlo collisions between the particles, absorption and injection of particles and other boundary effects such as sputtering, secondary electron emission and specular reflection. These steps are often added to the end of the PIC cycle once all the original particles in the system have been moved.

The introduction of the grid means particles interact with each other via a charge density rather than pair to pair interactions. For a simulation with n particles the introduction of the grid reduces the amount of calculations required per time step to the order of n rather than n^2 as in the particle-particle scheme. Splitting a physical, continuous domain up into grid cells does have implications which need to be considered in order to ensure the simulation can still produce physically accurate results. The consequences of introducing a grid on to the domain and how this can still accurately represent a plasma are discussed in section 3.3. The grid allows the equations that determine field values and particle motion to be solved using finite differencing, a scheme that takes continuous differential equations and converts them so that they can be solved on discrete grids in space and time. The first step of finite differencing is to carry out a Taylor expansion. For a function $f(x)$, a discretised form of the first differential of the equation can be obtained as follows. First carry out a Taylor expansion in the forward direction

$$f(x+\Delta x) = f(x) + \Delta x \frac{\partial f(x)}{\partial x} + \frac{\Delta x^2}{2!}\frac{\partial^2 f(x)}{\partial x^2} + \frac{\Delta x^3}{3!}\frac{\partial^3 f(x)}{\partial x^3} \tag{3.2}$$

Repeating the procedure in the backwards direction

$$f(x-\Delta x) = f(x) - \Delta x\frac{\partial f(x)}{\partial x} + \frac{\Delta x^2}{2!}\frac{\partial^2 f(x)}{\partial x^2} - \frac{\Delta x^3}{3!}\frac{\partial^3 f(x)}{\partial x^3} \tag{3.3}$$

The two equations can be combined giving

$$\frac{\partial f(x)}{\partial x} = \frac{f(x+\Delta x) - f(x-\Delta x)}{2\Delta x} + \frac{\Delta x^3}{3!}\frac{\partial^3 f(x)}{\partial x^3} \tag{3.4}$$

Combining the two equations in this way is known as central differencing. The term proportional to Δx^3 is dropped so this method is second order accurate.

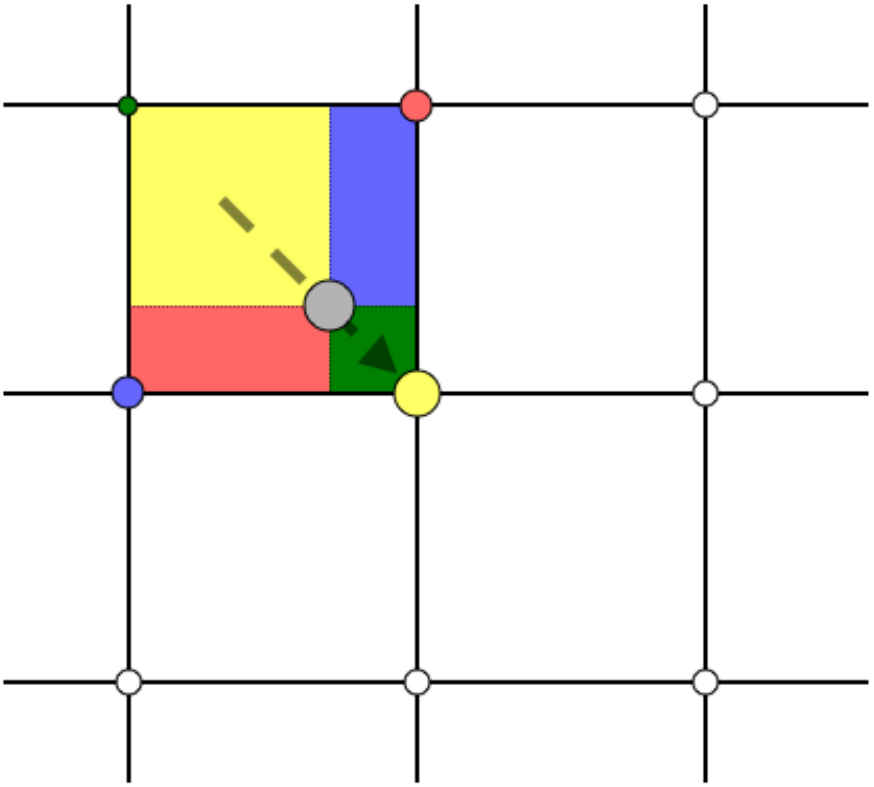

FIGURE 3.1: A representation of a two dimensional grid. The particle (grey circle) moves through the domain and deposits charge on the grid points. The area of the rectangle is proportional to the amount of charge deposited at each grid point.

Each step of the PIC cycle will now be detailed with VSim specific algorithms detailed where appropriate. VSim is a three dimensional, commercial PIC code used for the simulations detailed in this thesis.

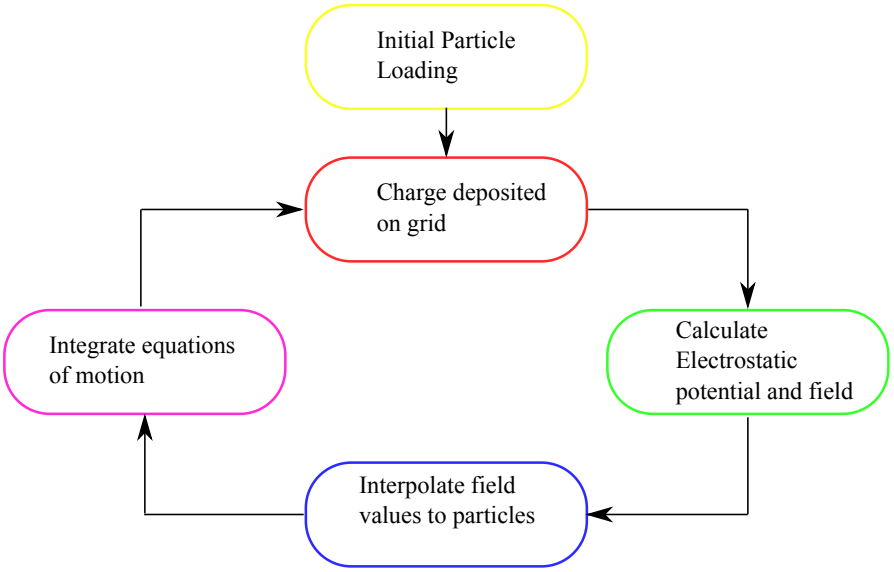

FIGURE 3.2: A flow chart of the essential steps of the PIC algorithm

3.2.1 Calculating the Charge Density

During this stage of the cycle, the charge density at each grid point is calculated from the individual particle locations. Weighting is the name given to the calculations which interpolate charge densities to the grid points from the continuous particle positions. Various weighting algorithms exist. The simplest weighting algorithm is to simply deposit all of a particles charge to its nearest grid point. This is the Nearest Grid Point (NGP) scheme. This is a zero order weighting method. Any particles within half a cell of a grid point are assigned to that grid point. Let Δx be the cell width, x the distance between the particle and grid point X and $W(X)$ denote the weighting at grid point X. In the NGP scheme

$$W(X) = \begin{cases} 1, & \text{if } |x| \leq \frac{\Delta x}{2} \\ 0, & \text{otherwise} \end{cases} \tag{3.5}$$

This is a computationally fast weighting method as it only requires one grid point lookup per particle but this comes at the expense of adding noise to the simulation. As a particle moves away from its original grid point and into the region of a new grid point, the charge density at the new grid point suddenly jumps up to have a value of one and the density at the grid point it just left falls down to zero. This weighting scheme is not commonly deployed due to the noisy transition as particles move between cells. It is possible to reduce this noise by spreading the charge of the particle over more grid points at the expense of increased computation time. First-order weighting, also known as area weighting, smooths the density and field fluctuations compared to NGP but is more computationally expensive as it requires two grid point lookups for each particle. In this method, for a 1D simulation, each particle contributes charge to its nearest two grid points. The first step calculates the offset (δ) of the particle from the closest grid

point to its left.

$$\delta = x_i - X_j \tag{3.6}$$

where x_i is the particles position and X_j the x-coordinate of the grid point. As this is for the grid point to the particles left, $x_i > X_j$. The charge assigned to the j^{th} grid point is then

$$W(j) = 1 - \delta \tag{3.7}$$

The charge assigned to the j+1 cell is

$$W(j+1) = \delta \tag{3.8}$$

Such that the total charge deposited to the grid equals the charge of the particle. This results in a much smoother contribution to the charge density as the particle propagates through the grid. This is the most commonly employed weighting scheme and is the default for VSim. Higher order weighting methods do exist such as quadratic and cubic splines, that are second order and third order accurate respectively. These schemes further smooth the non-physical noise at the expense of more computation time by increasing the number of grid points that a particle contributes its charge to. This does lead to complications at the edge of the simulation boundary where there are insufficient neighbouring grid points.

3.2.2 Calculating the Potential

Now the charge density is known at each grid point, Poisson's equation for electrostatics can be solved to obtain the electrostatic potential.

$$\nabla^2\psi = -\frac{\rho}{\epsilon_0} \tag{3.9}$$

This can be solved numerically on a discretised grid using finite differencing. For a 1D simulation Poisson's equation can be expressed in finite difference form

$$\frac{\partial^2\psi}{\partial x^2} = \frac{\psi(x+\Delta x) - 2\psi(x) + \psi(x-\Delta x)}{(\Delta x)^2} = -\frac{\rho_x}{\epsilon_0} \tag{3.10}$$

For clarity we rewrite (3.10) with labels based on the grid number j.

$$\frac{\partial^2\psi}{\partial x^2} = \frac{\psi_{j+1} - 2\psi_j + \psi_{j-1}}{(\Delta x)^2} = -\frac{\rho_j}{\epsilon_0} \tag{3.11}$$

The value of ψ at grid point j, (ψ_j), depends on the value of ψ at the two grid points either side of it (ψ_{j-1} and ψ_{j+1}), so the grid points are coupled together. In order to find the value of ψ_j at N different grid points requires the solution of N coupled linear

equations. These coupled equations can be expressed in matrix form.

$$\begin{pmatrix} B_1 & C_1 & & & \\ A_2 & B_2 & C_2 & & \\ & A_3 & B_3 & C_3 & \\ & & \ddots & \ddots & \ddots \\ & & & A_N & B_N \end{pmatrix} \begin{pmatrix} \psi_1 \\ \psi_2 \\ \psi_3 \\ \vdots \\ \psi_N \end{pmatrix} = \begin{pmatrix} \rho_1 \\ \rho_2 \\ \rho_3 \\ \vdots \\ \rho_N \end{pmatrix} \tag{3.12}$$

Where $A = 1, B = -2$ and $C = 1$. A matrix like this, with non-zero elements only on the diagonal and one place either side of it, is known as a tri-diagonal matrix. The value of the charge density (ρ_i) at each grid point is known as it was calculated in the previous step of the PIC algorithm. This matrix equation must now be solved in order to obtain the potential at each grid point. There are various numerical methods to find the solution and they can be divided into two categories: iterative methods and direct methods. VSim supports both type of solvers. For parallel simulations running on multiple cores, the iterative solver is employed. Before a solution can be found, the boundary conditions must be supplied as the grid points at the edge of the domain only have one neighbouring grid point. Two common choices for boundary conditions exist, Dirichlet boundary conditions where ψ_1 and ψ_N are set to a fixed value or Neumann boundary conditions where the gradient of the potential is fixed at the boundary. The implementation of Dirichlet boundary conditions is simple, B_1 and B_N are set equal to one, $C_1 = 0$ and $A_N = 0$. ψ_1 and ψ_N are then given the desired potential boundary values α and β respectively. The first and last matrix equations then read

$$1.\psi_1 + 0.\psi_2 = \alpha \tag{3.13}$$

$$0.\psi_{N-1} + 1.\psi_N = \beta \tag{3.14}$$

Neumann boundary conditions involve fixing the gradient of the potential (i.e. the electric field) at the edge of the domain. This could be implemented by setting $B_1 = -\frac{1}{\Delta x}$, $C_1 = \frac{1}{\Delta x}$ and $\rho_1 = \alpha$. Thus giving the first line in the matrix equation as

$$\frac{\psi_2 - \psi_1}{\Delta x} = \alpha \tag{3.15}$$

Once the boundary conditions have been supplied the tri-diagonal matrix equation can be solved.

3.2.3 Calculating the Electric Field

Once the potential is known at each grid point the electric field is easily found by calculating the gradient of the potential.

$$E = -\nabla\psi \tag{3.16}$$

which in one dimension becomes

$$E = -\frac{\partial \psi}{\partial x} \tag{3.17}$$

This can be discretised as before using finite differencing.

$$E_j = -\frac{\psi_{j+1} - \psi_j}{\Delta x} \tag{3.18}$$

3.2.4 The Particle Mover

The final step in the PIC cycle is to calculate a new position and velocity for each particle in the simulation based on the forces acting on them. In order to do this the following equations of motion must be solved

$$\vec{F} = m\frac{d\vec{v}}{dt} = q(\vec{E} + \vec{v} \times \vec{B}) \tag{3.19}$$

$$\vec{v} = \frac{d\vec{x}}{dt} \tag{3.20}$$

The particles positions and velocities can be found by integrating the differential equations (3.19) and (3.20) again using finite difference methods. VSim uses a leap-frog scheme with a Boris advance [58] to push the particles. The leap-frog method involves offsetting the velocity by half a time step from the position. So the velocity of the particles is only known at half integer time steps while the positions are known at integer time steps. This requires the initial velocities of the particles to be moved back half a time step at the beginning of the simulation, a "de-acceleration", in order to have time centred velocities. This just requires calculating the fields as before. This method is known as Leap-frog because in order to calculate new positions requires a leap over the known velocity. The algorithm is demonstrated in figure 3.3.

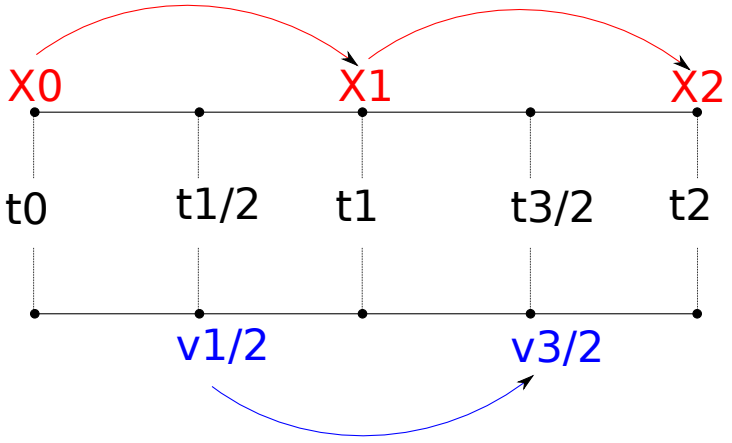

FIGURE 3.3: A graphical representation of the Leap-Frog scheme. Particle positions are known at integer time steps while velocities are known at half-integer time steps.

In discretised form the equations of motion become

$$\frac{x_{t+1} - x_t}{\Delta_t} = v_{t+1/2} \tag{3.21}$$

$$\frac{v_{t+1/2} - v_{t-1/2}}{\Delta t} = \frac{q}{m}\left[\vec{E_t} + \frac{(v_{t+1/2} + v_{t-1/2})}{2} \times B_t\right] \tag{3.22}$$

First, equation 3.22 must be solved to get the new velocity of the particle ($v_{t+1/2}$), this is then inserted into equation 3.21 to obtain a new position for the particle (x_{t+1}). This is carried out for every particle in the system.

The most common implementation of the Boris scheme separates the effects of the electric and magnetic fields. Firstly half of the impulse due to the electric field is added to the particle's velocity creating an intermediate variable v^-

$$v^- = v_{t-1/2} + \frac{q}{m} E_t \frac{\Delta t}{2} \tag{3.23}$$

The magnetic field then acts on v^- to create a second intermediate variable v^+. The magnetic field only effects the rotation of the velocity vector not the magnitude.

$$\frac{v^+ - v^-}{\Delta t} = \frac{q}{2m}(v^+ + v^-) x B_t \tag{3.24}$$

Finally the second half of the electric impulse is added to v^+ to obtain the new velocity for the particle.

$$v_{t+1/2} = v^+ + \frac{q}{m} E_t \frac{\Delta t}{2} \tag{3.25}$$

The Boris scheme can be used to advance particles for an arbitrarily large number of time steps whilst remaining accurate and is therefore the de facto standard for particle movers [59]. The value for equation 3.25 is then substituted into equation 3.21 to obtain a new position for each particle.

3.3 Consquences of the Computational Grid

3.3.1 Stability Conditions

PIC simulations utilise finite difference equations to find solutions to continuous differential equations on a discretised grid. The use of finite difference equations can provide accurate physical results provided certain stability conditions are met. To ensure the stability of the leap-frog particle advancing algorithm, the time step (Δt) must be sufficiently small such that

$$\omega_p \Delta t < 2. \tag{3.26}$$

where ω_p is the plasma frequency

$$\omega_p = \sqrt{\frac{e^2 n_e}{\epsilon_0 m_e}} \tag{3.27}$$

A time step of this size ensures stability of the algorithm but a further restraint must be placed upon the time step for it to provide accurate results [60].

$$\omega_p \Delta t < 0.2. \tag{3.28}$$

The second constraint determines the minimum grid spacing (Δx) that can be used.

$$\Delta x \leq \lambda_D \tag{3.29}$$

where λ_D is the Debye length. PIC codes can only resolve phenomena that are larger than Δx, anything smaller than this is smoothed over. PIC codes must resolve the Debye length in order to accurately capture the shielding effects. If this criteria is not met, non-physical numerical heating of the electrons will occur. The temperature of the electrons will increase until the Debye length is such that the stability criteria is met. The time step is further constrained by the criteria that no particle should be able to travel more than one grid cell in a given time step known as the Courant-Friedrich-Lewy condition [61].

$$\Delta t < \frac{\Delta x}{v_{max}} \tag{3.30}$$

where v_{max} is the speed of the fastest moving particle in the system. For high density, low temperature plasmas $\lambda_D \approx 10^{-6}$ m while electron velocities can exceed 10^6 ms^{-1}. This means thousands of grid cells may be necessary to simulate the 10 mm^2 tip of a Langmuir probe with time steps as small as 10^{-12} s. Simulations with these demands can only be carried out on supercomputers.

3.3.2 Finite Sized Particles

Rather than the point sized particles of a physical plasma, particles in a PIC simulation are finite sized clouds of uniform charge. Finite sized particles are a direct result of weighting particles on to the grid. The weighting method determines the effective size and shape of the particle as viewed by grid. For the first order weighting scheme described above, a fraction of the clouds charge which is in the J^{th} cell is weighted to the X_J grid point and the rest of it goes to the X_{J+1} grid point. This gives the particle a triangular shape, so the particle is effectively a triangular cloud of uniform charge centred at x_i with a width of $2\Delta x$ as it is able to influence grid points either side of it.

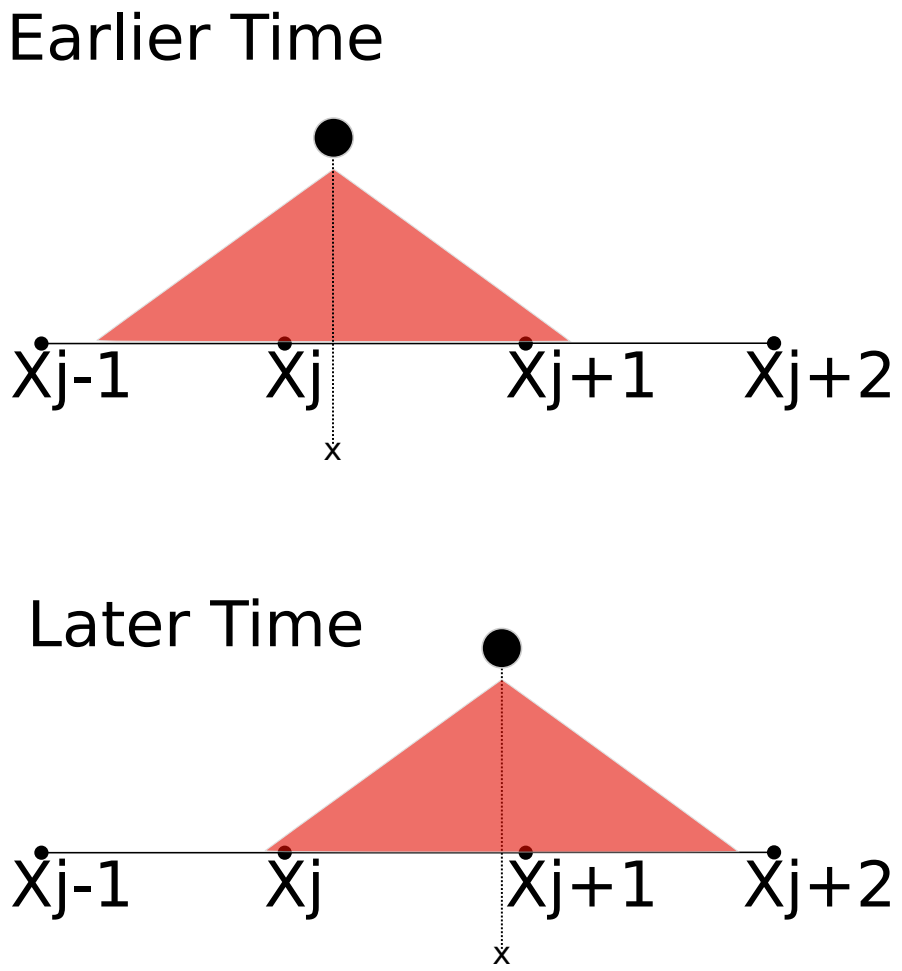

FIGURE 3.4: The effective shape of a particle at position x as seen by the grid. At the earlier time the majority of the particles charge is deposited to the X_J grid point as this is the particles nearest grid point. At a later time the particle has advanced and now deposits most of its charge to grid point X_{J+1}.

Typical plasmas are considered weakly coupled systems as they have a large number of particles in a given cube of volume λ_D^3. This means the trajectory of each particle is affected by a very large number of particles, so the trajectory is smooth as many particles contribute to the electric field. Effects from close encounters with other particles do not dominate particle motion. A strongly coupled system on the other hand is one in which there are few particles per Debye length. The trajectory of a particle is then strongly affected by a collision with another particle and the electric field is noisy and irregular. PIC codes manage to replicate the physics of real plasmas despite using fewer particles by using finite sized particles. Finite sized particles interact more weakly during close encounters than the point size particles of a real plasma. Once finite size particles begin to overlap, the force they exert on each other decreases, reaching zero once the particles fully overlap [62]. By reducing the interaction amongst particles, PIC codes can successfully model weakly coupled plasmas.

3.4 Particle Injection

3.4.1 Particle Loading and Injection

In Langmuir probe simulations, and any other plasma discharge simulation, particles are lost to the various collecting surfaces and must be replaced so that a constant density plasma can be simulated. It is therefore necessary to include an additional step into the PIC cycle, in which new particles are introduced into the simulation, so that the simulation can converge to a steady state. This step is referred to as particle injection. Particle injection often occurs on one side of the simulation domain. For clarity, particle loading only occurs at the very beginning of the simulation to distribute plasma throughout the domain, after the initial particles are loaded into the simulation the loading algorithm will not be used again. Particle injection takes place continuously, throughout the duration of the simulation, at the end of the PIC cycle, once all other existing particles have been moved. It is desirable to inject particles at a rate that conserves the plasma density specified at the beginning of the simulation, however, it is not a necessity. The simulation will reach a steady-state density once the particle injection rate is balanced by the outflow rate of particles. The number of particles that must be injected per time step to maintain a constant density plasma can be estimated as

$$R_{constant-density} = v_{th,s}\Delta T N/\Delta x \tag{3.31}$$

where $v_{th,s}$ is the thermal velocity of the species, ΔT the size of the time step, N the number of particles per cell specified at the beginning of the simulation and Δx the grid spacing. The thermal velocity of the species is given by

$$v_{th,s} = \sqrt{\frac{eT_s}{m_s}} \tag{3.32}$$

where T_s and m_s are the temperature and mass of the species respectively. $R_{constant-density}$ gives the number of particles that must be injected per time step in order to preserve the specified plasma density. The number will be different for electrons and ions as electrons move across grid cells in much less time due to their low mass, leading to a higher thermal velocity.

Langmuir probe theory is based on the assumption that the electrons and ions have a Maxwellian velocity distribution. Multiple algorithms exist to generate Maxwellian velocity distributions and these are detailed in Chapter 16 of Birdsall [60]. A velocity distribution generated with such an algorithm is shown in figure 3.5. The simulation will be required to run for many thousands of time steps in order to reach a steady state solution. For Langmuir probe simulations, the requirements of an effective particle injection algorithm are to ensure the probe samples a constant temperature and density plasma, as a Langmuir probe in a real plasma would. The algorithm must preserve the specified particle density and conserve the Maxwellian velocity distribution of particles. The former requirement is simply met by injecting particles at the rate at which they

move across grid cells as given by equation 3.31. The latter requirement is not so easily met. PIC simulations model a small region of the plasma and use superparticles to sample the velocity distribution. There are orders of magnitude in the difference between the number of superparticles followed and the number of particles present in a real plasma. Therefore, losses of superparticles in a PIC simulation can dramatically change the velocity distribution over very short time scales. The problem is often enhanced by the lack of collisions in fusion-relevant PIC simulations. Due to the high densities and low temperatures of a SOL plasma, PIC simulations can only feasibly model small regions of the plasma. The dimensions of the simulation region are often smaller than any collisional mean free paths, so particles are able to move across the whole domain without experiencing a collision. Collisions drive particles towards Maxwellian distributions. Without this restoring force it is of crucial importance to sample from the correct velocity distribution during particle injection.

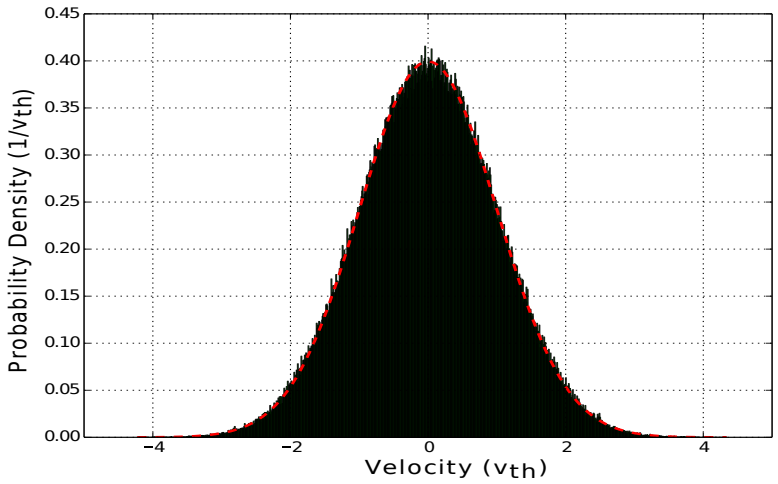

FIGURE 3.5: The velocity distribution of particles generated by the Maxwellian source function. Velocities are expressed in terms of the thermal velocity (v_{th}).

In early simulations, particle loading at the beginning of the simulation and particle injection throughout the simulation both sampled the same source function. For every particle, a random velocity was sampled from a Maxwellian distribution. However, it was found in practise that this did not conserve the Maxwellian distribution. With increasing simulation time, the velocity distribution of the particles in the domain narrowed, resulting in an artificial 'cooling' of the plasma. The initial velocity distribution of particles and the distribution after many time steps is shown in figure 3.6. Although not anticipated, the reasons for this observation are simple. Particles are initially loaded into the simulation domain with a range of velocities all sampled from a Maxwellian distribution. Provided there are enough superparticles in the domain, the distribution will be sufficiently represented by the finite number of particles. As time advances, particles exit the simulation once they reach an absorbing boundary layer and new particles enter in the injection phase of the PIC cycle. The fastest particles in the simulation are,

on average, the first to leave as they quickly move across the domain to an absorbing surface. However, if the injected particles are also sampled from the same Maxwellian distribution then it is far more likely that the injected particle will have a velocity close to zero rather than a high velocity in the tail of the distribution. As a result, the fastest particles leave the simulation quickly to be replaced by slow moving particles that reside in the simulation for a long time. This results in an under representation of the fastest particles in the simulation. The high energy tail disappears, the distribution narrows and the effective temperature of the plasma cools. Ideal probe theory assumes a constant temperature, Maxwellian plasma. Experimental measurements generally work on this assumption too. It is not possible to compare experimental data with simulation results if the simulation plasma is not at a constant temperature. A source function that conserves temperature as the simulation runs is desired. This source function must replace the particles at a rate proportional to their velocity. The fastest particles are required to be replaced more often while the slow moving particles not so much. Rather than the Maxwellian distribution that peaks at $v = 0$ the new distribution must fall to zero at this point as those particles should never leave the simulation. A method to investigate the required shape of the source function was established.

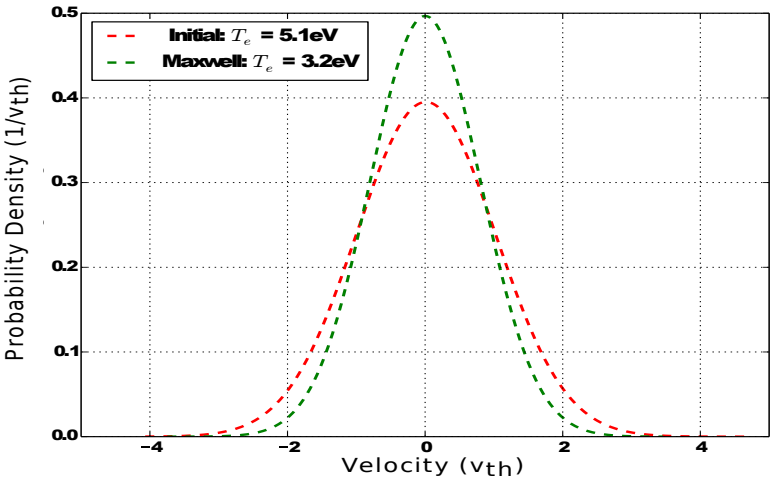

FIGURE 3.6: The initial velocity distribution of the particles compared to the final distribution. Velocities for particle injection were sampled from a Maxwellian distribution.

3.4.2 Temperature Conserving Source Function

A 1D simulation was adequate for the purposes of identifying the correct source function to use. The simulation domain is shown in figure 3.7.

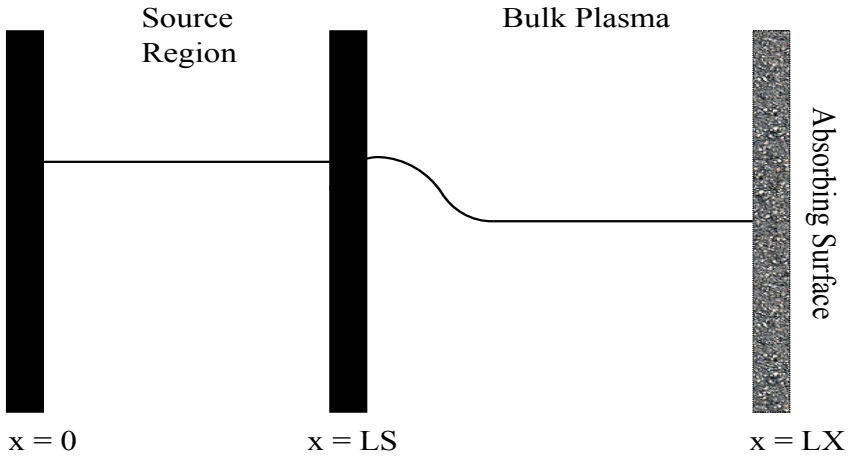

FIGURE 3.7: The simulation domain used to determine the temperature conserving source function. Particles born into the source region cannot escape the simulation. Before reflecting off the $x = LS$ plane, source particles are cloned. This clone escapes the source region and replenishes particles lost in the bulk plasma. A slight decline in plasma density is observed outside the source region compared to the density inside the source region. This is due to the effects of the source sheath.

The model tracks a length of plasma, hundreds of Debye Length (λ_D) long and follows the motion of all ions and electrons as they move in self-consistent electric fields. The presence of a magnetic field impacts the source function so, to begin with, simulations without a magnetic field were carried out. On one side of the domain is an absorbing surface that represents the probe. This surface can be held to any potential. Any charged particles that hit the surface are deleted from the simulation and their current recorded. On the opposite side of the domain is a source region of plasma. The purpose of this source region is to supply the bulk plasma with new particles to replenish those lost to the sides. At the beginning of the simulation, a quasineutral plasma with a Maxwellian distribution fills the entire domain. Any particles born into the source region ($0 \leq x \leq LS$) are trapped in the source region for the duration of the simulation. These source particles travel back and forth in the source region and are reflected at the boundaries $x = 0$ and $x = LS$. Any particles from outside the source region ($x > LS$), that reach the source layer boundary are deleted from the simulation. Both edges of the source region are held at the same potential (V_{source}) which fixes the plasma potential. As there is no potential difference between the two sides and no particles can escape, the plasma source remains at the temperature and density specified at the beginning of the simulation.

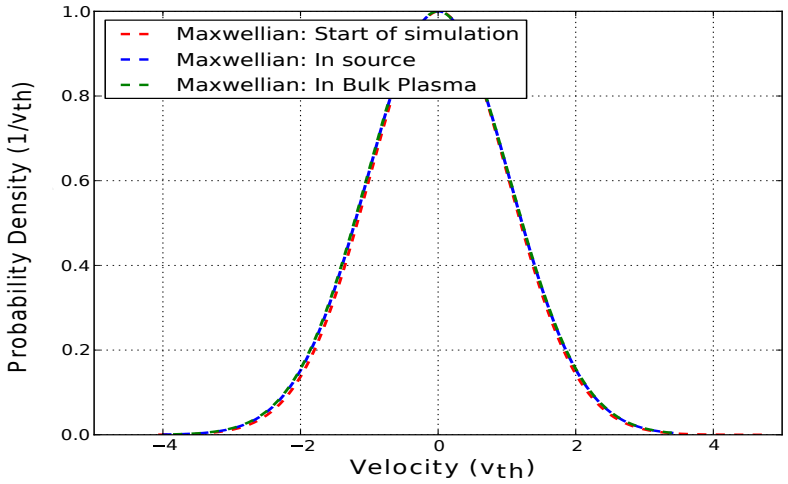

FIGURE 3.8: The velocity distribution of particles in different regions of the plasma at the end of the simulation. The Maxwellian distribution is conserved.

Any source particle striking the $x = LS$ boundary is copied before being reflected. This copy is identical to the original particle, having the same charge, mass, position and velocity but is not reflected at the source boundary. Instead, the copy travels into the bulk plasma, allowing the source region to replenish the bulk plasma. As a result, both the source plasma and the bulk plasma maintain the Maxwellian distribution throughout the duration of the simulation as shown in figure 3.8. The source boundary marks a transition region. In the source plasma, ions have a Maxwellian velocity distribution and travel in both directions along the x-axis. However, outside the source region, ions only move towards the absorbing surface, the backward moving part of the ion velocity distribution isn't represented. There are also more electrons arriving at the source boundary and being copied than there are ions due to the higher mobility of the electrons, there is therefore a charge imbalance just outside the source boundary. These two effects lead to a source sheath, a region of electric field in the source region. The source sheath only spans approximately ten grid cells. After this transition region, the plasma settles to a quasineutral state, at the specified temperature, with zero electric field but at a slightly lower density than that of the source region. The change in density is not significant but it must be taken into account when analysing the current collected by the probe. By looking at the velocity distribution of particles exiting the source, it is possible to determine the form of the source function required to conserve a Maxwellian plasma. The distribution of particles leaving the source region is equivalent to the distribution of particles that would exit the simulation of a bulk plasma. It is these velocities that must be sampled in order to maintain a constant temperature plasma. The velocity distribution of particles leaving the source region is shown in figure 3.9

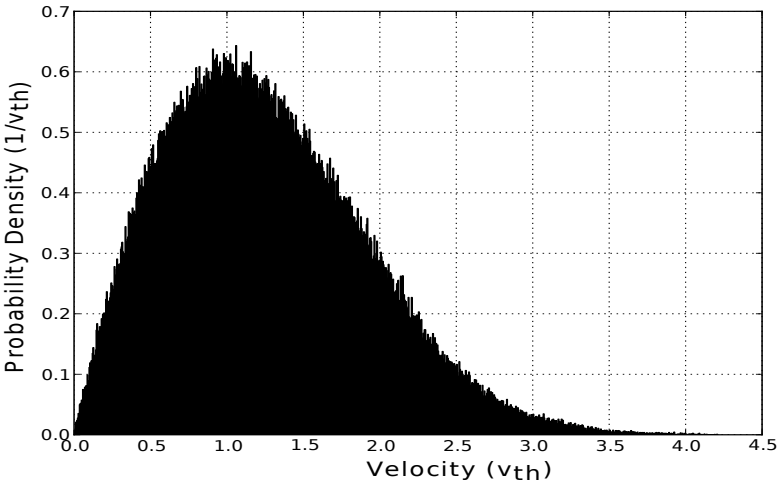

FIGURE 3.9: The velocity distribution of particles that exit the source region.

This distribution is described by the Emmert source function [63] which is given by

$$S_(v) = \frac{mv}{eT_s} exp\left(-\frac{mv^2}{2eT_s}\right) \tag{3.33}$$

The shape of the source function generated from equation 3.33 is shown in figure 3.10.

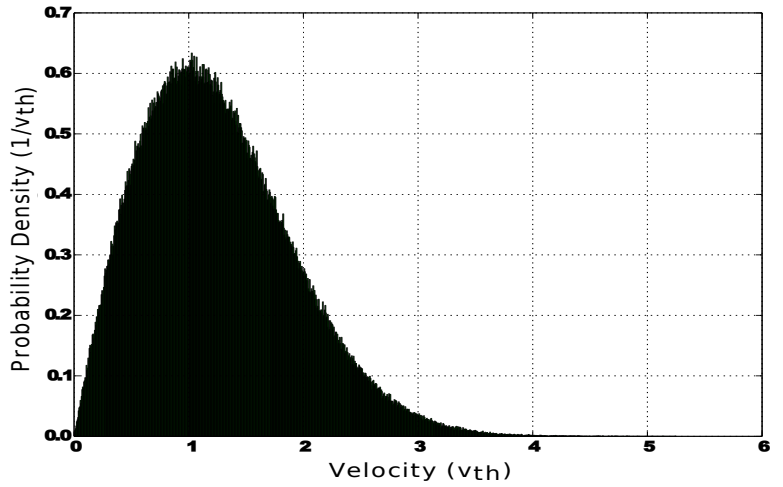

FIGURE 3.10: The Emmert source function only replenishes the high energy tail of the distribution. It is identical to the distribution of particles that escape the source region.

As well as providing a source function, this method validated the rate of injection. It was found that the ratio of electrons exiting the source to ions exiting the source region was equal to the ratio of their thermal velocities. With a temperature conserving source function, to sample velocities from, for the particle injection step, there is no need for the large, reflecting source region. Simulating a large source region requires tracking many particles, which is feasible in 1D simulations but not for simulations with

a greater number of dimensions. The simulation domain without the reflecting source region is shown in figure 3.11.

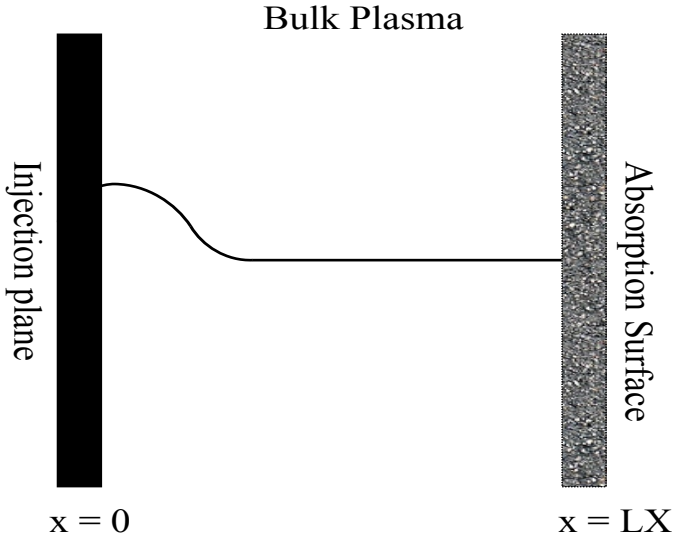

FIGURE 3.11: The domain for the 1D probe simulations used to test the source function. Particles are injected at the injection plane with velocities sampled from the Emmert distribution.

A plasma source is required to replenish particles that are lost to the probe. This source can be held at any potential, this sets the plasma potential. Ions and electrons are injected at every time step at the injection plane with a velocity towards the absorbing surface. Electrons that are reflected by the absorbing surface and return to the injection plane are deleted from the simulation. The rate of injection is given by equation 3.31. The system reaches a steady state over a few ion transit times at which point the current drained by the probe surface reaches a constant value and the plasma density stabilises.

3.4.3 Generating a Velocity from a Source Function

The Emmert source function is described by equation 3.33. The source function is a cumulative distribution function. As this distribution function is invertible it can be used to generate a velocity. The distribution is in the form of a Weibull distribution

$$W(v) = \alpha\beta v^{\beta-1} \exp\left(-\alpha v^{\beta}\right) \tag{3.34}$$

with $\beta = 2$ and $\alpha = \frac{m}{2eT_s}$. By applying the fundamental transformation law of probabilities, it is possible to use a randomly generated number x, where $0 \leq x \leq 1$, from a uniform distribution and transform this into a randomly generated number belonging to the Weibull distribution. For two probability distribution functions $p(x)$ and $S(v)$, the fundamental transformation law states

$$|p(x)dx| = |dS(v)dv| \tag{3.35}$$

or

$$S(v) = p(x)\left|\frac{dx}{dv}\right| \tag{3.36}$$

as x is from a uniform distribution, $p(x)$ is constant and so

$$S(v) = \left|\frac{dx}{dv}\right| \tag{3.37}$$

therefore

$$x = \int_0^v S(v)dv \tag{3.38}$$

Integrating the Weibull distribution gives

$$x = 1 - \exp\left(-\alpha v^{\beta}\right) \tag{3.39}$$

Inverting this gives a relation for the velocity in terms of the random number x

$$v = \left[-\frac{1}{\alpha}\ln(1-x)\right]^{\frac{1}{\beta}} \tag{3.40}$$

Substituting in values for α and β gives

$$v = \left[\frac{-2eT}{m}\ln(1-x)\right]^{\frac{1}{2}} \tag{3.41}$$

3.5 Langmuir Probe Simulations

3.5.1 Reproducing Ideal Probe Theory

In order to test the suitability of PIC codes to the study of Langmuir probe behaviour, multiple simulations were carried out to reproduce predictions made from ideal probe theory. These simulations were first carried out using a 1 dimensional PIC code. This code was written in C, at the beginning of the project, in order to gain an understanding of PIC codes. Due to the complexities involved in developing a fully three dimensional, parallelised PIC code, the decision was made to move to a readily available code for more complex simulations. VSim was found to have all the functionalities required for PIC simulations of a Langmuir probe in a magnetised plasma. The simulations of ideal probe theory were reproduced in VSim and the results of these are presented in this chapter. The main equations of ideal probe theory will now be summarised before simulation results are presented. A complete description of ideal probe theory can be found in Chapter 2. In experiments, a probe I-V curve is produced by sweeping the voltage across the probe (V_{probe}) and measuring the collected current for each voltage. The total current reaching the probe (I_p) will be the sum of the electron (I^-) and ion (I^+) currents to the probe.

$$I_p = I^+ + I^- \tag{3.42}$$

The magnitude of these currents will vary with the applied probe voltage. If the probe is biased negatively with respect to the plasma potential (Ψ) then ions will be collected at their saturated value and only the portion of the electron population with sufficient energy to overcome the negative bias will be able hit the probe. As the probe bias becomes more negative, less of the electron population can reach the probe. Eventually, no electrons reach the probe and the probe only collects the ion saturation current given by

$$I_{sat}^{+} = n_{se} e c_s A \tag{3.43}$$

where n_{se} is the ion density at the sheath edge, e is the fundamental charge and A the collection area of the exposed probe tip. If the probe is biased sufficiently positively with respect to Ψ no ions will be able to reach the probe. The current collected by the probe is then the electron saturation current given by

$$I_{sat}^{-} = \frac{1}{4} n_s e \sqrt{\frac{8eT_e}{\pi M_e}} \tag{3.44}$$

Provided the probe is biased negatively with respect to the plasma potential, the current to the probe will consist of the ion saturation current plus a reduced electron current

$$I_p = I_{sat}^{+} + I_{sat}^{-} \exp\left(\frac{V_{probe} - \Psi}{T_e}\right) \tag{3.45}$$

I_{sat}^{+} can be deducted from the total current, leaving just the contribution from the electrons. This can be rearranged to simplify the measurement of T_e.

$$\ln(I^{-}) = \frac{V_{probe}}{T_e} + \ln(I_{sat}^{-}) \tag{3.46}$$

Taking $\Psi = 0$. By plotting the natural logarithm of the electron current against the probe bias and measuring the gradient it is possible to use probe measurements to determine the electron temperature. With a source function that preserves the specified plasma temperature, simulations should be able to reproduce this important prediction of probe theory. Multiple simulations were run using the domain as shown in figure 3.11. The absorbing surface represents a Langmuir probe. In each simulation a different bias voltage was applied to the absorbing surface. The simulations were run to a steady state in which the currents absorbed by the surface reached a constant value. For each voltage, the electron and ion current reaching the surface was recorded. The source temperature of the electrons and ions was set to 5eV. Using ideal probe theory allowed the correct temperature to be measured by the simulated probe as shown in figure 3.12.

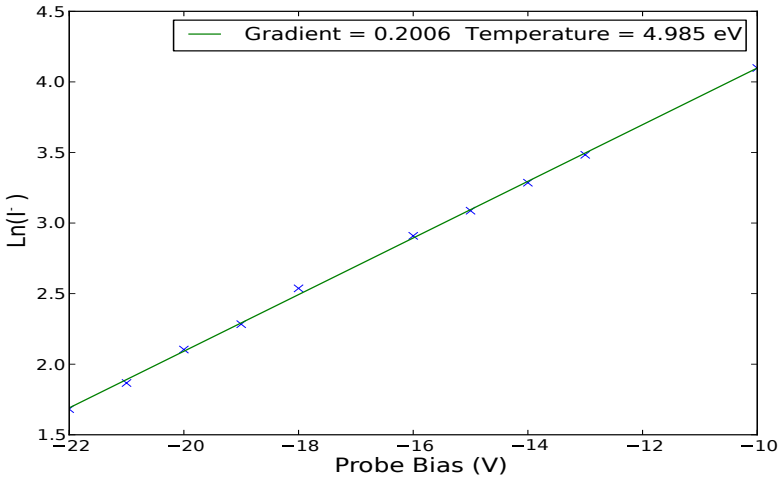

FIGURE 3.12: The log of the electron current against probe bias voltage for the Emmert source function. The gradient of the natural log plot is equivalent to the reciprocal of the electron temperature. Using the Emmert source function to inject new particles allows the probe to measure the correct source temperature.

For comparison the simulations were repeated using the Maxwellian source function rather than the temperature conserving Emmert function to inject particles. As can be seen in figure 3.13 the probe measures a lower electron temperature, a consequence of the narrowing of the velocity distribution.

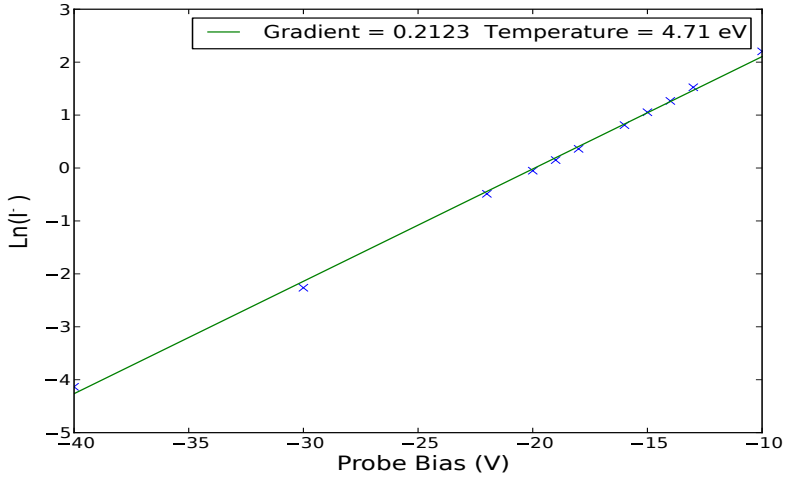

FIGURE 3.13: The log of the electron current against probe bias voltage for the Maxwellian source function.The gradient of the natural log plot is equivalent to the reciprocal of the electron temperature. Using the Maxwellian source function to inject new particles results in the probe measuring a temperature that is lower than the specified source temperature.

Figure 3.14 compares the velocity distribution of the electrons at the end of simulation when sampling from each distribution. It is clear that the correct temperature is conserved when sampling from the Emmert source function but a loss of temperature

is detected when using the Maxwellian function. For the Maxwellian runs, the probe measured a temperature somewhere in between the original specified temperature and the final plasma temperature.

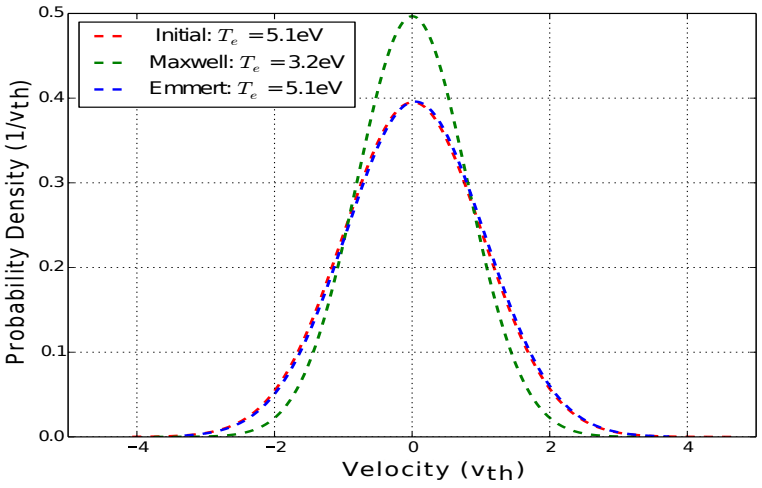

FIGURE 3.14: A comparison of the electron velocity distributions. Red - The distribution of electrons at the beginning of both simulations. Green - The electron distribution at the end of the simulation using a Maxwellian source function. Blue - The electron distribution at the end of the simulation using the Emmert source function.

The ability to reproduce ideal probe theory confirms the correct choice of source function. This was a crucial starting point. With a reliable source function, scenarios with more complicated physics can now be explored.

3.5.2 Source Function for Magnetised Plasmas

In order to simulate Langmuir probes in fusion plasmas, a magnetic field must be added to the simulations. The magnetic field has components along each coordinate axis, B_x, B_y and B_z, even in a simulation with one spatial domain. The magnitudes of these components determine the angle the magnetic field makes with the axes. In the simulations presented in this thesis, $B_z = 0$. The angle the field makes with the y-axis (θ) is given by $\theta = \tan^{-1}\left(\frac{B_x}{B_y}\right)$.

In the previous simulations, without a magnetic field, it was found that the Emmert source function was correct to use in the x-direction as the rate at which particles were lost to the probe was directly proportional to the v_x component of their velocity. For a simulation with one spatial dimension and three velocity dimensions (1D3V), v_y and v_z are sampled from a Maxwellian distribution, this produces the same results as presented in the previous section. The presence of the magnetic field, which does not have to lie along one of the Cartesian axis, adds an additional step to the particle injection algorithm. Particle velocities are generated relative to the magnetic coordinates, parallel to the field lines ($v_{\parallel}$) and the two perpendicular directions ($v_{\perp,1}$ and $v_{\perp,2}$). These velocities must then be transformed so that they lie along the coordinate axis. In a

magnetised plasma, the rate at which particles are lost to the wall now depends on their parallel velocity so this velocity should be generated from the Emmert distribution. The two perpendicular velocities are again generated from Maxwellian distributions. The field orientated velocities $v_{\parallel}, v_{\perp,1}$ and $v_{\perp,2}$ are then converted to Cartesian velocities v_x, v_y, v_z by the following transformations [64].

$$v_x = v_{\parallel} b_x + v_{\perp,2}\sqrt{b_y^2 + b_z^2} \tag{3.47}$$

$$v_y = v_{\parallel} b_y + \frac{v_{\perp,1} b_z - v_{\perp,2} b_x b_y}{\sqrt{b_y^2 + b_z^2}} \tag{3.48}$$

$$v_z = v_{\parallel} b_z - \frac{v_{\perp,1} b_y + v_{\perp,2} b_x b_z}{\sqrt{b_y^2 + b_z^2}} \tag{3.49}$$

where

$$b_x = \frac{B_x}{B} \tag{3.50}$$

$$b_y = \frac{B_y}{B} \tag{3.51}$$

$$b_z = \frac{B_z}{B} \tag{3.52}$$

These transformations have been tested to ensure they generate correct parallel velocities for the particles. The presence of the magnetic field complicates the way particles are injected into the simulation. In simulations without a magnetic field, if a particle hit the injection plane it was deleted from the simulation, as it was moving away from the absorbing surface and out of the simulation domain. However, particles now gyrate around magnetic field lines, which may run near parallel to the y-axis. The orbit of the particle around magnetic field lines could take it beyond the injection plane even though its parallel velocity is still headed towards the absorbing surface. In order to avoid deleting these particles, a buffer region is added to the simulation domain. This region needs to be at least one ion Larmor radius (ρ_i) in width. The potential across the buffer region is fixed to zero such that there is no electric field. If a particle enters the region due to its orbit, the particle will carry on its orbit and re-enter the simulation domain. If a particle is reflected by the absorbing surface and travels backwards into the buffer region, it will travel to the beginning of the simulation domain where it will then be deleted from the simulation. A typical 2D simulation domain is shown in figure 3.15.

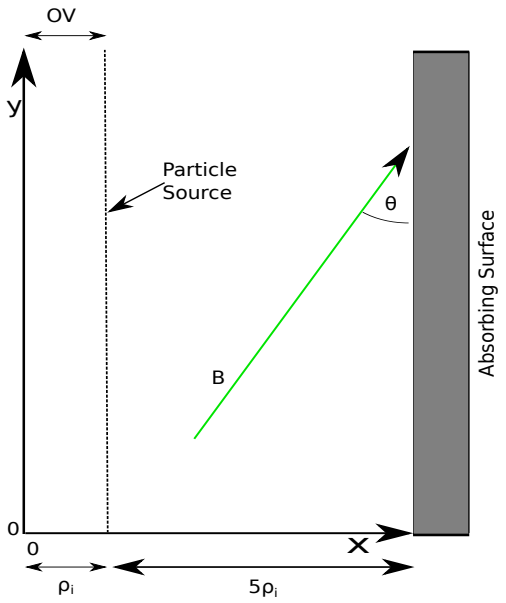

FIGURE 3.15: A typical two dimensional simulation domain. A buffer region of width $\geq 1\ \rho_i$ is added to the start of the simulation to avoid deleting gyrating particles. Particles are injected on the boundary of the buffer region and the simulation domain.

Simulations with magnetic fields capture the magnetic pre-sheath but not the pre-sheath. This region is too large to be covered by PIC simulations

3.5.3 Floating Wall Conditions

In simulations of Langmuir probes it is desirable to implement floating surfaces to represent a probe operated in floating mode or a surrounding divertor tile. To include floating boundary conditions in VSim requires the use of heavy particles. These are particles with the same charge as that of an ion or an electron but a mass that is sufficiently large such that the particle will not move due to the forces imparted upon it, throughout the duration of the simulation. A mass of 1 kg is sufficient. If a particle comes into contact with a floating surface in the simulation, the particle is deleted from the simulation. A heavy particle is then emitted at this point of absorption, so the charge of the absorbed particles build up on the wall. A charge and electrostatic potential naturally build up on the floating surface this way without having to impose a floating potential. To test this boundary condition a simulation was carried out with the simulation domain used in section 3.5.1. Instead of biasing the right hand side of the simulation to a set probe bias potential, the wall now absorbed particles that hit it and re-emitted heavy particles in their place. The simulation was run until the wall reached a constant potential and drained a steady current. The current and potential on the wall agree well with what is expected based on the electron temperature as shown in figure 3.16.

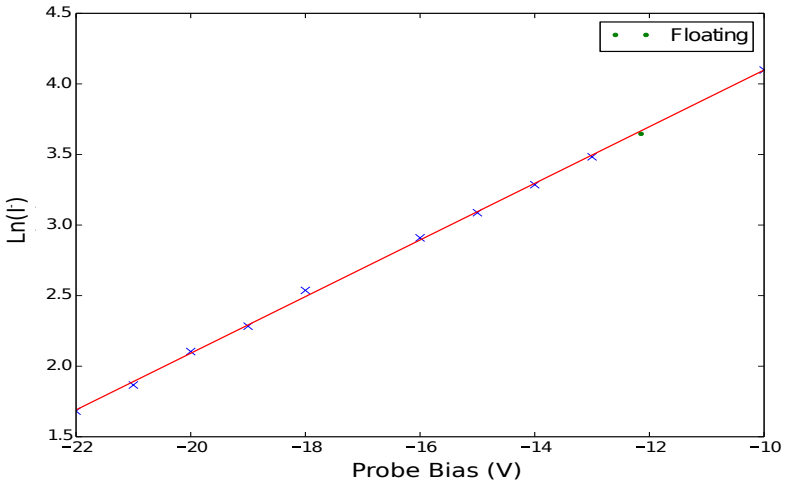

FIGURE 3.16: The green circle represents the floating potential and current drained by the probe using the heavy particle floating boundary condition.

A 2D3V simulation was carried out using the domain presented in figure 3.15. The ions had a mass of 900 m_e. Both species had a temperature of 6 eV. The absorbing surface was found to float at -12.83 V below the plasma potential. Which is in good agreement with the theoretical prediction for V_F presented in Chapter 2, equation 2.24.

3.5.4 Assumptions in the Model

In the simulations presented in this thesis, there are no collisions between the charged particles. Typical plasma parameters used in the simulations are of the order $n_e \approx 1 \times 10^{18}$ m^{-3} and $T_e \approx 10$ eV. The simulation domain usually spans no longer than 5 mm in either direction. The demand that the grid must resolve the Debye length means it is not feasible to simulate larger lengths than this as the required amount of grid points will be too computationally demanding ($\lambda_D \approx 10^{-5}$ m). The mean-free path (λ) for both electrons and ions is calculated to far exceed the length of typical simulation domains for the plasma parameters. Using equations from Wesson [65] it is calculated that $\lambda_{electron} = 7.2$ cm and $\lambda_{ion} = 10$ cm for the stated plasma parameters. As a result particles can travel across the entire simulation domain multiple times without experiencing a collision. It has also been assumed that there are no neutrals or impurities present so the plasma consists of electrons and singly charged ions.

3.6 Summary

An overview of the general PIC methodology has been presented. The adaptations that are required to simulate a Langmuir probe have been described. A temperature conserving source function was found that conserves the Maxwellian velocity distribution of particles, at the specified temperature, throughout the duration of the simulation. This allows the simulated probe to sample a constant temperature plasma. Measurements of

the electron current reaching the simulated probe were used to accurately measure the specified electron temperature. The simulation model for a magnetised plasma has been introduced. This model will be used to simulate flush-mounted probes in Chapter 4 and ball-pen probes in Chapters 5 and 6.

Chapter 4

Flush Mounted Probes on MAST

4.1 Introduction

Langmuir probes are built into divertor plates such that their surface is flush with the surface of the divertor tiles. Probes in this configuration are known as flush-mounted probes (FMP). These tiles and the FMPs, are capable of surviving the high power flux of the SOL, if the magnetic field meets the tiles at a grazing angle of incidence, as this spreads the flux over a larger area, reducing the thermal load on the probe surface [66]. As has been discussed previously in Chapter 2, interpretation of Langmuir probe measurements in strongly magnetised plasma is complicated by the influence of the magnetic field on charged particle collection. In a strong magnetic field, the collection area of the probe (A_{eff}), is reduced from the surface area of the probe (A) to the projected area of the probe along the field ($A_{eff} = Asin(\theta)$), where θ is the angle between the magnetic field and the probe surface. For a standard Langmuir probe inserted into a plasma, A_{eff} is relatively easy to calculate. A measurement of the ion saturation current and the electron temperature can then be used to determine the electron density, as can be seen in equation 4.1

$$I_{sat} = n_e e A_{eff} c_s \tag{4.1}$$

Due to the grazing angle of incidence the magnetic field makes with the divertor tiles, the FMP configuration provides further complications to the interpretation of the measurements. At grazing angles of incidence, the effective collection area of the probe is reduced significantly and can be comparable to the area of the sheath in front of the probe. The Child-Langmuir law, equation 4.2, states that the thickness of the sheath (s) in front of the probe depends on the bias voltage (V_{probe}), increasing as the probe is biased more negatively relative to the surrounding tiles [67], [68].

$$s \propto \lambda_D \left(\frac{V_{probe}}{T_e} \right)^{\frac{3}{4}} \tag{4.2}$$

Ions that enter the sheath are drawn to the probe by the strong electric fields present in this region. With increasingly negative bias voltage, the sheath size expands and so does the effective collection area of the probe. As a result, current-voltage (I-V) characteristics obtained from FMPs, deviate from the ideal characteristics derived from the one-dimensional model presented in Chapter 2, with non-saturation of the ion current often observed [69]. An example of an I-V curve obtained by a FMP is shown in figure 4.1. Standard probe theory cannot be used to interpret FMP measurements [70]. Applying the conventional analysis procedure to FMP data yields temperatures and densities that are too high [70], as the non-saturation of the ion current at highly negative voltages is interpreted as a still present, but declining electron current by the fitting algorithm. In order for FMP measurements to return more accurate estimates of the plasma parameters, the effective collection area of the probe must be known.

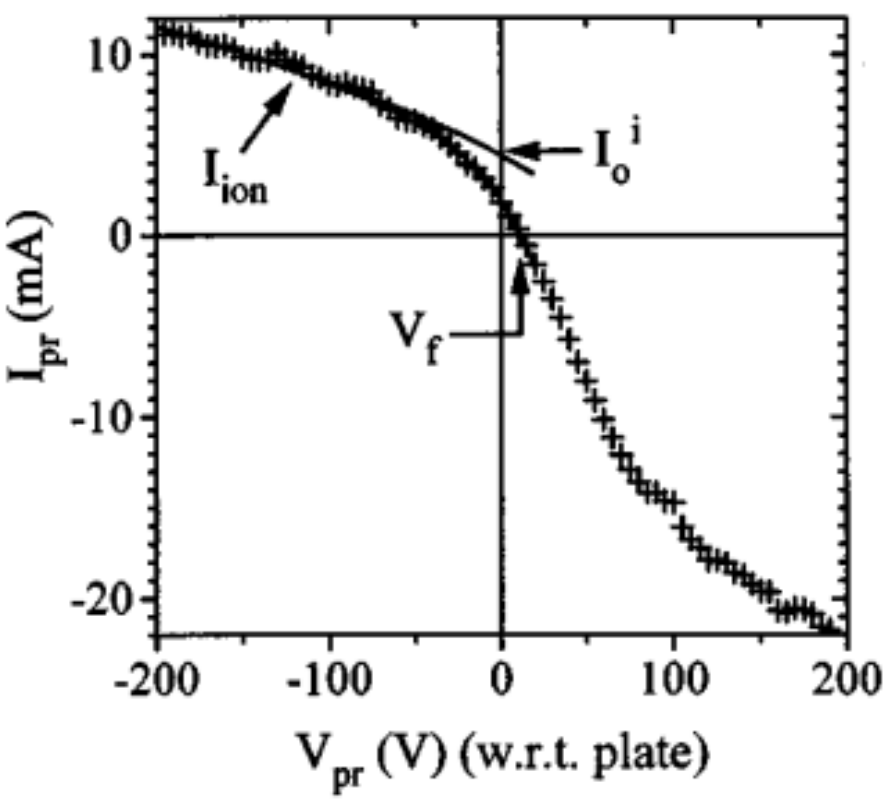

FIGURE 4.1: A FMP I-V characteristic. Taken from [66].

4.2 Overview of FMP theory

It is clear for FMPs that the area of the sheath cannot be neglected, as it often is for probes in the standard configuration. The effective area for a FMP consists of the geometrical projection of the surface area of the probe and the area of the sheath in

front of the probe, which will increase with voltage applied to the probe

$$A_{eff} = A \sin\theta + A_{sheath} \tag{4.3}$$

This assumes that due to the strong electric fields present in the sheath, any ions that enter the sheath will be collected by the probe.

Models of ion collection by FMPs have been developed that take into account the increasing size of the sheath as the probe is biased more negatively. Early modelling attempts included a non-linear term to account for the Child-Langmuir expansion, obtaining an equation for A_{sheath} of the form

$$A_{sheath} = w \times s = wk\lambda_D \left(\frac{V_{probe}}{T_e} \right)^{\frac{3}{4}} \tag{4.4}$$

Here, w is the width of the sheath, which is taken to be the probe width, s is the sheath thickness and k is the constant of proportionality in the Child-Langmuir law. The new value for A_{eff} is then substituted into equation 4.1, obtaining a new equation that could then be fitted to the slope of the ion current to extract the plasma parameters.

These early models correctly predicted that the sheath in front of the probe would be larger than the sheath in front of the floating tiles either side of it. However, they neglected the complex sheath structure in a magnetised plasma and the exact trajectories of ions moving through these transitional sheath layers. As discussed in Chapter 2, the transition region in a magnetised plasma consists of three layers, the quasi-neutral pre-sheath, the magnetic pre-sheath (MPS) and the Debye sheath (DS). Ions enter the MPS with parallel velocity along the field lines exceeding the Bohm speed and exit the MPS with speeds normal to the surface exceeding the Bohm speed. From current continuity, neglecting transport perpendicular to the magnetic field, the following equation is obtained [71]

$$n_{mps}\ c_s \sin\theta = n_{ds}\ c_s \tag{4.5}$$

Where n_{mps} and n_{ds} are the densities at the entrance to the MPS and DS respectively. It can be seen from equation 4.5 that the density at the entrance to the DS is significantly lower than that at the MPS entrance for grazing angles of incidence. As a result of this density drop, the thickness of the sheath, which scales with Debye length, in front of the probe and the floating wall can be greatly enhanced compared to the unmagnetised case.

An analytical fluid model that incorporated the MPS density drop was developed by Weinlich and Carlson in order to understand the lack of saturation of the ion current [72]. This model also considers the trajectories of ions as they move through the MPS and DS. In the Weinlich and Carlson model, the probe sheath was considered to be a rectangular, sharp edged box. Any ion that enters the sheath is drawn to the probe. The model of the sheath is shown in figure 4.2. The probe has a length L and a width w extending into the plane. The probe is biased negatively with respect to the floating

wall around it and so the thickness of the DS in front of the probe is enhanced relative to the DS in front of the wall by an amount s. Ions travel parallel to the field lines until they enter the MPS, at which point they begin to follow a curved trajectory, until attaining a velocity normal to the wall which satisfies the Bohm Criterion, on entry to the DS. For ions that enter the MPS at the same speed, all trajectories in the MPS will be equal in length and shape, regardless of whether ions reach the wall's DS or the probe's. As the probe has a thicker DS, the entrance of the probe's MPS will be shifted upstream. This is illustrated in figure 4.2, where the entrance to the MPS is represented by the dashed lines, corresponding to an upstream image of the DS.

The trajectories, lines 1 and 2, drawn with bold lines, mark the boundaries between ions that make it to the probe and those that hit the wall. Ions following a trajectory in between lines 1 and 2, exit the MPS at the entrance to the probe's DS and hit the probe. Circled on line 2 is a bifurcation point in the trajectory. An ion following a trajectory just outside of line 2 will travel parallel to the field, past the bifurcation point, only turning towards the normal once reaching the MPS entrance of the wall, shown in dashed lines, which is the same fixed distance from the wall's DS as the distance between the MPS and DS of the probe. Therefore, there exists a region of the wall, between the two bifurcated trajectories, that the ions cannot access. A lower current is expected in this region. At the leading edge of the probe, located above line 1 by an amount s at the MPS entrance, is another ion trajectory. This represents ions that would reach the probe due to its projected length, $(L \sin\theta)$, the enhanced thickness of the probe's DS is not relevant to these ions. However, for ions between this trajectory and line 1, the increased sheath thickness allows these ions to reach the probe's DS. Without the sheath enhancement, these ions would hit the wall instead. All ions following trajectories in this region, arrive in the probes DS at the same horizontal position above the probe. The model therefore predicts a focusing effect and hence, an enhancement of the ion current on the leading edge of the probe.

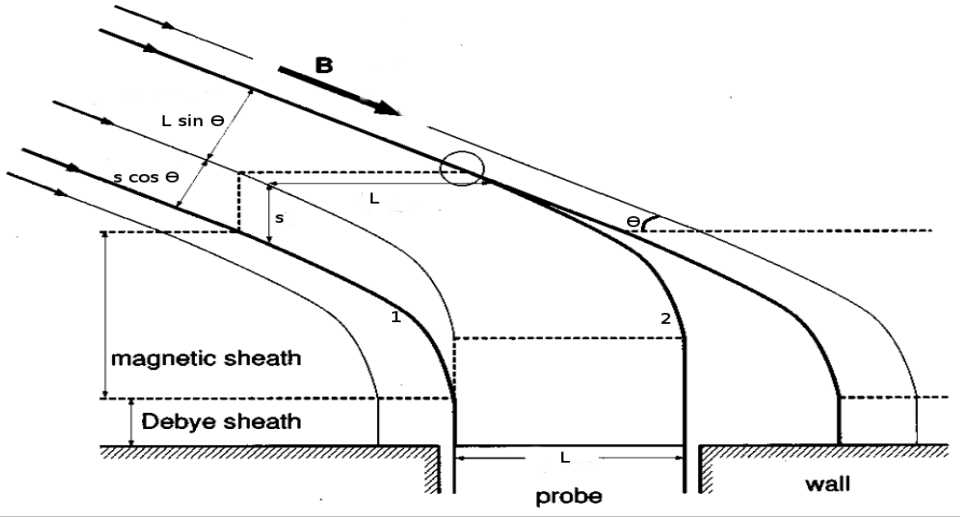

FIGURE 4.2: Model of the sheath in front of a FMP. Taken from [72].

This model does not take into account effects of the finite gyroradius of the ions. In order to capture these effects a kinetic treatment of the ions is required. Detailed, two-dimensional particle-in-cell (PIC) simulations of small FMPs in plasmas with oblique magnetic fields were carried out by Bergmann [73]. The fluid model's predictions of an enhanced ion current to the leading edge of the probe and a depleted current to the wall beyond the trailing edge of the probe were observed in the PIC simulations. The work detailed in [73] and [74] is the foundation of the results presented in this chapter, it is therefore necessary to summarise this work before proceeding to the results.

4.2.1 Summary of Previous Particle-In-Cell Simulations of Flush-Mounted Probes

In [73], the motion of ions and electrons were tracked as they followed magnetic field lines towards an absorbing surface, consisting of a floating wall and a probe that was biased negatively with respect to the floating potential. The probe had a length (L). The simulation domain is shown in figure 4.3. Both ions and electrons are treated kinetically although a guiding centre approximation for the electrons was used to speed up the simulations.

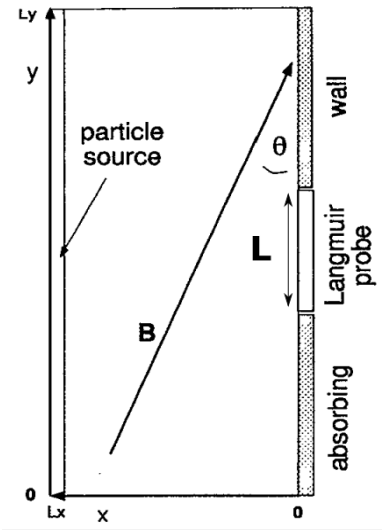

FIGURE 4.3: A representation of the particle-in-cell simulation domain used to model the particle collection of FMPs. Taken from [73].

As with experimental data, the ion current in the PIC simulations was found not to saturate at highly negative voltages. A sheath that scaled with voltage was found to be responsible for this non-saturation. It was found that the sheath thickness in front of the probe (Δ) was described by the following relation

$$\Delta = \Delta_0 + \Delta_1 |V|^{3/4} \tag{4.6}$$

Where V is the bias voltage applied to the probe, relative to the floating wall.

$$V = \frac{V_{wall} - V_{probe}}{T_e} \tag{4.7}$$

Δ_0 is the thickness of the sheath in front of the probe when it is at the floating potential. Δ_1 is a coefficient that takes into account the enhanced thickness of the Debye sheath when the probe is biased more negatively than the surrounding wall. It was found that Δ_0 decreases as $\theta \to 0$, despite the MPS density drop having a larger effect at low angles. For decreasing θ, more of the potential drop is contained in the MPS rather than the DS. As there is less of a potential drop across the DS, the thickness of the DS is reduced. This effect more than makes up for the enhanced Debye length. Δ_1, on the other hand, increases as $\theta \to 0$. It was found that

$$\Delta_1 \approx \frac{0.5\lambda_D}{\sqrt{\sin\theta}} \tag{4.8}$$

The ion focusing effect is more powerful at smaller angles. When the probe is floating, so at the same potential as the surrounding tiles, $V = 0$ and therefore, the sheath thickness in front of the probe is the same as that of the sheath in front of the floating wall ($\Delta = \Delta_0$). As a result, no ion focusing effects are observed, the probe collects a current I_0, which is the current travelling along the flux tube subtended by the probe

$$I_0 = en_e c_s L sin\theta \tag{4.9}$$

Where n_e is the electron density at the entrance to the MPS. The simulations are two-dimensional, which means the probe has a length (L) rather than an area. Here the sound speed is $c_s = \sqrt{(T_e + \gamma_i T_i)/m_i}$. γ_i is the adiabatic index determined by the number of effective degrees of freedom for the ions (f), $\gamma_i = (f+2)/f$. At grazing angles of incidence, f = 2 [74]. For a standard Langmuir probe, where the collection area of the probe is much greater than the sheath area, the sheath area is negligible. As a result, I_0 would be a good approximation for the ion current at all negative voltages up to the plasma potential. This isn't the case for a FMP, where the sheath area is comparable to the effective collection area of the probe. The current to the simulated probes was well described by the following equation

$$I/I_0 = 1 + a|V|^{3/4} - e^V \tag{4.10}$$

The parameter a is directly proportional to Δ_1 which is shown in figure 4.14. a represents the proportion of additional ion current received by the probe due to the enhanced sheath thickness in front of the probe. a is inversely proportional to the probe length. The additional current reaching the probe due to its enhanced sheath thickness is independent of probe length. The additional ion current reaching the probe is then a lower proportion

of the total ion current for a larger probe. In [73], a value for a was derived

$$a = \left(0.5 + 0.4\frac{1-\sin\theta}{\sin\theta}\right)\frac{1}{L\sqrt{sin\theta}} \tag{4.11}$$

However, this derivation used a more complicated sheath model than that presented in figure 4.2. Due to computational demands, simulations in [73] were carried out for small probes, where the ratio of probe length to ion gyroradius was smaller than that in experiments. The complicated model presented in [73] was found to be a good approximation for small probes. The model was later extended to larger probes with realistic ratios of probe length to ion gyroradius [74]. For these larger probes, the rectangular approximation of the sheath was found to be a better representation. For this model, a new sheath expansion parameter was derived

$$a = \frac{c_1 + c_2\cot\theta}{\sin^{1/2}\theta}\frac{\lambda_D}{L} \tag{4.12}$$

The probe sheath expands both in thickness away from the wall and laterally along the length of the wall. c_1 is a coefficient that describes the lateral sheath expansion while c_2 is related to the increased sheath thickness in front of the probe. By plotting $aL\sin^{1/2}\theta$ against $\cot\theta$ it is possible to measure c_1 and c_2. It was found that $c_1 = 0.5$ and c_2 depended on the probe length relative to λ_D, reaching a maximum value of 0.6 once $L \approx 400\lambda_D$. This model was found to explain measurements of the non-saturation of the ion current on ASDEX-Upgrade [74].

In an experiment, there is always a gap between the FMP and the surrounding divertor tiles. The gap exposes the leading side of the probe to plasma and so could increase the effective collection area of the probe. The model in [74] does not take into account the gap. This may not be an issue for the FMPs of ASDEX-Upgrade as the probes deployed measure 5 by 40 mm with the largest side orientated parallel to the magnetic field lines [72] and so the additional current reaching the side of the probe may be negligible. However, the MAST probes are much smaller, with dimensions 2 by 5 mm and a significant probe gap of 1 mm. If there is an additional current to the side of the probe, this would need to be taken into account to extract an accurate plasma density from the measured ion current. To investigate the effects of the probe-tile gap, PIC simulations were carried out with VSim. The remainder of this chapter introduces the simulation model and presents the results of the simulations.

4.3 The Simulation Model

The simulation model has two spatial dimensions and three velocity components (2D3V). A plasma consisting of singly charged ions and electrons is studied. The full gyromotion of electrons and ions is tracked as they move in a self-consistent electric field and a prescribed, homogeneous magnetic field. The domain captures the entire probe length with the probe located at the centre of the domain surrounded by a floating wall. The

simulations model a region of plasma above the probe of width 5 ρ_i to capture the MPS. An additional buffer region of width 1 ρ_i is added to the particle source region. The electric field in this region is zero, this allows particles with velocity parallel to the magnetic field ($v_\parallel$), directed towards the probe-wall interface to complete their gyromotion around the magnetic field without being deleted from the simulation. Particles that are moving away from the probe (with negative $v_\parallel$) that enter this region, travel to the beginning of the domain and are removed from the simulation. A two dimensional slab model of the simulation domain is presented in figure 4.4.

The y axis is treated periodically. Particles follow field lines towards the probe-wall interface. Particles that reach the interface are removed from the simulation. Those that hit the floating wall deposit their charge there allowing a charge density and electrostatic potential to evolve naturally, to a steady state without imposing additional boundary conditions on the walls. The domain is initially filled with a spatially uniform Maxwellian plasma. Particles are injected into the simulation domain at the source region to replenish those lost to the probe and walls. The parallel component of velocity for the particles is sampled from the Emmert distribution [63] as this conserves the plasma temperature in the domain. The two perpendicular velocity components are sampled from a Maxwellian distribution. The potential at the beginning of the domain is set to 0 V and the probe potential is fixed to V_{probe}, the wall evolves to a floating potential (V_F).

The domain is a rectangle in the x-y plane and models the toroidal length of the probe which lies along the y axis. The plasma is assumed to be uniform along the ignored z-axis. The domain has lengths L_x and L_y respectively and the probe has length L. The magnetic field is inclined to the wall by an angle θ where $\tan(\theta) = B_x/B_y$. In these simulations the field is directed in the toroidal direction, along the largest dimension of the probe, there is no poloidal component.

A reduced ion mass (m_i) was used in the simulations equivalent to 900 m_e, where m_e is the electron mass. The reduced ion mass decreases ρ_i which in turn decreases the required length of the simulation domain in the x direction. It also increases the ion sound speed thus reducing the time taken for the simulation to reach steady state. Simulations were carried out with the same probe length to ion gyroradius ratio as in the MAST divertor region, as the simulated gyroradius is less than in experiments, the length of the simulated probe is therefore shorter than in experiments too. The ion gyroradius to Debye length (λ_D) ratio from experiments was also conserved in the simulations. For a typical shot on MAST, the ion gyroradius in the MAST divertor is estimated to be 0.9 mm, but in the simulation, with less massive ions, this is reduced to 0.42 mm. The probe length in the simulations is then reduced from 5 mm to 2.38 mm. The Debye length is also reduced, requiring a small increase in density to conserve the ratio. The simulated densities are still well within the range of values seen in the MAST divertor. Typical simulation parameters are given in table 6.1. The results presented will be for these simulation parameters unless otherwise stated.

Magnetic field strength B	0.41 T
Magnetic field inclination θ	12°
Plasma density n_0	6.4×10^{18} m^{-3}
Electron temperature T_e	6 eV
Ion temperature T_i	6 eV
Ion Larmor radius ρ_i	0.42 mm
Electron Mass m_e	9.11×10^{-31} kg
Ion Mass m_i	900 m_e
Ion Charge Z	1.6×10^{-19} C
Probe Length L	2.38 mm
Debye Length λ_D	7.2×10^{-6} m

TABLE 4.1: Typical plasma parameters used in the simulations of FMPs on MAST.

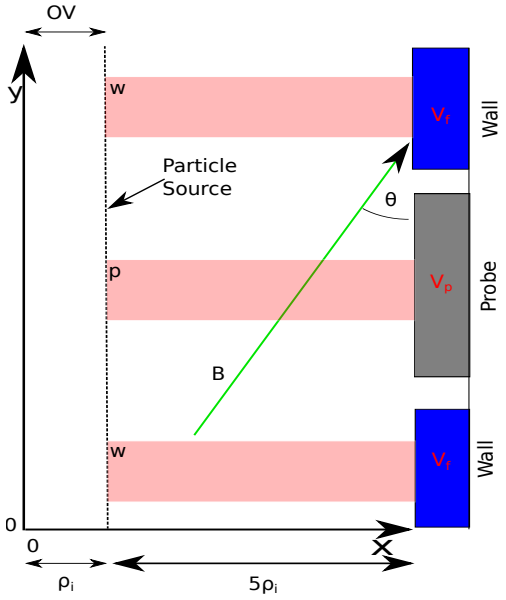

FIGURE 4.4: The simulation domain. Particles are injected in the source region to replenish those lost to the wall. The magnetic field makes an angle θ to the probe surface. An additional Larmor buffer region is included to ensure only particles with parallel velocity moving away from the probe are deleted. The red lines, labelled p and w, are the regions where the density is calculated in front of the probe and wall respectively. These densities are shown in figure 4.5.

Before exploring the effects of the gap on charged particle collection it was necessary to benchmark the model developed in VSim against the simulations carried out in [74]. Simulations without the probe-wall gaps were carried out with VSim. The results of these simulations are presented in the following section.

4.4 Validating the Model

In the VSim simulations a floating potential on the wall develops over time as charge is deposited on the walls by the absorbed particles. This differs from the method deployed

in [74], in which multiple 1-D simulations were carried out to determine the potential at which net zero current reached the wall, this potential was then set as a prescribed boundary condition to the floating walls in the 2-D simulations. Presented in this section are results from VSim using the same simulation domain as that of [74]. These results aid in understanding the particle collection of FMPs and provide a means to benchmark the code. These results are compared to results obtained in both [73] and [74]. The following results are obtained for a plasma of density $n_0 = 6.4 \times 10^{18}\, m^{-3}$, where n_0 refers to the density at the entrance to the MPS, a temperature of $T_e = T_i = 6$ eV, an inclination angle $\theta = 12°$ and a probe bias voltage $V_{probe} = -70$ V.

By plotting the density along lines perpendicular to the wall, the MPS and DS can be easily identified. The variation of density, along the lines labelled p and w in figure 4.4, is shown in figure 4.5. Line p measures the particle densities in front of the probe, these are represented by solid lines in figure 4.5. The two lines labelled w measure the density in front of the floating wall, the two densities are then averaged to produce the dashed lines in figure 4.5.

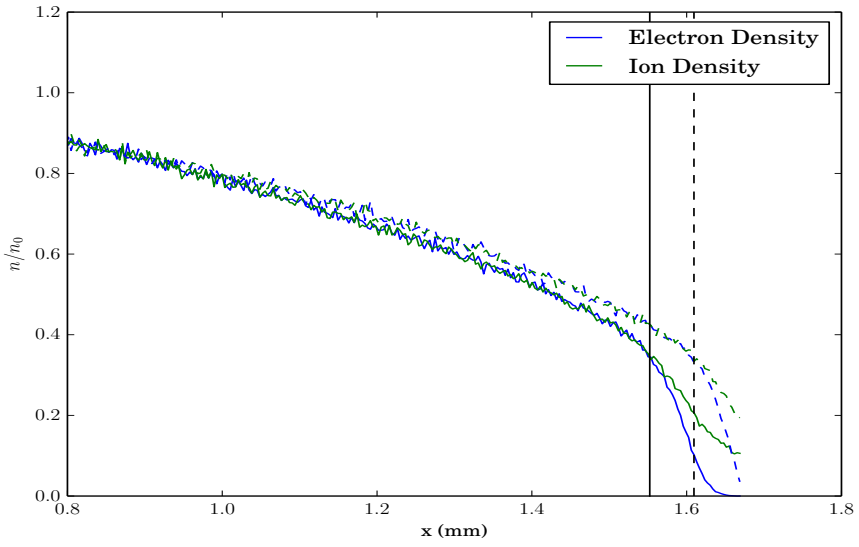

FIGURE 4.5: The ion density (green) and electron density (blue) along a line perpendicular to the wall. Densities are normalised with respect to the density at the entrance to the MPS. Solid lines represent the density in front of the centre of the probe, dashed lines represent the density in front of the floating walls. The vertical lines represent an approximate entrance to the DS, where quasi-neutrality breaks down.

The quasi-neutral MPS can be easily distinguished from the DS where the electron density tends to zero. The black, vertical lines represent an approximate location of the entrance to the DS where quasi-neutrality breaks down. The enhanced thickness of the probe's DS can be seen. The density drop across the MPS is observed for both lines, with the drop occurring earlier in front of the probe. This occurs earlier because the DS in front of the probe is thicker and so the probe's MPS begins further from the wall. The density at the entrance to both Debye sheaths is approximately the same. As has been

discussed, this density drop is a key part of the fluid model [72] and has been observed in PIC simulations [73].

The effect of the enhanced sheath thickness on ion current can be observed in figure 4.6. A large peak is observed at the leading edge of the probe, as ions hit the side of the enhanced DS sheath and are focused on to the probe. The probe is biased sufficiently negatively such that no electrons reach the probe surface. The effects of the bifurcation point in the ion trajectories are observed with a large reduction in current reaching the trailing edge of the probe.

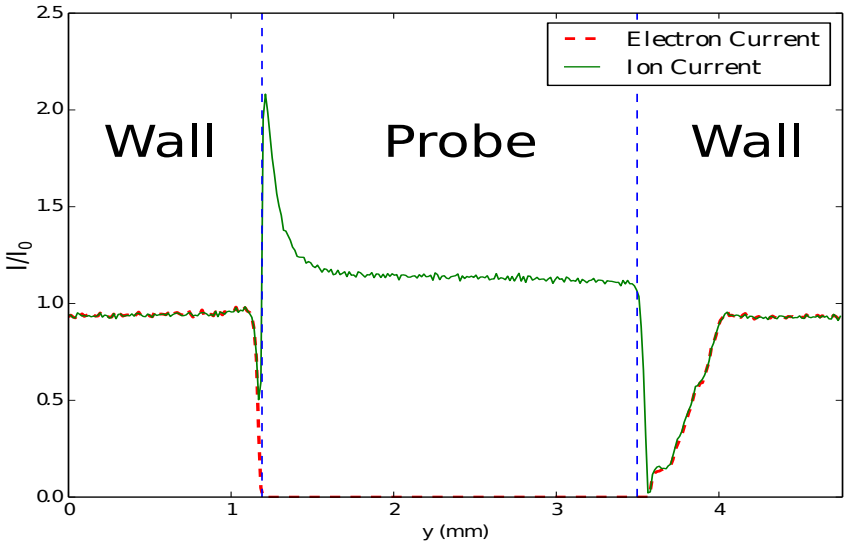

FIGURE 4.6: The ion current (green, solid) and electron current (red, dashed) reaching the wall. The currents are normalised by I_0. The edges of the probe are shown in dashed, vertical lines.

As observed in [73], there is a region behind the trailing edge of the probe, that is depleted of electrons. The electrons are unable to access this region as they are tied to magnetic field lines, electrons that would reach this region are reflected by the negative potential of the Debye sheath. This region can be distinguished when plotting the particle density in front of the wall as shown in figure 4.7.

As the walls are allowed to establish a floating potential, there are equal fluxes of ions and electrons at all points along the length of the wall apart from at the very edge of the right hand side of the probe, as ions are the only species capable of hitting this region of the wall. A positive potential therefore develops at this point to attract electrons and repel ions. The potential structure along the wall is shown in figure 4.8.

In order to measure the value of the coefficients c_1 and c_2 in equation 4.12 a value of a is required for multiple field inclination angles, keeping the other plasma parameters constant. The value of a can be extracted from the ion current collected by the probe at different bias voltages. From equation 4.10, taking the ion current component

$$I_{ion} = I_0 + I_0 a |V|^{3/4} \tag{4.13}$$

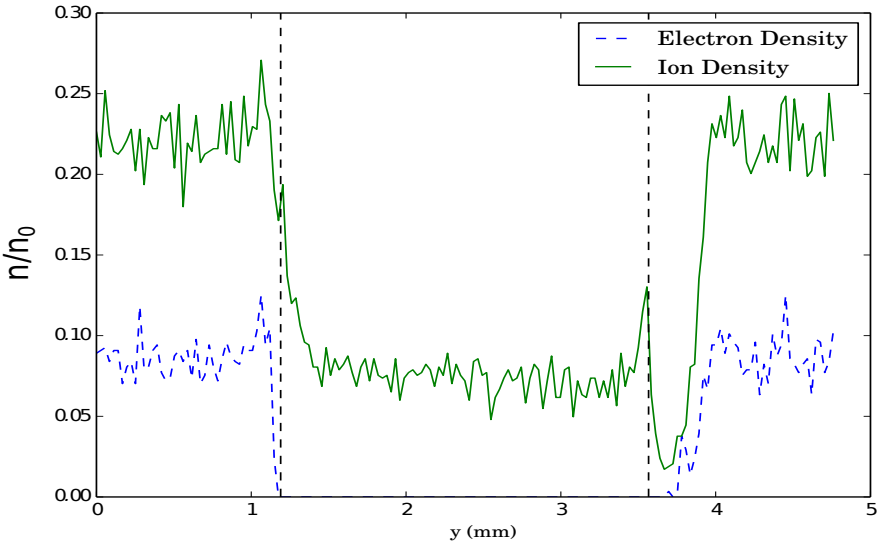

FIGURE 4.7: The ion density (green, solid) and electron density (blue, dashed) in front of the wall. The densities are normalised by the density at the entrance to the MPS. The edges of the probe are shown in dashed, vertical lines.

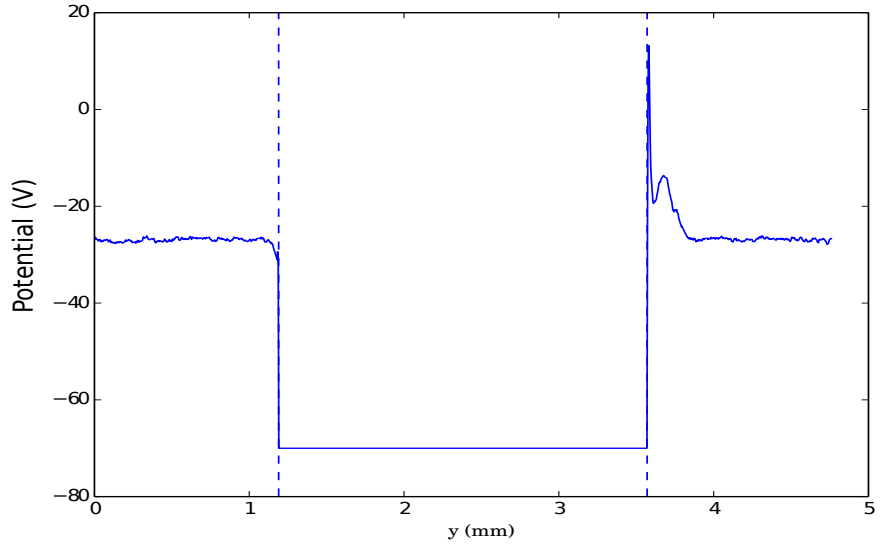

FIGURE 4.8: The potential profile along the wall.

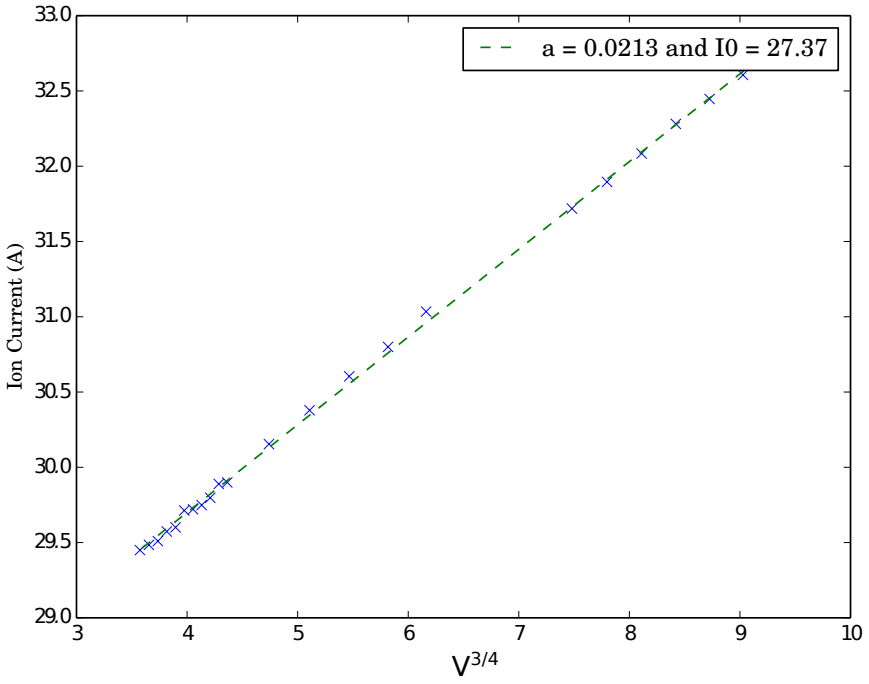

FIGURE 4.9: The ion current collected by the probe at different bias voltages.

Plotting the ion current against $|V|^{3/4}$ then gives a straight line, with the y-intercept equal to I_0 and the gradient equal to $I_0 a$ as shown in figure 4.9.

To validate the VSim PIC simulations, this procedure was carried out for three different angles of inclination. From equation 4.10, it can be seen that a plot of $aL(\sin\theta)^{1/2}$ against $\cot\theta$ results in a straight line graph with c_1 equal to the y-intercept and c_2 equal to the gradient. Figure 4.10 shows the VSim results agree well with those of [74], obtaining a value of $c_1 = 0.5$ and $c_2 = 0.6$

In summary, the transition from the MPS to the DS can clearly be seen in the simulation results. As with [73]: an enhanced sheath thickness in front of the probe, relative to the floating wall is observed; the thicker sheath leads to an ion focusing effect at the leading edge of the probe; whilst electrons, that are tied to magnetic field lines, cannot access a region behind the probe. The floating condition used in VSim ensures equal fluxes of both species to the wall and results in a potential structure behind the trailing edge of the probe that is not observed in [73]. This does not appear to affect the charged particle collection by the probe as good agreement with the model presented in [74] has been found.

4.5 Incorporating the Gaps

After successful comparison with [74], simulations were carried out including a gap between the probe and the wall, using the simulation domain shown in figure 4.4. The effect of the presence of a probe-wall gap becomes evident when plotting the current

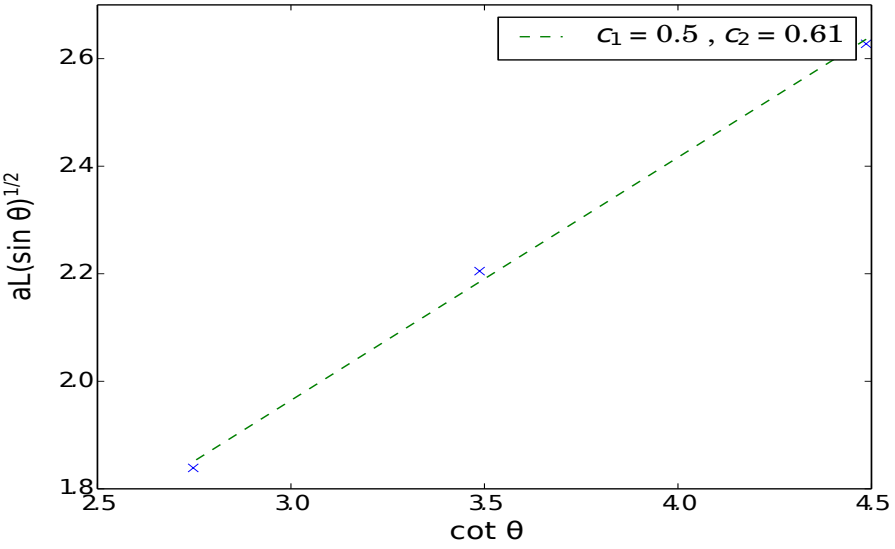

FIGURE 4.10: The product of parameter a extracted from the I-V characteristic multiplied by $\sqrt{\sin\theta}$ and the length of the probe (in units of λ_D) against $\cot\theta$.

reaching each part of the wall, as shown in figure 4.11. Both the leading edge of the probe and the face of the wall behind the trailing edge of the probe, upon which magnetic field lines end, see a large ion current. In the case of the probe, the increase in the ion current is much larger than that caused by the ion focusing effect. The effective collection area of the probe is increased as magnetic field lines terminate on the side of the probe. This is also the case for the face of the wall behind the trailing edge of the probe. The increased ion current here is matched by a higher electron current.

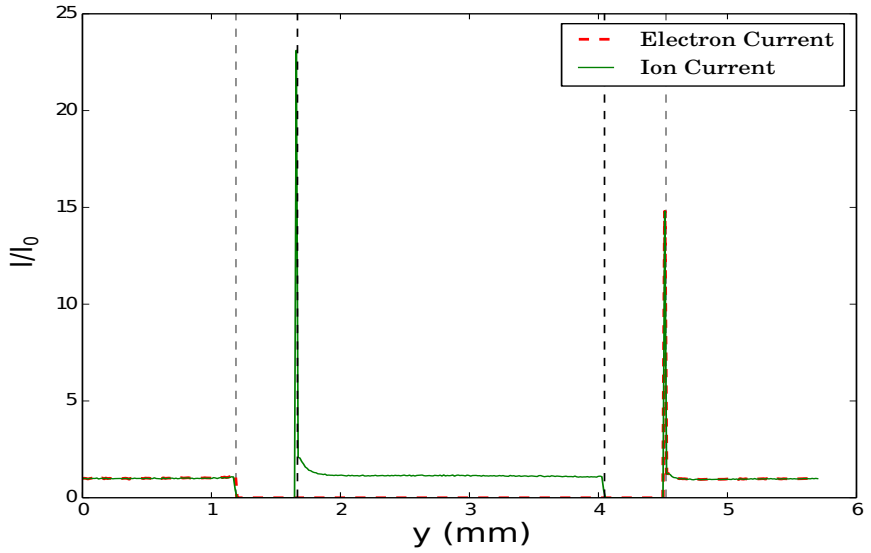

FIGURE 4.11: The ion current (green, solid) and electron current (red, dashed) reaching the wall. The currents are normalised by I_0. The edges of the probe (wall) are shown in black (grey), dashed, vertical lines.

The peak in ion current at the wall is lower than at the probe for two reasons. Firstly, the floating wall doesn't experience an ion focusing effect and secondly, as with the no-gap simulations, the particle density is reduced in a region behind the trailing edge of the probe. The particle density in front of the wall for the gap model is shown in figure 4.12.

The densities in front of the wall and probe show the same trends as for the no-gap model. The ion density in front of the wall is higher than in front of the probe as this region is deeper into the probe's DS. The particle densities are much higher in front of the gaps where there is no surface for a build up of charge to develop and therefore no sheath forms. The lateral expansion of the probe's DS can be seen in a plot of the electrostatic potential in front of the wall as shown in figure 4.13.

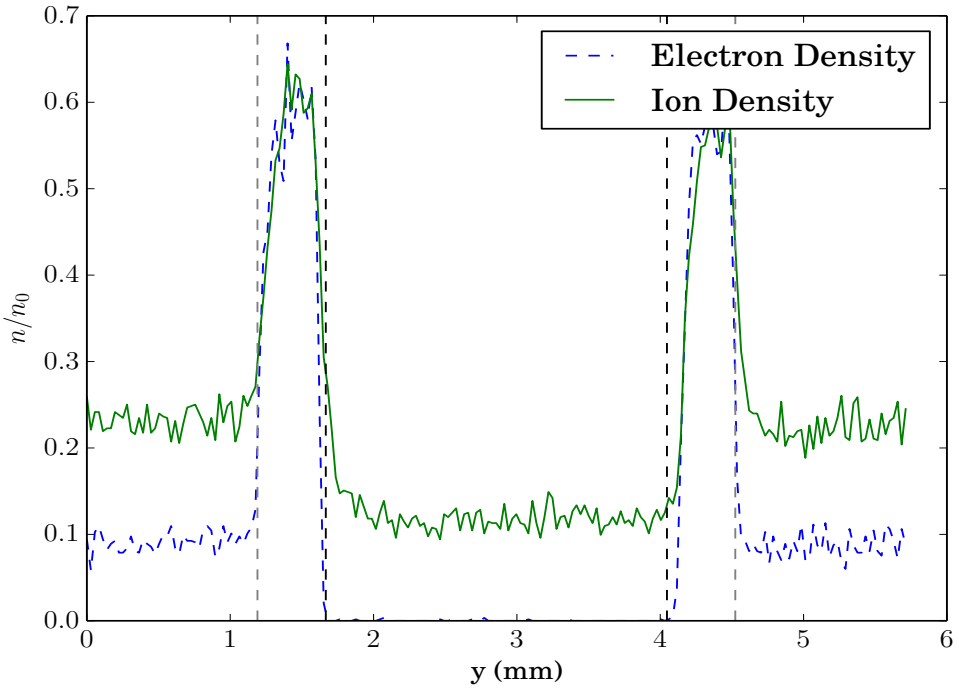

FIGURE 4.12: The ion density (green, solid) and electron density (blue, dashed) in front of the wall. The densities are normalised by the density at the entrance to the MPS. The edges of the probe (wall) are shown in black (grey), dashed, vertical lines.

The presence of the gap exposes the side of the probe directly to plasma travelling along impinging field lines, increasing the effective collection length of the probe. The extent of this effect must be calculated in order to extract the correct plasma density from FMP data on MAST.

4.6 Ion Collection and Estimation of the Electron Density

The model of [74], extended to include a gap of width, g, between the probe and the divertor surface is shown in figure 4.14. In front of the wall is a DS of thickness Δ_0. The

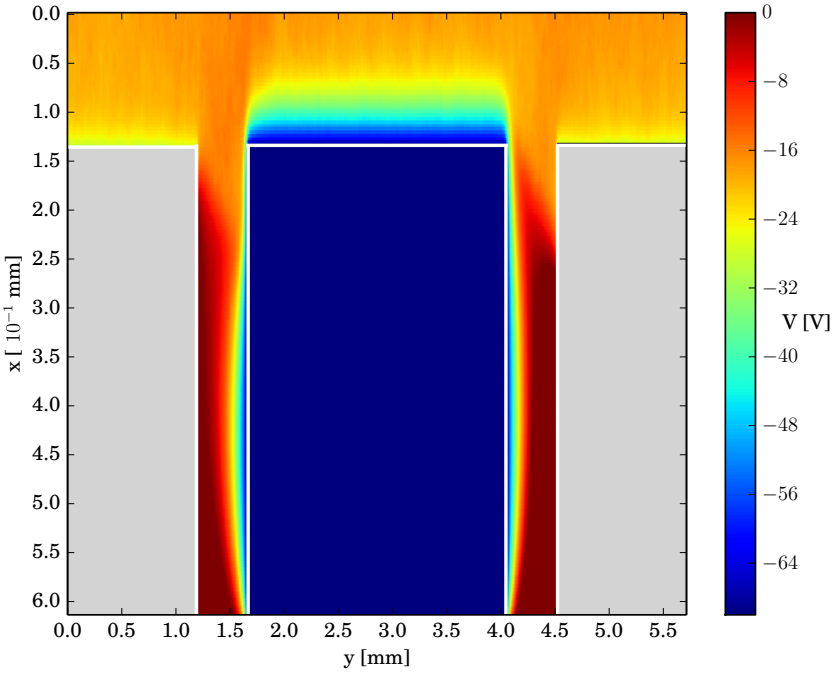

FIGURE 4.13: The potential structure in front of the wall in a VSim simulation incorporating the gaps. The probe is biased negatively with respect to the surrounding floating walls (shown in grey), therefore the probe's DS is thicker than that of the walls. The thickness of the sheath is exaggerated in this figure due to the difference in scaling of the x and y-axes.

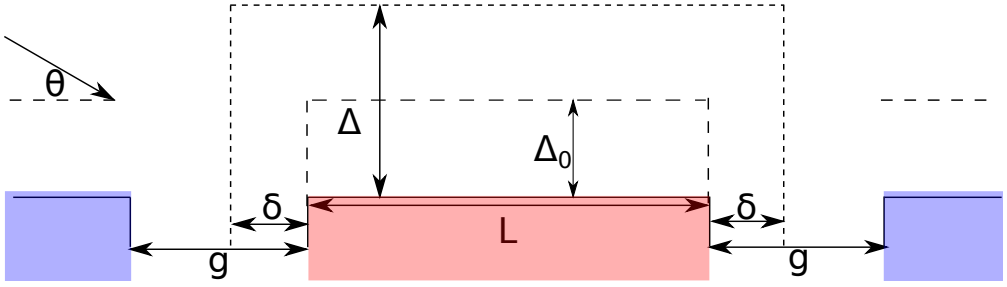

FIGURE 4.14: A model of the sheath in front of the FMP. The sheath is modelled as a rectangle. The floating wall has a sheath of thickness Δ_0. For $V_{probe} < V_F$ the probe has an enhanced sheath thickness of Δ and a lateral expansion of δ.

probe is biased more negatively than the floating wall and so has a DS thickness Δ. The sheath expands laterally either side of the probe by the length δ. Two simulations were carried out with identical plasma parameters and probe bias voltages, one simulation with the gap and one without. Figure 4.15 shows the effect of the gap on the collected ion current. The top line represents the current collected by the probe in the gap-model. From equation 4.10 it can be seen that I_0 is the magnitude of the ion current at the point $V = 0$, when the probe is at the floating potential. When $V = 0$, the DS thickness is the same in front of the probe as it is at the wall, the ion focusing effect therefore does not occur and the probe collects current over its projected length. The gap in between the

probe and the wall exposes the left hand side of the probe to the plasma as presented in figure 4.14. Magnetic field lines terminate on the side of the probe, therefore, the probe now subtends a larger flux tube. The length of the exposed side of the probe is given by $g \tan\theta$. Taking the projection of this length along the field results in $g \sin\theta$. As a result, the value of I_0 is increased by the factor $(L+g)/L$ from the no-gap case which would lead to an increase in the derived plasma density if not accounted for.

$$I_0 = enc_s(L+g)\sin\theta \tag{4.14}$$

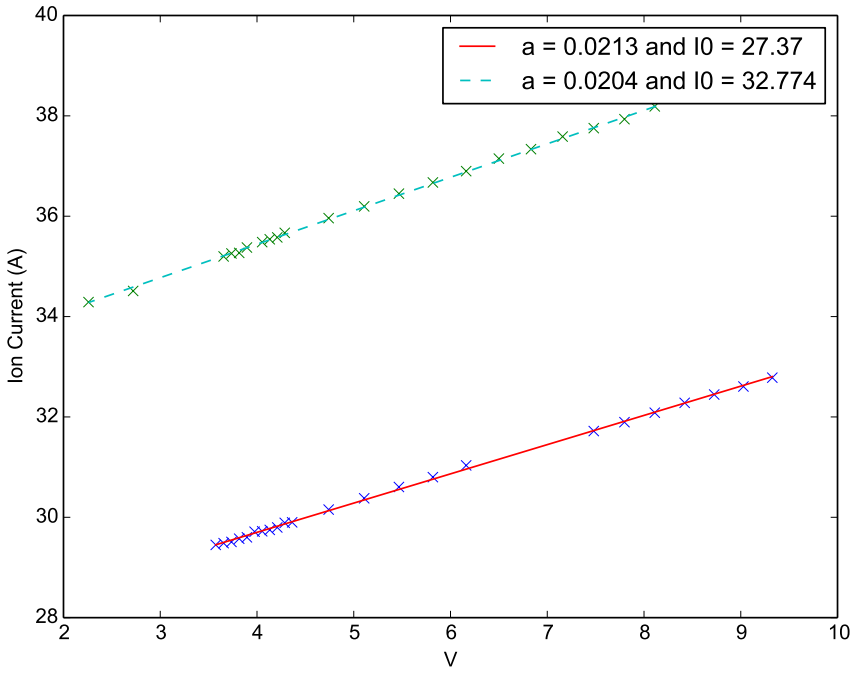

FIGURE 4.15: A plot of the ion current as a function of voltage applied to the probe. Top, dashed line represents the ion current in the gap model. Bottom, solid line is the current in the no-gap model.

For MAST FMPs, $L = 5$ mm and $g = 1$ mm. The presence of the gap therefore increases the collected ion current by 20% for the MAST probes. As can be seen in figure 4.15 the sheath expansion parameter is found to be lower for the probe in the gap-model. Following the derivation of [73], for the sheath expansion parameter, we have a new effective probe size

$$\begin{aligned} L_{eff} &= [L+2\delta]\sin\theta + (\Delta - \Delta_0)\cos\theta + g\tan\theta\cos\theta \\ &= [L+2\delta+g]\sin\theta + (\Delta-\Delta_0)\cos\theta \end{aligned} \tag{4.15}$$

The normalised current to the probe is then

$$I_i/I_0 = \frac{L_{eff}}{(L+g)\sin\theta} = 1 + \frac{2\delta}{L+g} + \frac{(\Delta-\Delta_0)\cot\theta}{L+g} \tag{4.16}$$

From equations 4.10 and 4.16 we have a new expression for the sheath expansion parameter

$$a = \frac{2\delta + (\Delta - \Delta_0)\cot\theta}{(L+g)} V^{-3/4} \tag{4.17}$$

The size of the sheath surrounding the probe is proportional to the applied voltage and the local Debye length in front of the probe. This is larger than the Debye length far away from the probe due to the density drop in the MPS. Hence

$$\delta, \Delta \propto \frac{V^{3/4}}{\sqrt{\sin\theta}} \tag{4.18}$$

Substituting these expressions into equation 4.17 gives

$$a = \frac{c_1 + c_2 \cot\theta}{\sqrt{\sin\theta}} \frac{\lambda_D}{L+g} \tag{4.19}$$

We expect to see a reduced sheath expansion parameter due to the presence of the gap, however, the predicted reduction from equation 4.19 is more severe than the measured reduction. Figure 4.16 shows the dependence of the sheath expansion parameter on θ. Various probe lengths were simulated, for a range of θ typical to conditions on MAST. Each data point requires an I-V curve to be simulated in order to obtain a value for the sheath expansion parameter. Measuring the value of the sheath expansion parameter, for a range of probe lengths and field angles allows a measurement of c_1 and c_2 to be made. c_2 is the gradient of the line. As with [74], we find c_2 depends on the ratio of the probe length to the Debye length, tending to 0.6 for larger probes. The y-intercept represents c_1, we find $c_1 \approx 0.9$ which is an increase over the previously reported value of 0.5. The inclusion of the probe-wall gap allows the probe sheath to expand laterally into a region of lower density than the bulk plasma. As a result of an increase in c_1, the reduction in the sheath expansion parameter for the gap model is not as severe as predicted. Taking into account the larger value for c_1 we find the sheath expansion parameter for probes in the gap-model is well described by equation 4.19.

4.7 Electron Collection and Electron Temperature Estimation

In hot magnetised plasmas it is often assumed that the relation $I_e = I_0 e^{-V}$ holds provided the electrons have a Maxwellian velocity distribution, where V is given by equation 4.7. A restricted region of the IV curve, below the floating potential, is used to avoid problems of spuriously high T_e measurements [37, 38, 75, 76]. Once the ion current has been deducted from the total current it is then trivial to determine the electron temperature by plotting $\log I_e$ against V_{probe} and measuring the gradient. Following the experimental procedure for the electron current to the probe in our simulations, it was observed that the probe measured T_e values that were higher than the specified source temperature. This occurred, in both simulations with and without the probe-wall gap,

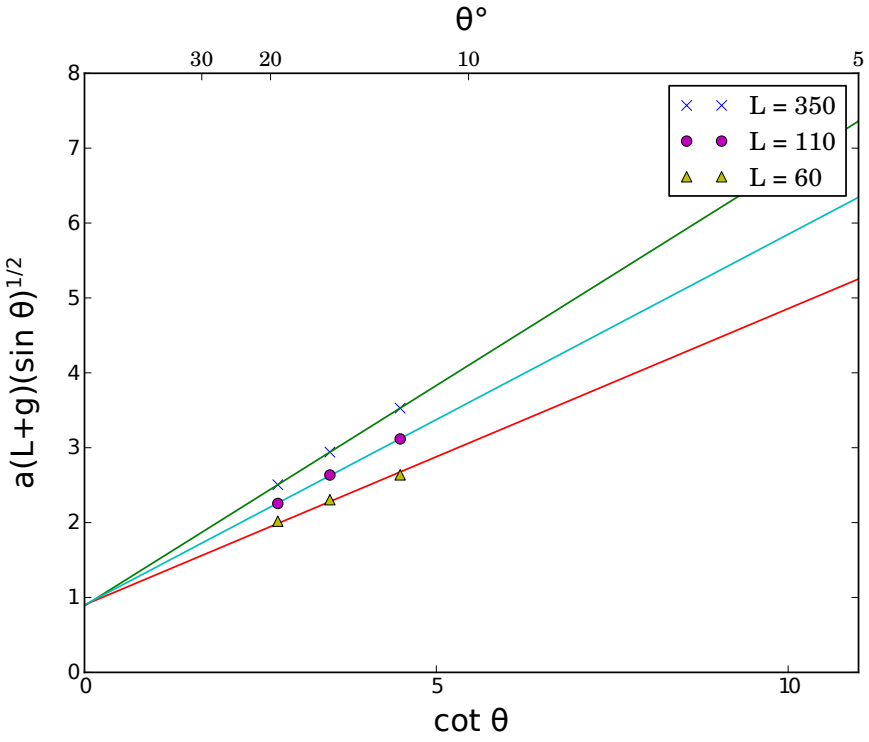

FIGURE 4.16: The product of the sheath expansion parameter a obtained from the I-V characteristic multiplied by the probe length L and the gap length g (both in units of λ_D) and $\sqrt{\sin\theta}$ as a function of $\cot\theta$.

provided $\theta \neq 90°$. In simulations the electron current and ion current are known individually, therefore problems with non-saturation of the ion current will not influence the electron current measured in our simulations. The presence of the gap is not expected to vary the extent of this effect. The following results are presented for the simulations with the no-gap model, these were used to investigate this effect as the simulation domain consists of fewer grid cells and so the simulations are faster to run. Examining the velocity distribution for electrons that are absorbed by the probe, reveals a significant portion of the electron current to the probe is made up of electrons that have a negative parallel velocity, i.e. directed away from the probe. This is shown in figure 4.17. These are electrons that have been reflected in the sheath and begin to move away from the probe, yet still reach the surface. Tracking these electrons as they propagate through the sheath, towards the probe, reveals their collection mechanism. The electrons are able to travel to within an electron gyroradius of the probe before undergoing reflection. At this point their orbit is sufficient to bring them to the probe, despite not having enough parallel energy to overcome the negative probe potential. The trajectory of an electron that makes it to the probe despite having a negative parallel velocity is shown in figure 4.18. The electron current to the probe then consists of electrons that have sufficient parallel energy to reach the probe and electrons that should not reach the probe but have enough energy to reach within 1 ρ_e of the probe. The proportion of the current to the probe made up of these latter electrons increases with increasing negative bias

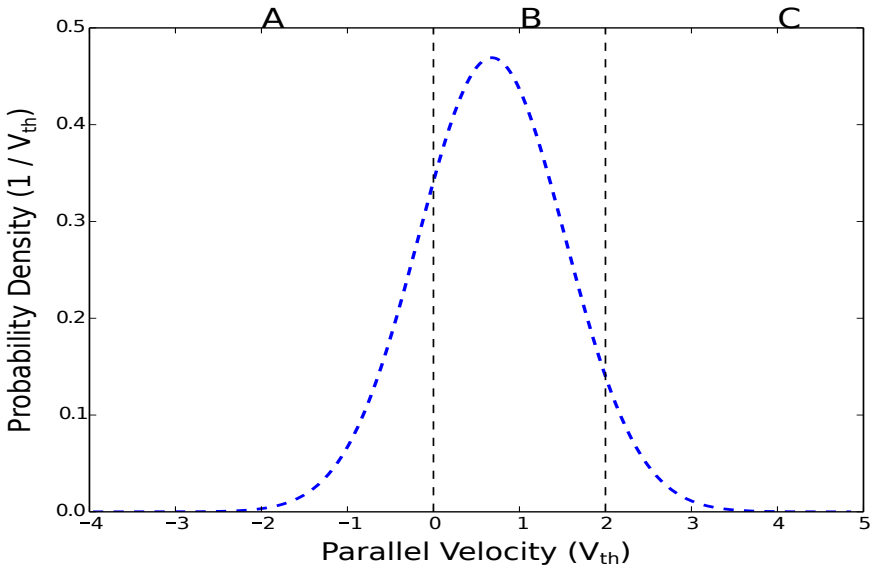

FIGURE 4.17: The parallel velocity distribution of electrons that are absorbed by a probe biased −28 V relative to the floating potential. Positive velocities are directed towards the probe. Region A represents electrons that have insufficient parallel energy to reach the probe but are assisted by their gyromotion. Region B is composed of a mixture of electrons that do have sufficient parallel energy to reach the probe and those that reached the probe due to their gyromotion before having time to reflect in the sheath. Region C consists of electrons that would make it to the probe regardless of finite orbit effects. The line between regions B and C is for illustrative purposes only. This boundary is not clearly defined.

to the probe. The result of this is that the electron current falls off more slowly than anticipated. Applying the standard theory then results in an overestimation of T_e. For a density of $6.4 \times 10^{18}\, m^{-3}$, at an angle of 12° and particles injected with a velocity distribution consistent with a 6 eV plasma, the temperature measured by the probe was 6.6 eV, a 10% increase. The influence of plasma density, field angle and strength and electron temperature on this effect is described below. With the unique capabilities provided by PIC simulations, it is possible to extract the electron current consisting only of electrons that have a highly positive parallel energy. These are electrons that would make it to the probe regardless of finite gyroradius effects. By only taking the current consisting of electrons that reach the probe with $V_{\|} \geq 2\ V_{th}$ for each probe bias, represented by region C in figure 4.17, it is possible to apply standard probe theory to measure the electron temperature of the particles injected in the source region. The difference in T_e obtained when fitting a straight line to the log of the entire electron current compared to fitting just to the current consisting of the high energy electrons is shown in figure 4.19. This is confirmation that the source function is providing electrons at the specified temperature. Removing the portion of the current consisting of the negative $v_{\|}$ electrons, those in region A, reduces the error in the temperature measurement but does not measure the correct temperature of the particles injected into the simulation domain. This is because a portion of the electrons, in region B, with positive $v_{\|}$, will

have made it to the probe due to their gyromotion, before having time to reflect off the sheath. A method of excluding these electrons from the current is not apparent. Of course, in experiments, it is not possible to take a reduced portion of the electron current, the total current is all that is available to the experimentalist. A theory is required that takes into account electrons that reach the probe due to their gyromotion about the field. In order for an electron to be absorbed by the probe it must have sufficient parallel energy to reach within a distance of 1 ρ_e from the probe surface and be at the right phase of its orbit before undergoing a reflection. The magnitude of ρ_e should then be an important parameter, the smaller the radius, the further the electron has to travel through the sheath, thus reducing its parallel energy. The Debye length should also influence the extent of this effect, a smaller Debye length and sheath means the electron can get closer to the probe before experiencing the repulsive potential drop in the sheath. Therefore more electrons can get to within 1 ρ_e of the probe surface.

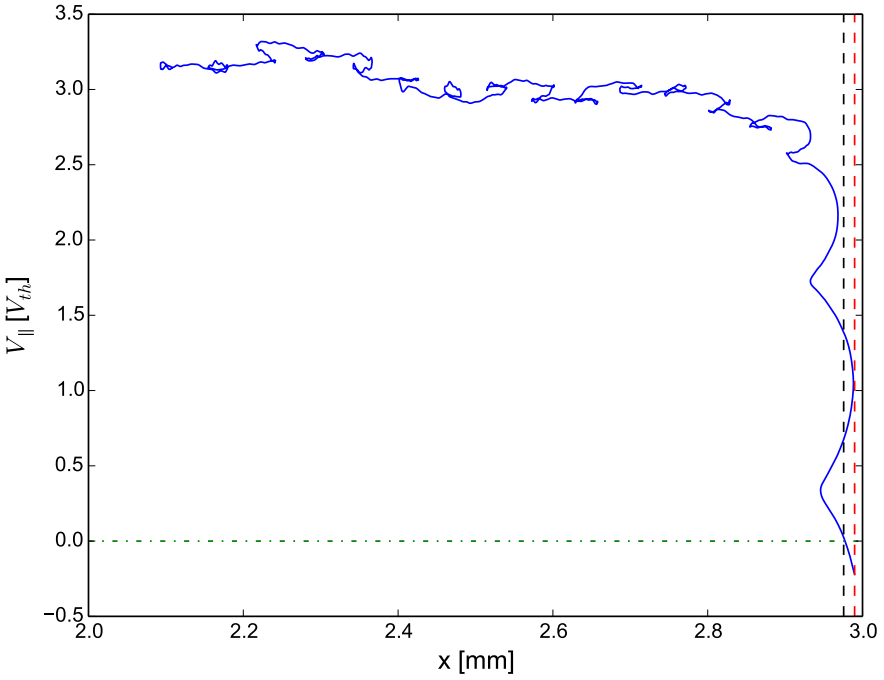

FIGURE 4.18: A plot of the parallel velocity of an electron that reaches the probe due to finite orbit effects as it moves through the bulk plasma, into the sheath, before reaching the probe surface. The two vertical dashed lines represent a region of width 1 ρ_e away from the probe. The electrons parallel velocity rapidly drops in the sheath, becoming negative within the marked region. At this point its orbital motion brings it to the probe.

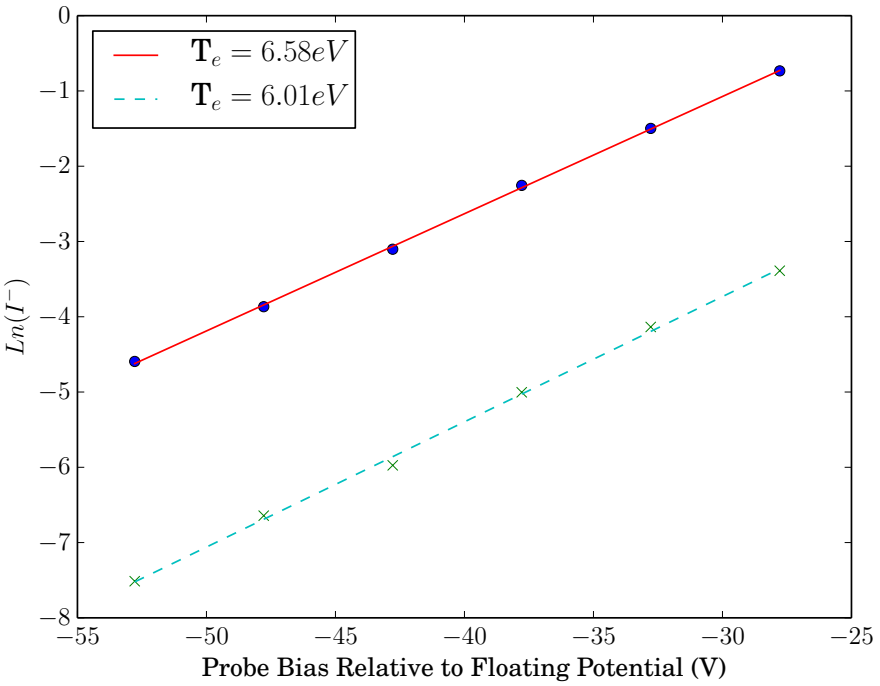

FIGURE 4.19: The electron temperature is derived from the gradient of the log of the electron current against the probe bias voltage. The solid, red line is obtained by taking the log of the entire electron current reaching the probe. This overestimates the electron temperature. The dashed, blue line is obtained by considering only the portion of the electron current that arrived at the probe with speed $\geq 2v_{th}$. This accurately measures the source temperature.

The collection of electrons with a negative parallel velocity was reproducible in 1D3V simulations, allowing for parameter scans to be carried out. These parameter scans varied the ratio λ_D/ρ_e to test its effect on the measured electron temperature. The ratio was adjusted by varying either the magnetic field strength or the plasma density. In addition to these simulations, a temperature scan was carried out and an angle scan. Presented in figure 4.20 are the results of the magnetic field and plasma density scans. Increasing the ratio λ_D/ρ_e, reduces the relative error in the temperature measurement. Also shown in dashed, vertical lines are the approximate values of λ_D/ρ_e based on typical divertor conditions for MAST [77], ITER [78] and CMOD [79].

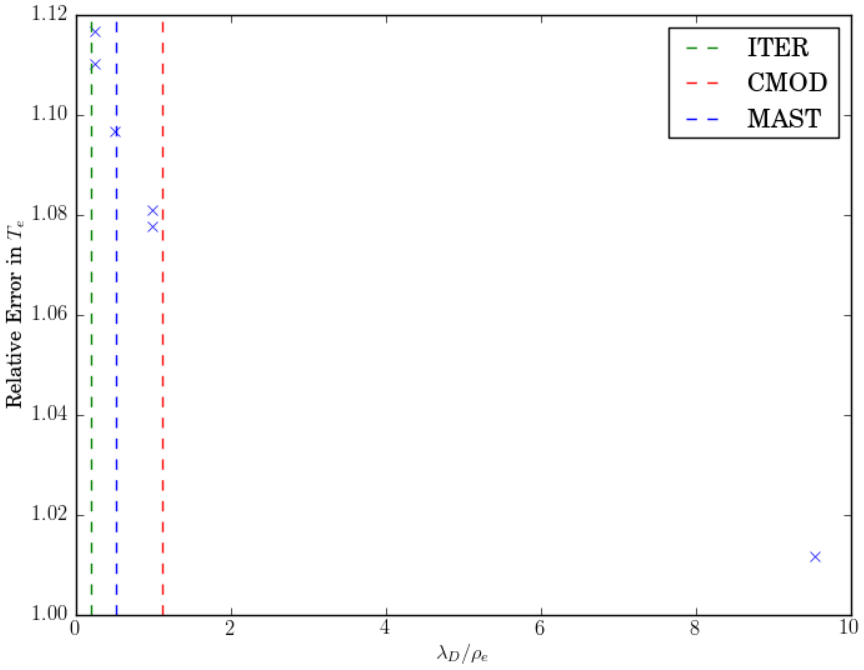

FIGURE 4.20: The relative error in the electron temperature measurement ($T_e^{measured}/T_e^{source}$) as a function of λ_D/ρ_e.

The effect also has an angle dependency. For cases where $\theta = 90$, the gyromotion of the electron has no component towards the probe and so this effect is not present. As the angle becomes more shallow, the relative error increases. The relative error in the temperature measurement as a function of angle is shown in figure 4.21. The relative error was fitted to a function $h(\cos\theta/\sqrt{\sin\theta}) + 1$, where h is a constant. The $\cos\theta$ term represents the component of the electrons gyroradius directed normal to the probe surface, while the $\sqrt{\sin\theta}$ term takes into account the increase in the local Debye length due to the MPS density drop. At a density of $6.4 \times 10^{18}\, m^{-3}$, a field strength of 0.4 T and a temperature for both species of 6 eV, it was found that $h = 0.055$. This value may change for different plasma parameters. This result provides further evidence that the ratio ρ_e/λ_D plays a key role in the error of the temperature measurement.

Simulations were carried out varying the electron temperature whilst keeping the magnetic field strength and plasma density constant. For the case described above, with a density of $6.4 \times 10^{18}\, m^{-3}$ and a magnetic field strength of 0.4 T at an angle of 12°, the relative error in the temperature measurement was $\approx 10\%$ for a range of specified T_e from $6 \rightarrow 48$ eV. Both λ_D and ρ_e have a $\sqrt{T_e}$ dependency so the ratio of λ_D/ρ_e remains constant as T_e is varied.

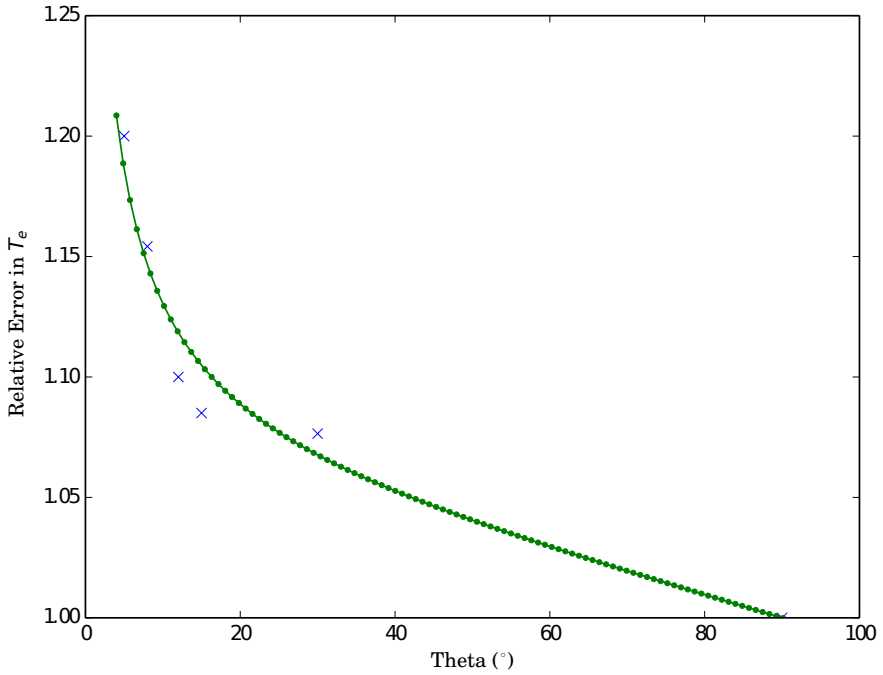

FIGURE 4.21: The relative error in the electron temperature measurement ($T_e^{measured}/T_e^{source}$) as a function of θ. The green line is a fitted function of the form $h(\cos\theta/\sqrt{\sin\theta})+1$. Where h is a constant.

In future machines, the high density and low angle of attack necessary for divertor tiles to survive the high heat loads, will place FMPs on these devices on the LHS of figures 4.20 and 4.21. Although this will somewhat be compensated by stronger magnetic fields, a complete theory to take into account the finite electron Larmor radius effect is necessary to reduce the error in T_e measurements. This theory is complicated as it depends on both ρ_e and λ_D both of which depend on T_e and the latter also depends on n_e. These are the two quantities the probe is used to measure.

4.8 Analysing Experimental Data

In this section both the no-gap model [74] and the gap model are fitted to experimental data obtained from a FMP on MAST and the results obtained are compared to the standard fitting procedure. The shot number was 30356. The data was analysed at time $t = 0.316$ s, with a toroidal field strength $B_t = 0.369$ T. The magnetic field made an angle $\theta = 8.46°$ with the probe surface. In the standard fitting procedure, first a straight line is fitted to the ion saturation region to give an estimate of I_{sat}^{+}. This method does not take into account sheath expansion effects. Once a value for I_{sat}^{+} has been obtained this value is fixed and the following function is then fitted to the I-V curve up to the floating potential

$$I = I_{sat}^{+}\left(1 - \exp\left(-\frac{V_{F,fit} - V_{probe}}{T_{e,fit}}\right)\right) \tag{4.20}$$

Here $V_{F,fit}$ and $T_{e,fit}$ are free parameters. The values obtained for the two variables are then used as initial guesses along with I^+_{sat} for fitting to the I-V curve with all three variables now free parameters. This returned the following values $I^+_{sat} = 0.0316$ A and $T_e = 9.97$ eV. The density is related to the saturation current by the following equation

$$n_e = \frac{I^+_{sat}}{c_s A_{probe} e \sin\theta} \tag{4.21}$$

In the standard fitting procedure it is assumed that the sound speed is given by

$$c_s = \sqrt{T_e e/m_i} \tag{4.22}$$

The fitted values then give a density $n_e = 4.34 \times 10^{18}\ m^{-3}$. However, from the FMP simulations, the sound speed is better described by $c_s = \sqrt{(T_e + \gamma_i T_i)/m_i}$ where $\gamma_i = 2$ for low angles of incidence [74]. Using this new value and assuming $T_e = T_i$ gives a lower density of $2.51 \times 10^{18}\ m^{-3}$. Now applying the no-gap model to the data. Firstly, a function is fitted to the ion saturation region, in this region it is assumed the electron current is zero, the current to the probe is then described by

$$I = I_0 \left(1 + a\left(\frac{V_F - V_{probe}}{T_e}\right)^{3/4}\right) \tag{4.23}$$

T_e and V_F are taken from the standard fitting procedure. This returns a value for I_0 and a. The latter two variables are then fixed and a fit to the I-V curve, up to the floating potential, is carried out to get a new estimate for T_e using the following function

$$I = I_0 \left(1 + a\left(\frac{V_F - V_{probe}}{T_{e,fit}}\right)^{3/4} - \exp\left(-\frac{V_F - V_{probe}}{T_{e,fit}}\right)\right) \tag{4.24}$$

As before, the values of I_0 and T_e are used to obtain an initial estimate for n_e. A full fit is then carried out using the obtained values as initial estimates. Both, I_0 and a, themselves depend on T_e and n_e. I_0 is proportional to the density and depends on temperature through the sound speed. a is proportional to the Debye length. The full fit equation is then given by

$$A n_{e,fit}\sqrt{T_{e,fit}} \left(1 + B\sqrt{\frac{T_{e,fit}}{n_{e,fit}}}\left(\frac{V_F - V_{probe}}{T_{e,fit}}\right)^{3/4} - \exp\left(-\frac{V_F - V_{probe}}{T_{e,fit}}\right)\right) \tag{4.25}$$

where A and B contain the constants of the fit.

$$A = \sqrt{3/m_i} q^{3/2} A_{probe} \sin\theta \tag{4.26}$$

$$B = \frac{0.5 + 0.6\cot\theta}{L \sin^{1/2}\theta}\sqrt{\frac{\epsilon_0}{q}} \tag{4.27}$$

The density and temperature estimated from the standard fit give rise to a Debye length such that $L/\lambda_D \approx 420$. It is then valid to take $c_2 = 0.6$. In lower density cases, c_2 would have to be treated as a free parameter. Applying this fit gives $n_e = 2.26 \times 10^{18}$ m^{-3} and $T_e = 9.21$ eV. So both quantities have decreased now that sheath expansion has been taken into account. To take into account the presence of the 1 mm gap, in between the wall and the probe, three adjustments must be made. Firstly, A_{probe} increases from $2mm \times 5mm$ to $(2mm \times 5mm) + (1mm \times 2mm)$ to take into account the exposed area of the side. L, in the B coefficient, is replaced by $(L + 1$ mm$)$ and finally, the value of c_1 is increased to 0.9. Applying this new fit to the data gives $n_e = 1.88 \times 10^{18}$ m^{-3} and $T_e = 9.22$ eV. The density is a 20% reduction on that as measured by the no-gap model whilst the electron temperature is the same. Densities on MAST are typically quoted with error bars of around 5%. The failure to take into account the gap is then a significant source of error. The fits to the data are shown in figure 4.22 and the derived values for n_e and T_e are given in table 4.2. The no-gap model and gap model provide an almost identical fit to the data, the interpretation of the fitted values is the distinguishing factor.

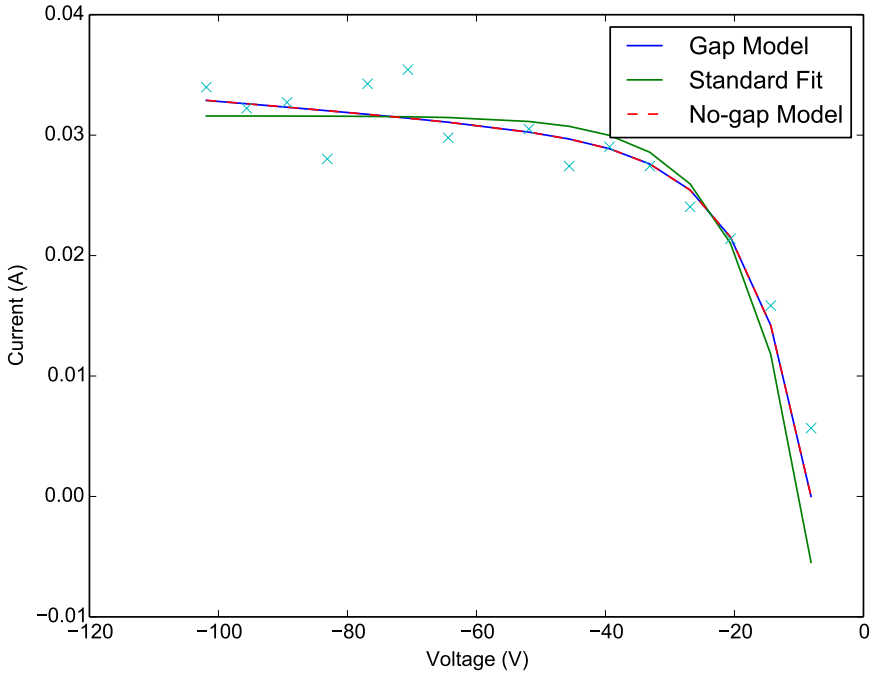

FIGURE 4.22: Fits to the MAST data for the three models.

Based on the density and temperature values derived from the gap model, the ratio of $\frac{\lambda_D}{\rho_e} = 0.8$. A very approximate overestimation of the temperature of 10% could be expected.

	n_e (m^{-3})	T_e (eV)	χ^2_ν
Standard Fit	$2.51 \times 10^{18} \pm 1.6 \times 10^{17}$	9.97 ± 1.5	6.1
No Gap model	$2.26 \times 10^{18} \pm 1.5 \times 10^{17}$	9.21 ± 1.3	1.6
Gap Model	$1.88 \times 10^{18} \pm 1.2 \times 10^{17}$	9.22 ± 1.3	1.6

TABLE 4.2: Electron density and temperature values extracted from the MAST data for each model along with a reduced chi-squared value (χ^2_ν) to estimate the goodness of the fit for each model.

4.9 Discussion

The simulations of [74] have been reproduced in VSim. This benchmark shows that VSim is able to reproduce previously reported findings, calculated using a different code and gives confidence that VSim can accurately simulate flush mounted probes in a tokamak environment. The model has been extended to incorporate a gap in between the probe and the floating divertor tiles. This gap is present in all machines and is especially important for the FMPs on MAST as the gap size is significant compared to the length of the probe. The presence of the gap was found to enhance the effective collection area of the probe and therefore needs to be included in probe data interpretation in order to extract the correct plasma density from the I-V characteristics. Non-saturation of the ion current was also observed in the gap simulations. The sheath expansion parameter, a, is slightly reduced from the no-gap model. The predominant effect on experimental data interpretation is the enhancement of the effective collection area of the probe. For MAST probes, the density is overestimated by 20% if the gap is not included.

Full resolution of the electrons gyromotion reveals a portion of the electron current to the probe consists of electrons with insufficient parallel energy to overcome the sheath potential drop. These electrons are able to reach within an electron Larmor radius of the probe and are then reflected away. At this distance from the probe surface, their motion around the magnetic field is able to bring them to the probe. This affects all regions of the I-V characteristic in which the probe is biased below the plasma potential. Applying standard probe theory to the electron current in simulations where the magnetic field makes a shallow angle to the probe surface, produces measurements of the electron temperature that are too high. If the correct electron temperature is to be extracted from probe I-V curves, a theory is required that takes into account this additional electron current to the probe. The use of strong magnetic fields will reduce the effects of sheath expansion and the finite electron gyro-orbit. For strong magnetic fields, the ions remain tied to magnetic field lines, even in the Debye sheath and so the probe collects current over its projected length ($(L + g)\sin\theta$). The Larmor radius of the electrons is reduced too so less electrons are capable of reaching the probe without having sufficient parallel energy to overcome the sheath potential.

It would be useful to extend this work to smaller magnetic field angles as future machines will aim to reduce θ to the minimum of engineering limits, to minimise the thermal load on the divertor components. In [74], the influence of E x B drifts on

particle collection by FMPs was investigated. The drifts caused an enhancement of the ion current to the probe but this effect was much smaller than the ion focusing effect. A reduction in the electron current was observed for a probe biased near the plasma potential. These effects indicate that three-dimensional PIC simulations of the FMPs would be beneficial to allow further investigation into the charged particle collection of these probes. Due to Debye lengths on the order of μm and probe lengths on the order of mm, three-dimensional PIC simulations are extremely computationally intensive.

Chapter 5

Ball-Pen Probe Simulations

Declaration

Figures 4, 6, 7, 9, 10 and the accompanying discussion have previously been published in the author's paper [80].

5.1 Introduction

The ball-pen probe is an advanced probe technique designed to directly measure the plasma potential (Ψ). As discussed in Chapter 2, a Langmuir probe inserted into a plasma floats not at the plasma potential, but at a floating potential (V_F) which is negative with respect to the plasma potential. This is due to the higher mobility of the electrons compared to the ions. The theory of Langmuir probes allows the value of the plasma potential to be determined from the current (I) - voltage (V) curve of a Langmuir probe. Assuming the probe operates in the thin sheath limit, a simple expression [81] relates the floating potential of the probe (V_{LP}) to the local plasma potential (Ψ)

$$V_{LP} = \Psi - T_e \ln(R) \tag{5.1}$$

where T_e is the electron temperature in eV and R the ratio of the electron saturation current (I^-_{sat}) divided by the ion saturation current (I^+_{sat}). The logarithm of R is often denoted as α such that

$$\alpha_{LP} = \ln(R) = \ln\left(\frac{I^-_{sat}}{I^+_{sat}}\right) \tag{5.2}$$

In principle it is possible to sweep the bias voltage applied to a Langmuir probe to derive V_{LP}, T_e and α_{LP}. The local plasma potential can then be obtained from equation 5.1. However, in practice, especially in fusion plasmas, it is not possible to measure R. As $I^-_{sat}/I^+_{sat} \approx \sqrt{m_i/m_e} \approx 40$ the probe can experience significant particle and heat fluxes whilst drawing I^-_{sat}. In these plasmas, probes operate in a restricted region of the I - V curve from floating to ion saturation. This allows measurements of n_e and T_e to

be made whilst avoiding damage to the probe and the problem of spuriously high T_e measurements [15, 36–38].

Measurements of the plasma potential (Ψ) and its fluctuations are vital for modelling transport phenomena in the edge region of tokamaks [82]. Turbulent structures (filaments) in the scrape-off layer are electrostatic and are advected towards the first-wall by E x B drifts arising from plasma potential fluctuations across the filament cross-section [83]. The strength and spatial scale of these potential fluctuations can be predicted, however, robust measurements of such fluctuations are lacking, making it difficult to fully validate models of radial transport in the SOL [84]. Various advanced probe techniques have been developed that aim to measure the plasma potential directly without requiring an electron temperature measurement. These include emissive probes [85] which will be discussed in Chapter 6 and the Ball-Pen Probe (BPP) [49] which is the focus of this chapter. The emissive probe is not well suited to fusion plasmas as it requires a thin filament of wire to be exposed to the plasma, making it structurally weak, as opposed to the BPP which is a robust diagnostic capable of surviving high heat loads [8]. Although this problem can be overcome with the use of laser heated emissive probes that do not require a thin filament of wire for operation and are therefore more robust [86]. The BPP was designed to reduce the ratio of saturation currents to unity so that the probe would float at the plasma potential, as evident from equation 5.1. With a typical filament size on the order of a cm and velocities on the order of km/s, microsecond time resolution is required to track the evolution of the potential between and during filament events [87]. The potential capability of the BPP to measure the plasma potential using a DC, floating measurement allows sufficient time resolution to measure these potential fluctuations [88]. Despite empirical confirmation of the BPPs capabilities [49, 82, 89–91], the probe is lacking a model based on first principles to confirm the collection mechanism. Presented in this chapter, are the results of three dimensional PIC simulations to explore the behaviour of the BPP.

This chapter begins by describing the principles behind the design of the BPP. An overview of the empirical evidence for the workings of the BPP is then given. The PIC simulation model is then described and results obtained from it are discussed in the remainder of the chapter. Simulations are used to investigate the collection mechanism of the BPP as well as the capability of the BPP to measure the plasma potential and the electron temperature. The chapter finishes with future work and concluding remarks.

5.2 The Ball-Pen Probe Design and Theory

There are currently two designs for the BPP. The initial design [49] consisted of a conically shaped collector shielded by a tube of insulating boron nitride. This design is shown in figure 5.1. The latter design is equipped with a flat, rather than conical collector and will be discussed later in this section.

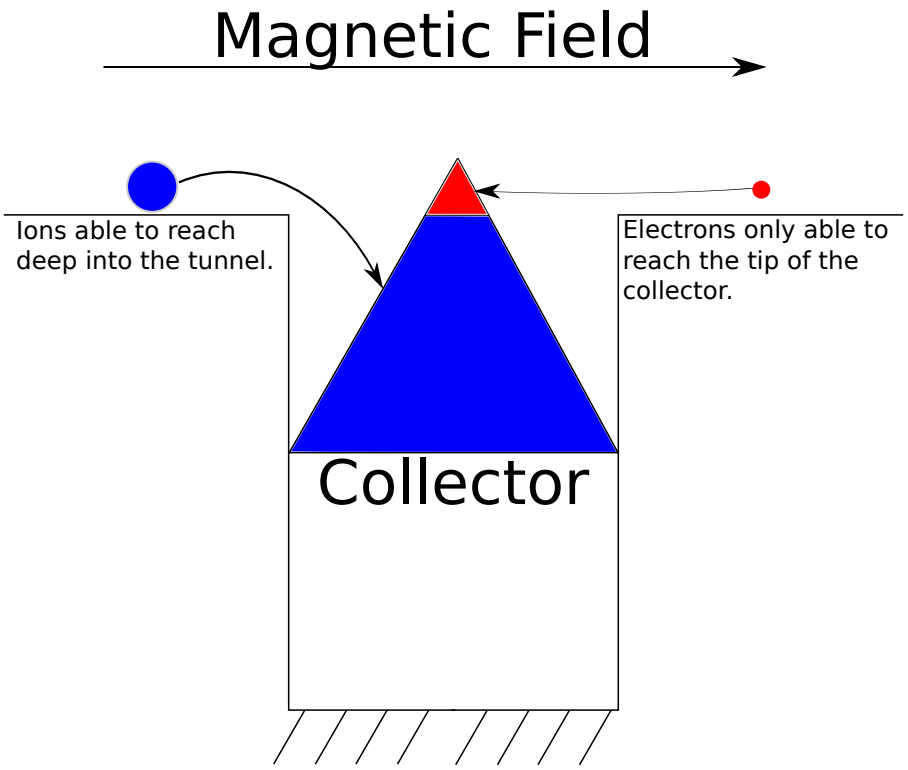

FIGURE 5.1: A schematic of the initial design of the BPP proposed by Adamek [49]. The probe is orientated such that the axis of the tunnel is perpendicular to the magnetic field.

The probe is aligned such that the axis of the tunnel is near perpendicular to the magnetic field. The vertical position of the collector can be adjusted to alter the collection area that is exposed to the plasma. By recessing the collector inside the tunnel, the BPP aims to exploit the difference between the ion Larmor radius (ρ_i) and the electron Larmor radius (ρ_e) to achieve a value of $R = 1$. As shown in figure 5.1, electrons with their small gyro-orbits will only be able to access the small tip of the collector, with area (A_e), whereas the larger ion gyro-orbit allows them to enter deep into the tunnel and access a much larger collection area (A_i). Due to their low mass, the electrons have a much higher parallel current density (J_e) relative to that of the ions (J_i) and so a larger ion collection area is required to equalise the saturation currents to the collector. In order for the ion saturation current to equal the electron saturation current, the following criteria must be met

$$I_e = A_e J_E \quad = \quad I_i = A_i J_i \tag{5.3}$$

As $J_e > J_i$ it is only possible to achieve a value of $R = 1$ if $A_e < A_i$. By adjusting the effective collection areas of the probe for the different species it was envisaged that an optimum recession depth would be found for which $R = 1$ [49]. In the ideal case, it was thought that recessing the probe further than this depth would result in a larger ion saturation current than electron saturation current, leading to a value of $R < 1$ and a floating potential that was positive with respect to the plasma potential. Likewise, raising the probe above this optimum depth would lead to values of $R > 1$ as seen for a

typical probe, in which case the probe collector would float negatively with respect to the plasma potential.

This simple model, first proposed by Adamek [49], shows some qualitative agreement with experimental data, but there are empirical features which can not be explained by this model, suggesting there is more complex physics to be considered. These empirical features will be discussed below. In addition, in [92], an alternative BPP design with a flat, cylindrical collector was implemented and results compared favourably with the initial BPP conical design, demonstrating that the conical collector is not essential to the BPP collection mechanism.

It is possible to use a BPP in conjunction with a standard Langmuir probe to make fast measurements of the electron temperature. This has been carried out on multiple tokamak experiments and yielded excellent agreement with Thomson scattering data [90, 93, 94]. The floating potential as measured by a BPP and a Langmuir probe (LP) can be written as

$$V_{BPP} = \Psi - \alpha_{BPP} T_e \tag{5.4}$$

$$V_{LP} = \Psi - \alpha_{LP} T_e \tag{5.5}$$

By rearranging these expressions we obtain

$$T_e = \frac{V_{BPP} - V_{LP}}{\alpha_{LP} - \alpha_{BPP}} \tag{5.6}$$

It is not possible to measure α_{LP} in most tokamak experiments as the probe drains too high a current in electron collection mode, however a theoretical value, for a planar Langmuir probe, is given by Stangeby [25]

$$\alpha = -\frac{1}{2} \ln \left(2\pi \frac{m_e}{m_i} \left(1 + \frac{T_i}{T_e} \right) \right) \tag{5.7}$$

Which gives for a hydrogen plasma, assuming $T_i = T_e$, $\alpha_{LP} \approx 2.5$. α_{BPP} on the other hand can be measured directly in experiments as the currents to the collector are much lower. It is possible to use these two values along with a Langmuir probe and a BPP operated in floating mode to determine T_e. All that is needed is a floating potential measurement from each probe, which can be made instantaneously, only limited by the speed of the data acquisition system. In fusion plasmas, T_e is typically measured by sweeping a standard Langmuir probe from ion collection to floating potential and then fitting an exponential to the I-V curve. This method is slow relative to the BPP-LP method due to the time it takes to sweep the probe voltage. The BPP-LP method then offers better time resolution and potentially more accurate measurements of T_e as it uses a floating potential measurement from the Langmuir probe which is considered to be in the safe region of the I-V curve for a probe in magnetised plasma [37].

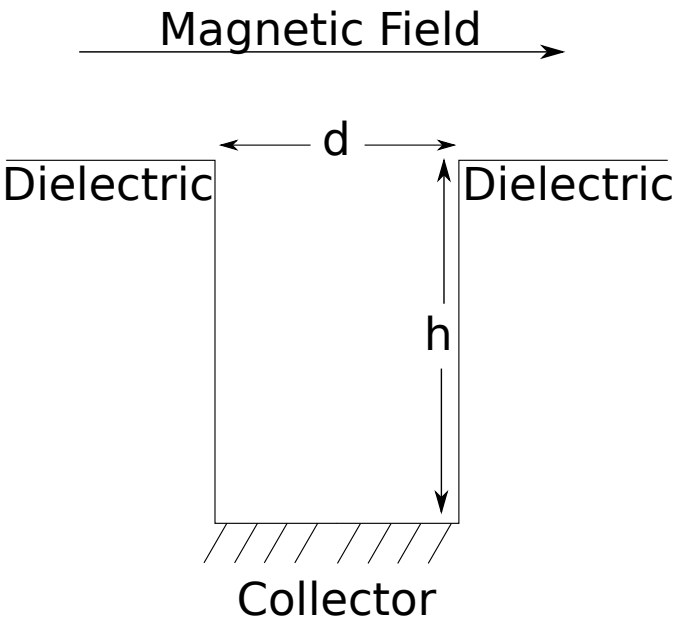

FIGURE 5.2: A BPP with a flat cylindrical collector. Also referred to as a Katsumata-type probe. d is the diameter of the probe and h the retraction depth.

5.3 Empirical Confirmation of the Ball-pen Probe Method

BPPs have been used to measure the plasma potential in multiple tokamak experiments including CASTOR [49], COMPASS [89], MAST [90] and ASDEX Upgrade in both L-mode [95, 96] and H-mode [82, 95]. Comparative measurements of the plasma potential were made using a BPP and a self-emitting Langmuir probe on COMPASS [97] and with a BPP and emissive probe on CASTOR [98]. BPPs have also been employed in low-temperature, weakly magnetised plasmas [91, 99]. In these plasmas the electrons are strongly magnetised but the ions are demagnetised. It was found that the BPP could measure the plasma potential in this case, but the capability of the BPP to shield the electron current was strongly dependent on the probe geometry, only effectively screening the electrons once the radius of the insulating tube was less than the electron Larmor radius [99]. This is discussed in more detail in Chapter 6.

Figure 5.3 shows the orginal BPP designed by Adamek alongside experimental results obtained by the probe, taken from [49]. In Adamek's initial experiments, an I-V curve was produced by sweeping the bias voltage applied to the conical collector, this enabled a value of R to be obtained. As can be seen in figure 5.3 c, the probe behaves as a standard Langmuir probe, with an electron saturation current much greater than the ion saturation current, for positive values of h, where the collector is outside the tunnel and directly exposed to plasma. A large reduction is observed in the electron saturation current, for negative values of h, where the collector is recessed inside the probe tunnel, demonstrating the capability of the probe to shield off the electron current. The ion saturation current remains roughly constant for both I-V curves, which results in a large reduction of R for the recessed collector relative to the exposed collector. The

process of sweeping the probe was repeated for various retraction depths, providing a measurement of the floating potential and α_{BPP} as as function of collector depth. This is shown in figure 5.3 d. As the collector is recessed inside the insulating tube, α_{BPP} approaches zero, although it is never observed to actually reach zero. At a recession depth of $h = -0.5$ mm, corresponding to a recession depth of one ion Larmor radius, α_{BPP} was observed to reach a minimum of ≈ 0.2 . At this point, if equation 5.1 is valid for the BPP, the collector floats at a potential which should be very close to the plasma potential.

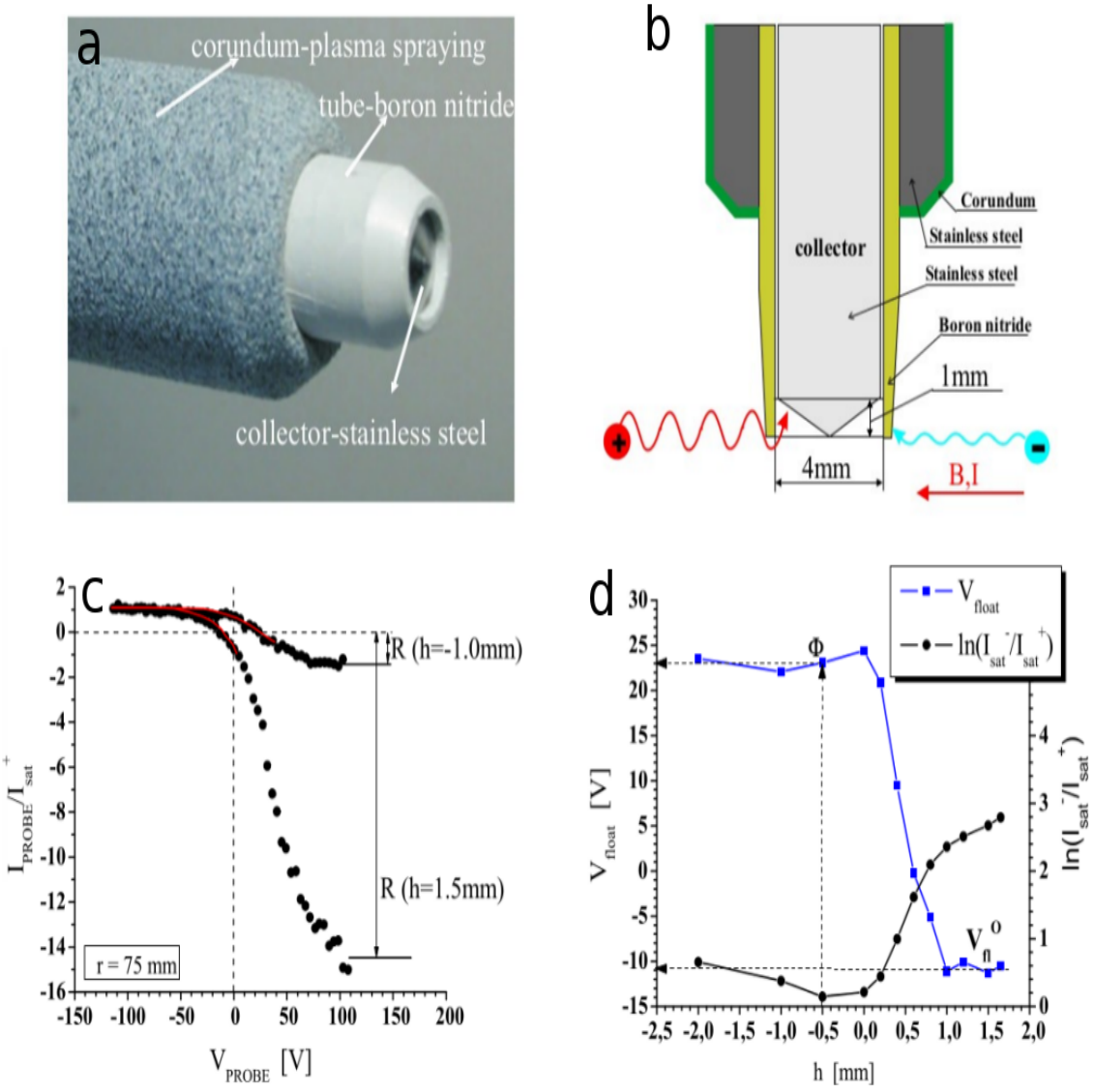

FIGURE 5.3: Top: The orginal BPP designs by Adamek. Bottom: Measurements made by the BPP on the CASTOR tokamak. Figure c shows two I-V traces for the probe collector at different recession depths. Figure d displays the floating potential and the measured value of α_{BPP} for the collector as a function of recession depth. Images taken from [49].

Clearly there is strong empirical evidence for the success of the BPP technique, however, there are discrepancies between the experimental observations and the ideal

theory. Firstly, α_{BPP} tends to zero but does not reach it, meaning there is always a higher electron saturation current to the probe than ion saturation current, even when the collector is recessed beyond multiple ρ_i. Ideal theory predicts negative values for α with sufficient probe recession as $I_e \rightarrow 0$ but this is not observed in experiments. These observations imply that the simple model, based on geometrical shadowing, is incomplete and significant transport perpendicular to the magnetic field must occur for electrons to still reach the collector surface once it is recessed beyond ρ_e. Experiments with a flat BPP collector [92], observed both ion and electron currents to the collector even when it was recessed beyond the ion Larmor radius, providing further evidence that cross-field transport must play a role in particle collection for the BPP. As such, a model for particle transport to the collector is required to verify the experimental results.

2D PIC simulations of the BPP have been carried out by Komm [100]. In these simulations, the extent of the probe tunnel along the field was simulated as was the depth of the probe tunnel down to the collector. The direction perpendicular to the magnetic field was neglected for ease of computation. This meant that the tunnel essentially had infinite width in this direction. These simulations verified the suitability of equation 5.1 for the BPP. However, values of $\alpha_{BPP} < 0$ were reported which have not been observed experimentally. This is in agreement with observations made from early 2D simulations carried out in VSim. It was found that when the direction perpendicular to the field was ignored, electrons could not reach the collector if it was recessed too far, suggesting that electric fields in the perpendicular direction were key to electron transport. If instead, both perpendicular directions were simulated, whilst neglecting the parallel direction, both ions and electrons were observed to reach the probe. This model does not accurately represent reality, as the probe tunnel now has infinite width parallel to the field, giving ions and electrons unlimited time to travel down the tunnel, perpendicular to the field, without coming into contact with a tunnel wall. Only 3D PIC simulations can fully capture the physics of the BPP.

Detailed 3D PIC modelling of the ion sensitive probe (ISP) has been carried out by Komm [101]. The probe is of a similar design to the BPP but both the tunnel and collector are conducting and so can be biased to a potential independent of each other. It was found that a positive space charge region exists at the tunnel entrance as ions can penetrate deeper into the tunnel due to their large gyro-orbit. This leads to an electric field across the tunnel entrance and subsequently an E x B drift is established that drives electrons and ions downwards into the tunnel. The reported transport mechanism is supported by experimental work carried out by Sullivan [102], in which an ISP was designed with a circular collector split into two semi-circles. This allowed the current collected by each half of the collector to be analysed independently. During electron collection mode, where the collector was biased positively with respect to the tunnel walls, an asymmetry in the electron current collected by each half was observed. This asymmetry was consistent with the direction of the E x B motion expected, due to the electric field created by the collector and wall potentials. It is believed that a

similar mechanism is also responsible for transport of electrons into the BPP tunnel but 3D PIC simulations are required to confirm this. This chapter continues by detailing the 3D particle-in-cell simulations of the BPP, with a flat collector, carried out in order to explore the transport mechanism that allows electrons and ions to be collected. Simulations demonstrate the capability of perfect diagnostics within the constraints of Monte-Carlo noise. The plasma potential is known at each grid point and as the velocity of each particle is tracked, the electron temperature is also known. The simulations can therefore assess how well the BPP can reproduce input parameters of the simulation.

5.4 The Simulation Model

The simulation model is fully three dimensional (3D3V). The simulation domain captures a region of the probe head, the entire BPP tunnel down to the collector and a region of plasma above the probe at least four ion gyro-radii in depth in order to capture the magnetic presheath (MPS). The simulation domain is a cubic 3D Cartesian grid. The collector lies in the y-z plane at the bottom of the probe tunnel (where x is at a maximum value), as illustrated in figure 5.4. At the beginning of the simulation, the plasma region is filled with a quasi-neutral plasma, with velocities sampled from a Maxwellian distribution. Particles that hit the probe structure deposit their charge to that location and are then deleted from the system. Particles are injected along the top plane of the simulation at $x = 0$ to replenish those lost to the probe. The y and z axes are periodic and the magnetic field makes an angle θ with the y-axis. The plasma potential in the Larmor buffer region and at the top of the simulation is fixed to be 0 V.

The plasma density and temperature, modelled in the simulations, was restricted by computational demands. Typical simulated parameters are shown in table 5.1. These values are close to those found in the SOL of MAST [103], however, the simulated density is an order of magnitude lower than in experiments. Each grid cell in the PIC simulation had dimensions of half a Debye length to prevent non-physical plasma heating in the simulations [60]. Increasing the density reduces the required grid spacing and so more grid cells are needed to simulate the same spatial region. To determine the effect of density, a selection of comparison simulations were carried out with an increased density of $n = 1.0 \times 10^{18}$ m^{-3} which is more in line with MAST's conditions. The increased density had no significant effect on the simulation results and so lower density simulations were run to produce the following results.

Magnetic field strength B	0.54 T
Magnetic field inclination θ	10°
Plasma density n	$6.5 \times 10^{17}\,\mathrm{m}^{-3}$
Electron temperature T_e	60 eV
Ion temperature T_i	60 eV
Ion Larmor radius ρ_i	1 mm
Electron Mass m_e	9.11×10^{-31} kg
Ion Mass m_i	900 m_e
Ion Charge Z	1.6×10^{-19} C

TABLE 5.1: Typical plasma parameters used in the simulations of the BPP.

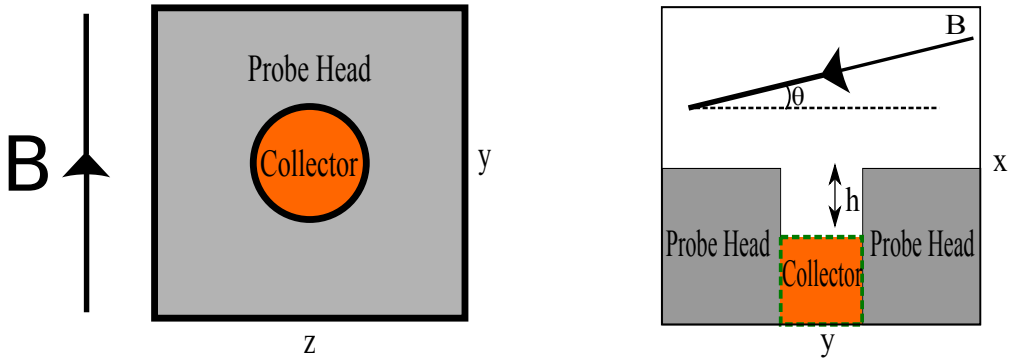

FIGURE 5.4: On the left - The BPP simulation domain as viewed from above looking along the x-axis. The collector sits at the bottom of the tunnel (maximum x). On the right - A cross-section of the domain. h is the recession depth. Grey surfaces are floating. The collector can either be biased to a potential or allowed to float.

In experiments, the BPP is aligned with respect to the magnetic field such that the axis of the probe tunnel is perpendicular to the field. In our simulations, an angle θ was introduced as this was necessary for the particle injection algorithm. In order to inject particles, a source function must be specified in which to sample the newly injected particles velocity from. The rate of injection for both species must be specified too. In this model, particles are injected at the top of the domain (minimum x, at the end of the buffer region) to represent particles streaming along field lines from the bulk plasma. In the case of perpendicular alignment ($\theta = 0°$), particle injection from the top of the domain would represent particles that have entered the domain due to cross-field transport mechanisms. A Maxwellian velocity distribution for these particles may be a valid assumption but the rate at which ions and electrons would enter the domain due to cross-field transport is not known. A crude attempt at particle injection for the case of a perpendicular field was made in which particles were re-injected into the top of the simulation domain, with a Maxwellian velocity distribution, at the rate at which they were lost to the absorbing surfaces in the simulation. In this set-up it was found that the top surface of the probe-head floated positively with respect to the plasma potential as the ions were the more mobile species due to their large Larmor orbit. As discussed in Chapter 2, this observation was expected as $\theta < \theta_c = \left(\frac{m_e}{m_i}\right)^{\frac{1}{2}}$ [31]. In an experiment,

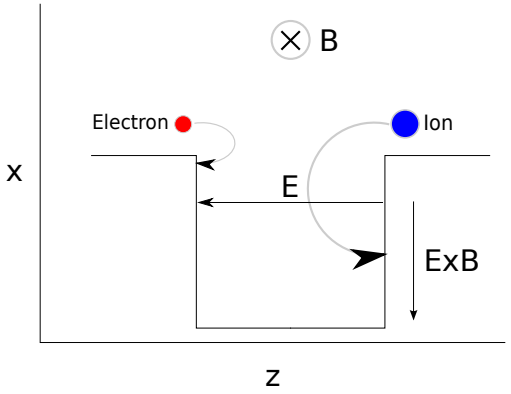

FIGURE 5.5: Electrons and ions orbit in opposite directions. Orbit of the ions takes them deep into the right hand side of the probe.

the alignment of the probe will never be perfectly perpendicular to the magnetic field. A misalignment above the critical angle, $\approx 1^\circ$ for deuterium, will allow electrons to stream along field lines to the surface, causing that surface to float negatively with respect to the plasma potential. The results discussed below are for a field alignment value of $\theta = 10^\circ$. Additional simulations were carried out with θ ranging from $5^\circ \rightarrow 15^\circ$. Varying θ had no significant effect on the simulation results, but the 5° case required more time to reach a steady state, as the ions take a longer time to propagate along the simulation domain for smaller angles. $\theta = 10^\circ$ was chosen as a compromise between shorter run times and matching the experimental set-up. This was the value used by Komm in simulations of the ISP [101].

Collisions between charged particles are neglected in these simulations. The simulation plasma consists of electrons and singly charged ions with no neutrals or impurities present. Plasma-surface interaction effects such as secondary electron emission and sputtering have also been neglected.

5.5 Transport Mechanism

Electrons and ions are observed to reach the collector in both experiments [49] and the simulations even for collector recession depths beyond 2 ρ_i. This observation implies that a cross-field transport mechanism is present driving particles down the tunnel. In the bulk plasma, particles are born at the top of the domain and travel along field lines towards the probe where they will either encounter the top surface of the probe head or will enter the tunnel. From the viewpoint of an observer looking along magnetic field lines, the electron's clockwise orbit takes them towards the left hand side of the tunnel, whilst the anti-clockwise orbit of the ions takes them deep into the right hand side. This is demonstrated in figure 5.5. This results in an electric field across the tunnel of the probe in the negative z direction. The potential structure within the probe tunnel and the resulting electric field is shown in figure 5.6.

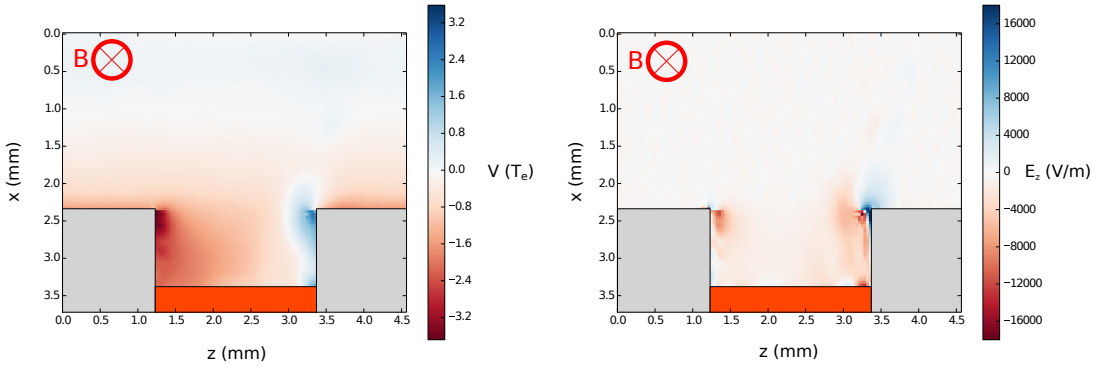

FIGURE 5.6: On the left - cross section of the electric potential. On the right - cross section of the resulting electric field in the z direction. Recession depth, $h = 1.1$ mm. Particles follow the magnetic field lines into and out of the plane shown. Their orbits can take them into contact with the walls, running parallel to the magnetic field, resulting in the potential structure shown.

The electric field in the z direction and magnetic field in the y direction results in an E x B drift that drives particles down the x-axis to the collector (for directions of coordinate axes the reader is referred to figure 5.4). Although the driving mechanism for the cross-field transport is the same for both species, their trajectories down the tunnel are very different. Once in the tunnel, particles will still continue to travel parallel to the field lines (along the y-axis) towards the tunnel wall. If a particle comes into contact with the tunnel wall it deposits it's charge there and is lost from the simulation. In terms of motion parallel to the field, electrons are the more mobile species due to their low mass. As a result, a sheath forms in front of the floating tunnel wall to retard the flow of electrons. Only the most energetic electrons overcome this sheath potential to reach the wall. The less energetic electrons will reflect off the sheath and travel towards the other side of the tunnel. At the same time the electrons are driven down the tunnel due to the E x B drift. As a result, the electrons follow an oscillatory path down the tunnel. The trajectory of an electron, taken from the simulation, that reaches the collector is shown in figure 5.7. The most energetic electrons are lost at the top of the tunnel as they are able to overcome the sheath potential. Therefore a less negative potential is required to maintain floating conditions further down the tunnel. The sheath potential on the wall becomes less negative with depth varying from -200 V at the top of the tunnel to -140 V at the bottom. As a result more and more of the electron population is lost to the walls with only the least energetic not capable of overcoming progressively weaker sheath potentials to make it to the bottom of the probe. The parallel velocity distribution of electrons at the top and bottom of the tunnel is shown in figure 5.8. The width of the distribution narrows deeper into the tunnel as the high energy electrons are lost to the wall.

The tunnel sheath acts to accelerate ions towards the wall so any ions that enter the sheath will be lost to the walls and unable to make it to the probe collector. Once entering the tunnel, an ion will continue its Larmor orbit whilst travelling parallel to the

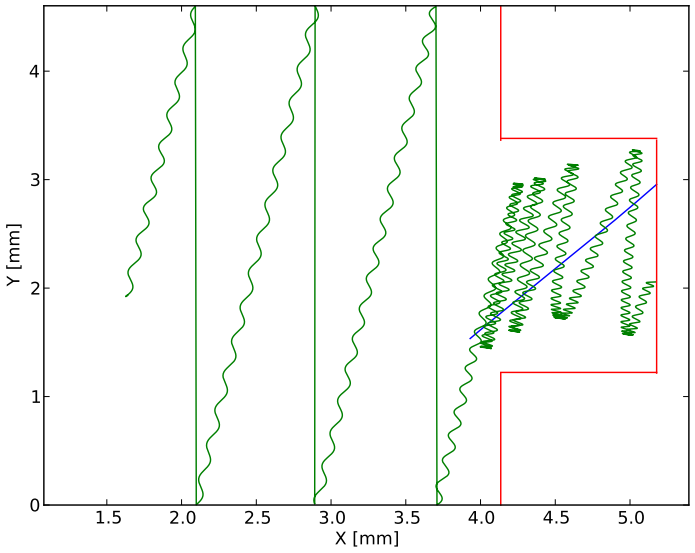

FIGURE 5.7: The trajectory of electrons and ions in the x-y plane is shown in green and blue respectively. Red lines show the walls of the probe. The electron follows the field across the periodic simulation domain until it enters the tunnel. Once in the tunnel the electron reflects back and forth due to the sheath potential. Vertical lines represent the electron leaving the simulation on one side of the periodic boundary and re-emerging on the other side. Ions simply travel down the tunnel due to their orbit whilst travelling parallel to the field. $h = 1.1$ mm.

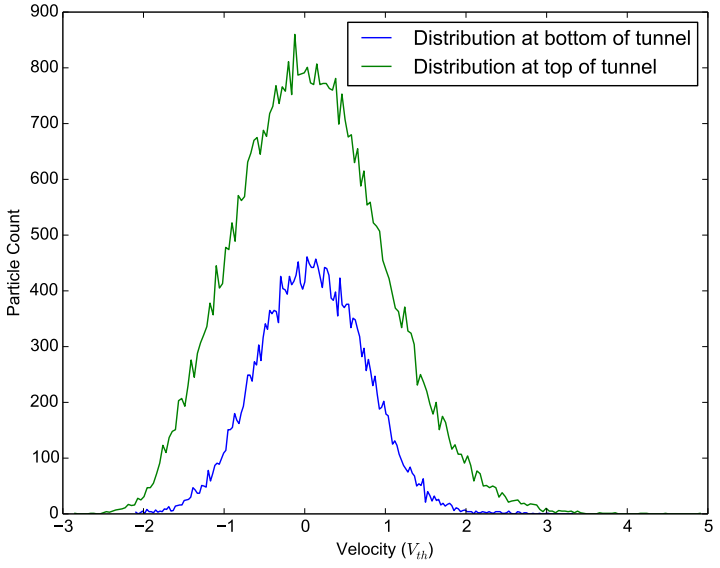

FIGURE 5.8: The parallel velocity distribution for electrons at the top and bottom ($h = 1.1$ mm) of the BPP tunnel. The distribution narrows deep into the probe as the more energetic electrons are able to overcome the sheath potential and hit the wall.

magnetic field towards the wall. To be collected an ion must have sufficient perpendicular velocity to make it to the probe before it's parallel velocity takes it to the wall i.e.

$$\left(\frac{h}{v_\perp}\right) < \left(\frac{d}{v_\parallel}\right) \tag{5.8}$$

where h is the recession depth of the probe and d the tunnel diameter. Ions that reach the probe collector have a higher perpendicular energy than parallel energy when they enter the tunnel. Their perpendicular speed is increased in the tunnel due to the E x B drift.

The contrast in the collection mechanism for ions and electrons was predicted in [90]. The collection mechanism suggests that the proportion of the electron population that can make it to the collector should not be sensitive to the probe tunnel diameter, provided $d >> \rho_e$. The electron parallel velocity will always exceed the E x B drift velocity so electrons will encounter the wall sheath multiple times before they are able to drift to the collector. On the other hand, the collection of ions should be sensitive to the probe diameter. If the probe is too narrow, ions will not have time to complete enough of their orbit to make it to the collector before encountering the tunnel wall. The tunnel must be sufficiently wide so as not to hinder the collection of the ions. This is investigated in section 5.8.1.

5.6 Does the Probe Measure the Plasma Potential?

In order to test the capability of the BPP to measure the plasma potential, simulations were carried out for a probe of diameter 3.2 mm and a depth of 1.04 mm. A simulation was carried out with the probe operating in floating mode to obtain a floating potential measurement (V_{BPP}). Further simulations were carried out in order to determine R and α_{BPP}. In these simulations, the probe was biased positively and negatively with respect to the plasma potential in order to determine I^-_{sat} and I^+_{sat} respectively. It was observed that the currents for both species did not saturate. This behaviour has also been observed in experiments [104]. Following the method of [104], it was necessary to carry out further simulations with different probe bias voltages. The currents obtained at each voltage could then be extrapolated to obtain the value of R at the plasma potential.

The saturation currents increase linearly with probe bias, therefore it was possible to estimate R by linearly interpolating both currents to the plasma potential and defining their saturation values to be at this point. The values for the currents give $R = 3.02$ corresponding to a value $\alpha_{BPP} = 1.1$. These values are higher than what is typically observed in experiments where α_{BPP} is in the range

$$\alpha_{BPP} = 0.6 \pm 0.3 \tag{5.9}$$

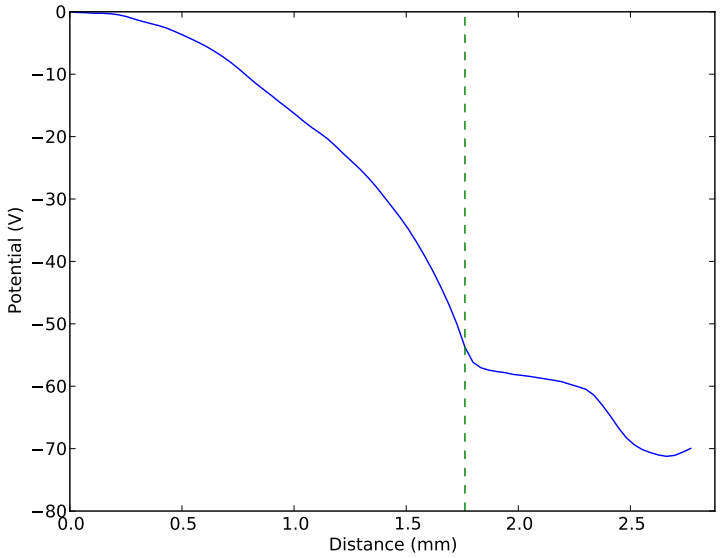

FIGURE 5.9: The plasma potential across the simulation domain, the dashed line shows the location of the BPP tunnel entrance.

However, these estimates were obtained using probes of at least 4 mm in diameter. In section 5.8.1, it is shown that a larger probe size reduces R closer to the value measured in experiments. Nevertheless, if it can be demonstrated that the BPP floats at a potential offset from the plasma potential by the product of $T_e\alpha_{BPP}$ then the BPP mechanism will be validated. Shown in figure 5.9 is a plot of the potential across the simulation domain along the x-axis. The potential at each point represents the average potential across a circular cross-section centered over the BPP collector. The plasma potential is defined as the value at the top of the domain, where the profile is flat before the magnetic presheath (MPS) potential drop. The probe is found to float at a potential of -69 V relative to plasma potential. Based on the values of α_{BPP} and $T_e = 60$ eV, equation 5.1 predicts the plasma potential should be -3.8 V. This is very close to the value for the plasma potential in the simulation (0 V). The BPP will therefore float at a potential offset from the plasma potential by a factor of $T_e\alpha_{BPP}$. An $\alpha_{BPP} = 0$ would be required for the BPP to truly float at the plasma potential.

Simulations were carried out with an increased electron and ion temperature of 120 eV to determine if particle temperature had an impact on α_{BPP}. As before, multiple simulations were carried out for different probe bias voltages so that α_{BPP} could be measured by interpolating the currents. For these runs, a value of $\alpha_{BPP} = 1.38$ was observed, which is not significantly higher than the value found for $T_e = 60$ eV ($\alpha_{BPP} = 1.1$). It does not appear that the temperature strongly effects the operation of the BPP over the range of $60eV \leq T_e \leq 120eV$ considered in this study.

5.7 Can the probe be used to make Electron Temperature measurements?

Additional simulations were carried out in order to test the capability of the BPP-LP pair to make electron temperature measurements. The BPP was replaced with a flush-mounted probe (FMP) and operated in floating mode to obtain V_{LP}. As discussed previously in section 5.6, α_{BPP} and V_{BPP} have already been measured. As in experiments, our simulations are not capable of measuring α_{LP}. In magnetised plasma the collection length of the probe operating in electron collection mode can extend very far into the plasma. It is not possible to capture this region in our simulation domain and so it is not possible to collect I^{-}_{sat}. Following experimental procedure we will therefore use the theoretical value for α_{LP} provided by equation 5.7.

As before, results are stated for the 3.2 mm diameter probe with an electron temperature of 60 eV. The FMP is found to float at a potential $V_{LP} = -129$ V. Combining this with $\alpha_{BPP} = 1.1$, $V_{BPP} = -69$ V and the theoretical value of $\alpha_{LP} = 2.14$ for the reduced ion mass we obtain a value of $T_e = 58.3$ eV which is in very good agreement with the specified temperature. This method is a viable way of making fast electron temperature measurements provided α_{BPP} is known. The measurement of T_e can be combined with V_{BPP} to determine the plasma potential.

5.8 Ball-Pen Probe Design Considerations

5.8.1 Effects of Probe Diameter

In order to investigate the effects of probe diameter, three probes of different width were simulated. The probe diameters were a) 1.08 mm, b) 2.16 mm and c) 3.24 mm. All probes were recessed to the same depth of 1.04 mm. The ion Larmor radius in the simulations was $\rho_i = 1.02$ mm. For each probe diameter, three simulations were carried out: one with the probe operating in floating mode and two biased cases where the collector was in ion collection and electron collection mode. The floating potential of the collectors is shown in figure 5.10 along with the measured value of R. The ratios presented were obtained by dividing one current for each species. A linear interpolation has not been carried out so the true value of R is not known. The values are presented here as they demonstrate the effects of probe diameter on BPP measurements even if their absolute value is not correct.

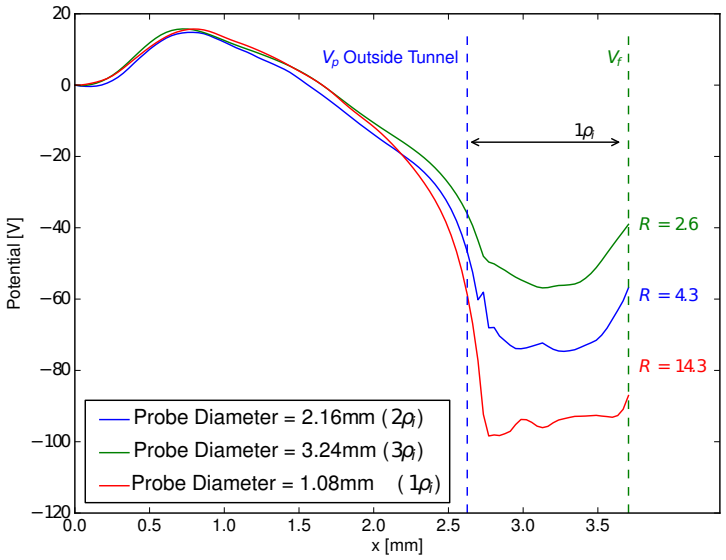

FIGURE 5.10: The potential structure across the simulation domain. The floating potential of the probe varies with tunnel diameter as does the value of R. The potential structure near $x = 0$ is a result of the source sheath, an artefact of particle injection in this region.

With increasing width, a lower ratio R and a less negative value for V_{BPP} is observed. Beginning with the ions we find the current per unit area increases as the diameter increases. This is consistent with the collection mechanism: with a wider probe, ions have more time to reach the probe before their parallel motion brings them to a tunnel wall, therefore a higher proportion of the ion population reaches the probe. The electron current per unit area remains approximately constant with increasing probe diameter.

In order to allow a direct comparison with experiments, a set of simulations with a probe diameter of 4 mm and depth of 1 mm were carried out using a realistic ion mass and a field strength of 1.3 T, equivalent to the conditions used by Adámek et al in [49]. The following measurements were obtained

$$R = 2.8 \quad \alpha_{BPP} = 1.04 \quad V_{BPP} = -67.6V \tag{5.10}$$

which for a specified electron temperature of 60 eV and plasma potential of 0 V are in good agreement with equation 5.1. The value of α_{BPP} obtained for this probe is very similar to the value obtained for the 3.2 mm probe ($\alpha_{BPP} = 1.1$) which suggests the diameter might not be an important consideration in the design of BPPs provided a threshold value is met. However, the value for α_{BPP} obtained in the simulations is outside the accepted range derived from experiments given in equation 5.9. This range is obtained using conical collectors where as the simulated probe was flat. The effects of BPP diameter were investigated on the linear plasma device Mirabelle [105]. However, due to the low magnetic field strength used in the experiments, the electron Larmor

radius was comparable to the tunnel diameter and the effectiveness of the probe to shield the electron current strongly depended upon the probe geometry. This regime of operation is not applicable to the simulations carried out. To the authors knowledge, an experimental comparison of the influence of probe diameter on the value R, for fusion relevant plasmas, has not been reported. However, in [106], three BPPs with a flat collector were placed into the edge region of CASTOR together with a BPP with a conical collector to make simultaneous measurements of the plasma potential. The flat collector probes were of different diameter: 1 mm, 2 mm and 4 mm and the conical collector had a diameter of 2 mm. The authors concluded that the diameter was not a critical construction parameter but differences in the value of the measured plasma potential were observed. Values for R were not reported. Differences in the plasma potential measurements were attributed to an alignment of the probes along different magnetic flux tubes. However, in the region of minimal curvature of the poloidal field, where the misalignment was lowest, it was found that the floating potential of the flat collector probes increased with probe diameter. If the floating potential of the probe varied with probe diameter, this could indicate that the value of R also changes with probe diameter. Out of the four probes, the 2 mm conical BPP was consistently found to float at the highest potential. This would suggest a smaller diameter conical BPP can achieve the same ratio R as a larger, flat collector BPP. The differences in potential measured in experiment were not as extreme as the differences found in the simulations. However, in the simulations, $T_e = 60$ eV compared with $T_e = 20$ eV in this experiment. This does not affect the capability of either probe to make plasma potential or electron temperature measurements, provided α_{BPP} is known for the probe that is employed.

5.8.2 Effect of Probe Recession

In the experiment described in [49] it was found that the value of R reached a minimum when the probe was recessed by 0.5 mm ($1\rho_i$). Once the probe was recessed beyond this depth, the value of R increased. Simulations have been carried out to test the sensitivity of R on collector recession and have found a similar trend. Both electron and ion currents to the probe decrease as the probe is recessed deeper into the tunnel, as more particles are absorbed by the tunnel walls. However, the electron current decreases less strongly than the ion current as electrons can reflect off the sheath formed along the interior walls of the probe while being driven towards the collector by E x B drifts. The reduced electron current is a result of the potential on the tunnel wall decreasing with depth into the tunnel, i.e. it becomes closer to the plasma potential. As a result, less of the electron population will be reflected by the weaker sheath potential. Increasing the probe depth makes it more likely that an ion's parallel velocity will take it into a tunnel wall before it can make it down to the collector. It appears that as long as the BPP is recessed beyond a few ρ_e the electrons become magnetically shielded and can only access the collector via E x B drift motion. The probe then operates as a BPP. As long as this criteria is met and the probe depth is fixed with known α_{BPP} the

probe depth is not thought to be an important parameter. However, beyond a certain depth, corresponding approximately to when equation 5.8 is not satisfied, most ions will be absorbed before making it to the collector and the measurements will become dominated by noise. Simulations and experiments suggest a depth of 1 mm is sufficient for tokamak plasma conditions in order to minimise α_{BPP}.

5.9 Conclusions and Future Work

3D3V PIC simulations of the BPP have been carried out for the first time. The simulations have verified that the BPP measures a potential offset from the plasma potential by a factor $T_e\alpha_{BPP}$. BPPs in practice have obtained values as low as $\alpha_{BPP} = 0.6$. For electron temperatures on the order of 10 eV, the difference between the floating potential of the BPP and the plasma potential will then be several volts. The floating potential measurement from the BPP is closer to the plasma potential than the floating potential of a standard Langmuir probe, however, the electron temperature is still required to determine the plasma potential from the BPP floating potential measurement and so the BPP is not capable of providing direct measurements of this quantity. By simulating both a LP and a BPP the source temperature for the electrons was recovered, validating the BPP-LP method for making fast electron temperature measurements. Using a BPP and LP, operated in floating mode, in close proximity to each other could then provide fast measurements of T_e which can then be used to determine Ψ.

The mechanism that allows electrons to reach the collector even when it is recessed far beyond their Larmor radius has been confirmed. Inside the tunnel, electrons oscillate along field lines, reflected by the wall sheaths, whilst simultaneously undergoing E x B drift motion towards the collector. The larger orbit of the ions allows them to reach deeper into the tunnel, their perpendicular motion further facilitated by the E x B drift. Ions must reach the collector before their parallel motion brings them to a tunnel wall. This mechanism suggests the probe diameter could be an important consideration in the design of ball-pen probes, at least until a threshold diameter is exceeded. Marginal reduction in the value of α_{BPP} was observed when increasing the probe diameter from 3.2 mm to 4 mm in the simulations, suggesting this threshold may have been met. Further simulations of smaller BPPs, to obtain accurate values of α_{BPP}, are required to test the existence of a threshold diameter. This work would benefit from experimental measurements of α_{BPP} for BPPs of different diameters in fusion plasmas. Larger α_{BPP} values are obtained in the simulations than in experiment. Possible reasons for this discrepancy are that a flat collector was simulated, experimental α_{BPP} values have only been reported for conical collectors, conical collectors may reduce the ratio R more efficiently. Secondly, for the simulations that were completed with realistic ion mass in order to directly compare against Adamek's original measurements, simulated electrons and ions were at a temperature of 60 eV, whereas in the experiment, the temperature was estimated to be 10 eV. Reducing the simulated temperature would have increased

the number of grid cells in the simulations, making the simulations too computationally expensive. Based on the 120 eV simulations carried out, it is not thought that the temperature would have a significant impact on the simulation value of α_{BPP}. A final cause of the discrepancy could be the exclusion of secondary electron emission (SEE) from the BPP collector. SEE could occur when an ion strikes the surface of the collector. An electron emitted from the surface of the collector would be equivalent to an ion collected by the surface. SEE could then act to enhance the measured ion current, reducing the measured value of α_{BPP}. It would be of interest to add a SEE model into the PIC simulations and test this effect on the BPP measurements.

Probe depth is not an important design consideration, provided the collector is recessed sufficiently such that the electrons are magnetically shielded from the collector. It was found that recessing the probe a depth greater than several ρ_e is sufficient. The voltage applied to a BPP should be swept initially in experiments to measure α_{BPP}. Once this value is acquired it is then possible to use the BPP to extract the electron temperature and plasma potential. Based on the results of the simulations, a BPP of diameter at least 3.2 mm and depth of at least 1 mm should be implemented to minimise α_{BPP} in fusion plasmas.

The simulations in this chapter focused on fusion relevant plasma conditions. The simulations could be extended to low-temperature devices such as the magnetron to test the capabilities of the BPP in these plasmas. Although the lower temperatures will reduce the Debye length, this is offset by lower densities, allowing the Debye length to be resolved. This extension is carried out in Chapter 6.

Chapter 6

Probes in Low Temperature Plasma

6.1 Introduction

As detailed in Chapter 5, ball-pen probes (BPP) have been implemented in fusion plasmas to make measurements of the plasma potential (Ψ) and electron temperature. These plasmas are characterised by high temperatures, high densities, strong magnetic fields and negligible collisions between ions and the neutral particles due to low neutral particle densities. BPPs have also been implemented in low temperature, low density and weakly magnetised plasmas where ion-neutral collisions can be significant [91, 105, 107]. These plasmas are useful in various technological applications such as microelectronics and the treatment of material surfaces [108]. In [105], a BPP was used in helium and argon plasmas at pressures in the 10^{-2} Pa range, with an electron density between $10^{16} - 10^{17}$ m^{-3}, an electron temperature between $1 - 7$ eV and various magnetic field strengths up to a maximum of 80 mT. Three BPPs of inner diameter 1, 0.6 and 0.3 mm were tested and compared to measurements of the plasma potential made by an emissive probe. It was found that the floating potential measurement made by the larger probes increasingly deviated from the plasma potential as the magnetic field strength was increased, with the probe floating negatively with respect to the plasma potential. However, the smaller probe was capable of measuring the plasma potential across the range of field strengths. In these plasma conditions, the electrons are magnetised but the ions are unmagnetised which is a different regime from a tokamak plasma in which both species are magnetised. The BPP in this plasma was insensitive to the ion gyroradius, its capability to measure the plasma potential was determined by its ability to effectively screen out the electron current. The electrons can only reach the collector by cross-field transport, if this transport can be reduced, the probe was able to operate as a BPP. It was found that the ratio of λ_D/D_{BPP} was important, where D_{BPP} is the diameter of the BPP. If $\lambda_D >> D_{BPP}$ the sheath of the floating tunnel covered the entrance to the BPP, preventing the perpendicular transport of electrons into the tunnel. If this condition was

not met, then a region of positive space charge in the tunnel exists, created by the ions which can penetrate more easily into the tunnel. This allows electrons to be driven into the tunnel by E x B drifts. However, in regimes where the tunnel diameter was smaller than the electron Larmor radius (ρ_e), drifting electrons would hit the tunnel wall before making it down to the collector thus reducing the perpendicular electron flux. For this reason, the 0.3 mm probe was still capable of operating as a BPP at 80 mT whilst the larger probes exceeded the size of the electron Larmor orbit and could not screen out the electron current. Overall, it was found that high values of λ_D/D_{BPP} and ρ_e/D_{BPP} were required for successful operation of the BPP when the ions were unmagnetised.

In [107], three BPPs with tunnel diameters ranging between $1.5-2$ mm were installed on a magnetron device with an argon plasma of density $\approx 1 \times 10^{16}\, m^{-3}$. In the experiments, the electron temperature ranged from $0.9-3.4$ eV, the pressure ranged from $1-20$ Pa and the field strength from $20-40$ mT. The work found a limit of applicability for use of the BPP in low temperature plasmas. The probe was found to float around the plasma potential provided the ratio of magnetic field strength to pressure exceeded 10 mT/Pa. Below this value, the electrons are not sufficiently magnetised and can travel to the probe collector unimpeded, the BPP collector then floated at the same potential as a standard Langmuir probe, regardless of the collector recession depth. In both papers the ions were unmagnetised and so the BPPs were insensitive to the gyromotion of the ions. The probe behaviour was completely different from BPPs in fusion plasmas where both species are magnetised. In our work we extend the investigation of the applicability of BPPs in low temperature plasmas, to field strengths found in tokamaks, in regimes where both charged species are magnetised.

The results presented in this chapter were obtained from experiments performed in the apparatus illustrated in figure 6.1. The apparatus consisted of a rectangular, aluminium chamber with a cross sectional area of 14 cm^2 which was 7.5 cm deep. A 13.56 MHz radio frequency (RF) argon plasma is generated in a parallel plate capacitively coupled cell. The electrodes, 4 cm in diameter were spaced 4 cm apart. The plasma is powered by a Dressler Cesar 136 RF power supply coupled through a matching unit to the powered electrode. A Helmholtz coil is used to generate the magnetic field uniformly (within 0.3%) throughout the plasma. A three-phase powered variable transformer (maximum ratings : 120 Vdc, 1.6 kA) was used to supply current to the Helmholtz coils. The coils were water cooled to dissipate the ohmic heat from the high current and to limit the resistance of the coils. The plasma density varies from $10^{15} \rightarrow 10^{17}\ m^{-3}$ and the electron temperature ranges from $1 \rightarrow 4$ eV, over a range of powers, pressures and magnetic field strengths.

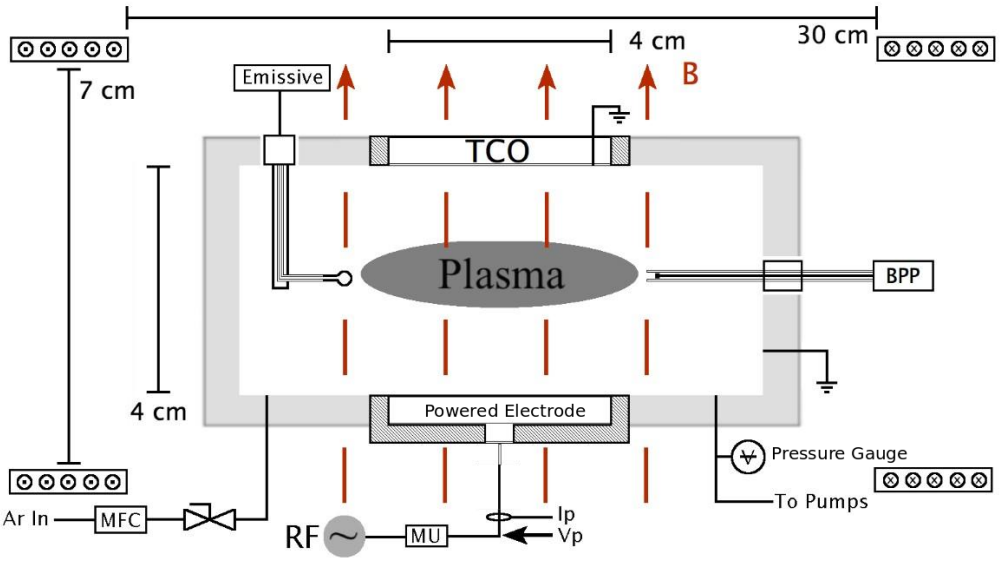

FIGURE 6.1: Schematic of the experimental system equipped with a transparent conductive oxide electrode (TCO), a mass flow controller (MFC), a matching unit (MU), a current sensor (Ip) and a voltage probe (Vp). The plasma was diagnosed with a ball-pen probe (BPP) and an emissive probe.

In this experiment, four BPP designs were investigated under various magnetic field strengths, from $0-0.5$ T. Two collector diameters of 2 mm and 4 mm were investigated, with the outer diameter of the tunnel being 3 mm and 5 mm respectively. For each diameter, experiments were carried out with a flat collector design and a tapered, conical collector design. This allows the effect of varying the size of the collector area and it's shape to be studied. The BPP collectors were made of stainless steel and mounted on a retractable arm so that the effect of recession depth could be studied. The tunnel was formed of aluminium oxide, an insulating material. The BPPs could be operated in floating mode or biased to extract an I-V characteristic. In order to obtain accurate values of the floating potential, a high impedance circuit was required, this is discussed further in section 6.3. I-V characteristics were obtained by connecting the collector to a commercial Langmuir probe acquisition system. The system used was a Hiden ESPION Advanced Langmuir Probe (Model EPIU). ESPsoft (Version 7.2) was used to communicate with the unit to generate the I-V curves. The floating potential measurements of the BPPs are compared to the plasma potential measurements inferred from the emissive probe, over a range of plasma powers, pressures and field strengths. The emissive probe consisted of a thoriated tungsten wire, 25 μm in diameter and 1 cm long. The electrical arrangement for the emissive probe and the underlying theory behind its operation is discussed in section 6.2. The chapter then moves on to explain the need for high impedance circuity to make accurate floating potential measurements in a low temperature plasma. Results for each of the BPP collectors and the emissive probe are then discussed.

6.2 Emissive Probe Theory

The emissive probe is an advanced probe technique designed to measure the plasma potential directly in magnetic fields. Conventional Langmuir probes cannot accurately measure the plasma potential in magnetic fields due to the distortion of the I-V characteristic by the magnetised electrons. The underlying principle of both the BPP and the emissive probe is to balance the magnitudes of the ion and electron saturation currents. If these two quantities are equal, the probe will float at the plasma potential. Unlike the BPP that aims to reduce the magnitude of the electron saturation current, the emissive probe instead enhances the ion saturation current. The emissive probe consists of a thin filament of wire that is heated, causing it to emit electrons by thermionic emission. If the probe is biased negatively with respect to the plasma potential, the electrons escape the probe surface and are accelerated into the plasma. In terms of current to the probe, an electron emitted is equivalent to an ion collected, so the emitted electrons enhance the observed ion current to the probe. If the probe is biased more positively than the plasma potential only the high energy tail of the electrons can escape into the plasma. An I-V characteristic for a heated emissive probe then consists of the ion current and both the emitted and collected electron currents. The collected electron current (I^-) is the same as that of a standard probe. For an ideal probe, the collected electron current can be expressed as

$$I^-(V_{probe}) = \begin{cases} I^-_{sat} \exp\left(\frac{\Psi - V_{probe}}{T_e}\right), & \text{if } V_{probe} < \Psi. \\ I^-_{sat} & \text{if } V_{probe} \geq \Psi. \end{cases} \tag{6.1}$$

The emitted current (I_{e0}) is given by

$$I_{e0}(V_{probe}) = \begin{cases} I_{e0} & \text{if } V_{probe} \leq \Psi. \\ I_{e0} \exp\left(\frac{\Psi - V_{probe}}{T_{probe}}\right), & \text{if } V_{probe} \geq \Psi. \end{cases} \tag{6.2}$$

At biases less than the plasma potential (Ψ), at a constant emissive probe temperature (T_{probe}), the emission current is constant and equal to I_{e0}, where I_{e0} is the temperature limited current given by the Richardson-Dushman equation [109]

$$I_{e0} = A{T_{probe}}^2 S \exp\left(\frac{e\phi_w}{T_{probe}}\right) \tag{6.3}$$

where A is the Richardson constant [110] , ϕ_w is the work function of the metal and S is the surface area of the wire. In this regime, the emission of electrons is limited by the temperature of the wire, so this regime is known as the temperature limited regime.

A significant flux of emitted electrons can change the sheath structure around the probe leading to a reduction of the floating potential and an effect on the shape of the I-V characteristic around the plasma potential. These space-charge effects need to be taken into account if the correct plasma potential is to be obtained from the I-V curve of an emissive probe. Various methods have been developed to extract Ψ, of these the

inflection point in the limit of zero emission method is regarded as the most accurate method to measure the plasma potential [111]. For the inflection point in the limit of zero emission method, inflection points (maxima in the first derivative of the I-V curve) are measured for the probe at various low emission levels, such that the temperature limited emission current is on the order of the electron saturation current or less. The potential of these inflection points is then plotted against emission current producing a linear plot which is then extrapolated to zero emission to obtain the plasma potential [112]. In the presence of strong magnetic fields, the I-V curve in the electron collection region is distorted and the inflection point can be hard to determine [112]. As a result, an alternative method for measuring the plasma potential was required. It is known that as an emissive probe is heated, the floating potential of the probe rises as the emission increases, rising rapidly at first and then plateauing at a potential deemed to be the plasma potential [113–115]. This is known as the floating point in the limit of large emission method. This follows from the equation for the floating potential (V_F) of a heated probe, valid for probe voltages below the plasma potential (Ψ) [116]

$$V_F = \Psi - T_e \ln R = \Psi - T_e \ln \left(\frac{I_{sat}^-}{I_{sat}^+ + I_{e0}} \right) \tag{6.4}$$

As I_{e0} increases the ratio R tends to unity. At this point the probe should float at the plasma potential. However, numerical simulations show that the floating probe will float $1.5T_e$ V less than the plasma potential [117], as the high emission current affects the sheath structure around the probe. Due to the strong magnetic fields, the floating point in the limit of large emission method was used to obtain the following emissive probe results presented in this chapter.

The electrical arrangement for the emissive probe is shown in figure 6.4. The probe wire was looped into a semicircle and then fitted into the probe stem. The wire was heated by passing a 50 Hz ac current through it. AC mains was supplied to a variable step down transformer. The output of this was fed into a fixed step-down transformer and connected to the probe. Adjustment of the variable transformer allows currents up to several Amps to heat the probe. The floating potential was measured by a potential divider with an attenuation ratio of (11:1) and a voltage probe (V.P). This was connected to the center of the secondary output so as to measure the potential in the centre of the filament.

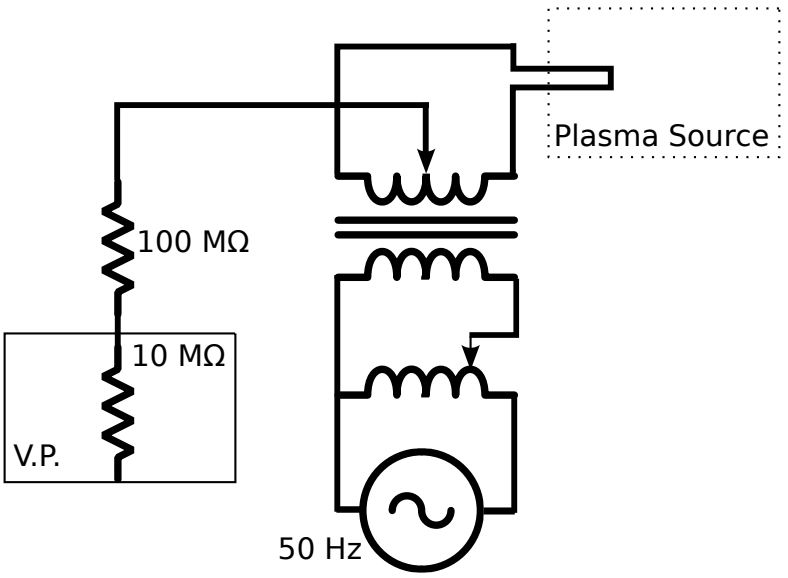

FIGURE 6.2: Schematic of the circuit used to heat the emissive probe and measure the floating potential using a voltage probe (V.P).

6.3 High Impedance Circuitry for Ball-Pen Probe Floating Potential Measurements

When measuring the floating potential of a probe, the probe can be considered as the voltage source (V_s) in the following circuit:

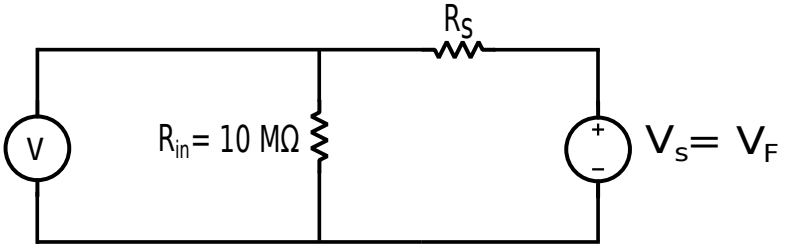

FIGURE 6.3: Representation of the probe circuit to measure the floating potential.

The potential difference is measured by a voltage probe with a resistance of 10 MΩ. The other source of resistance in the circuit is R_S which represents the impedance between the collector and the plasma and is an unknown quantity. For a standard Langmuir probe, R_S is the sheath resistance, $R_S << R_{in}$, therefore most of the potential drop occurs across R_{in} and the voltage probe is able to measure V_s. However, for a BPP, R_S is the impedance to the ions and electrons moving inside the tunnel. With a recessed collector, particle collection to the probe is not due to motion parallel to the magnetic field, but is due to cross-field transport. This greatly increases the effective impedance of the BPP and is a complicated function of recession depth, tunnel geometry and plasma parameters. As a result, R_S can be much greater than R_{in} and so the potential drop does not occur entirely across R_{in}. As the value of R_S is not known, its effect can not

be factored out. By adding an additional high valued resistor into the circuit (R_2), with a high impedance, to form a potential divider, the effect of the BPP's high impedance can be reduced.

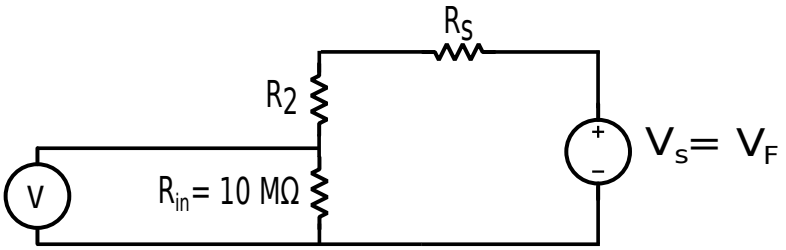

FIGURE 6.4: A potential divider is used to determine the correct floating potential of the probe.

Provided $R_2 >> R_S$ and $R_2 >> R_{in}$, V_s can be determined from the reading on the voltage probe (V_{out}).

$$V_s = V_{out}\frac{(R_2 + R_{in})}{R_{in}} \tag{6.5}$$

Once the collector is recessed inside the BPP tunnel, the impedance can rise to several hundred MΩ [105]. Therefore, R_2 must have a very high impedance. Figure 6.5 shows the floating potential measured by the voltage probe as the value of R_2 is increased. Even for impedance values as high as 700 MΩ, the effect of the probe impedance is still evident and hence the value of V_F has yet to saturate. In order to obtain sufficient impedance, the above circuit was replaced by a high impedance voltage follower circuit using the operational amplifier OPA452T (by Texas Instruments) that had a high input impedance of 10^{13} Ω. This operational amplifier has previously been used in [107] to make direct floating potential measurements of a BPP in a low temperature plasma. The voltage follower circuit is show in figure 6.6.

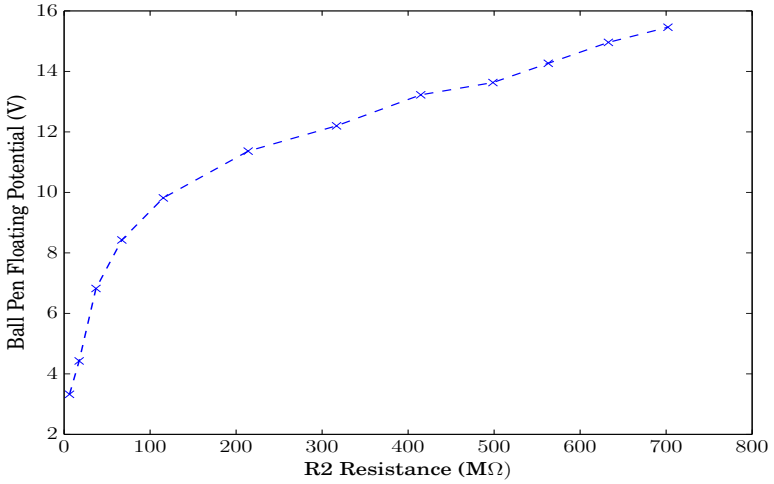

FIGURE 6.5: The measured value of the BPP floating potential with increasing resistance of R_2 in the potential divider circuit. As R_2 increases so does the measured floating potential.

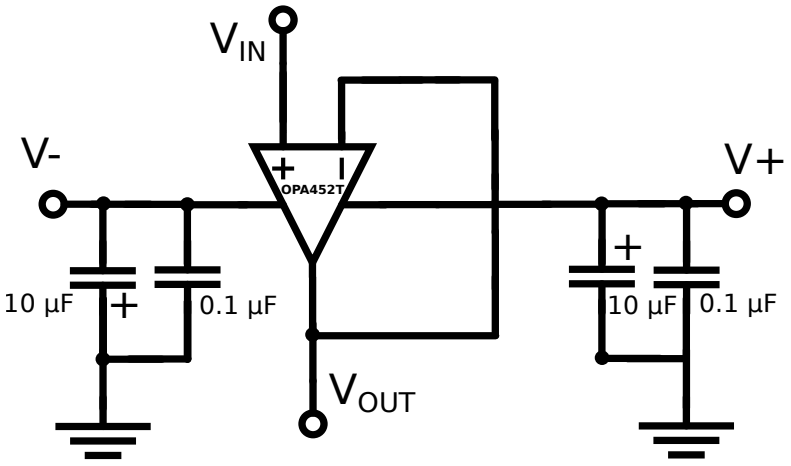

FIGURE 6.6: The voltage follower circuit used to provide high impedance. This is required in order to make accurate measurements of V_F.

6.4 Results

Initial experiments were carried out with a Langmuir probe in place of the BPP in order to check the validity of the emissive probe plasma potential measurements for a range of plasma powers and pressures. The Langmuir probe tip in these experiments was a 1 cm long, 25 μm diameter tungsten wire. Plasma potentials from the Langmuir probe were obtained from the maximum in the first derivative of the I-V characteristics. Derived values of the plasma potential for both probes are shown in figure 6.7. In these comparison runs the plasma was unmagnetised. Magnetising the plasma distorts the electron collection region of the Langmuir probe I-V curve, increasing the noise and reducing the accuracy of the plasma potential measurements. The plasma potential measurements from both probes agree within 3 eV which is approximately the electron temperature, this suggests the floating point method is valid. The emissive probe measurement should remain valid in magnetised plasma up to 250 mT, after which the electron Larmor radius becomes smaller than the diameter of the emissive wire [118].

The capability of the BPP to make plasma potential measurements for a range of magnetic field strengths was tested for each collector. For each experiment the plasma power and pressure were held constant, at 10 W and 0.45 Pa respectively unless otherwise stated. Care was taken to ensure the field strength remained constant throughout each experiment. The collector began fully recessed inside the tunnel at recession depth, $h = -10$ mm and was then moved forward in 1 mm increments with a new value for V_F recorded at each position. After the final reading was taken at $h = 5$ mm (collector outside the tunnel), the magnets were turned off to allow them to cool. The collector was then fully recessed before beginning the investigation under a new field strength. The results obtained from the 2 mm tapered collector are shown in figure 6.8. The pressure was 0.45 Pa and the power was 10 W.

In the unmagnetised plasma the probe does not operate as a BPP. Once the collector

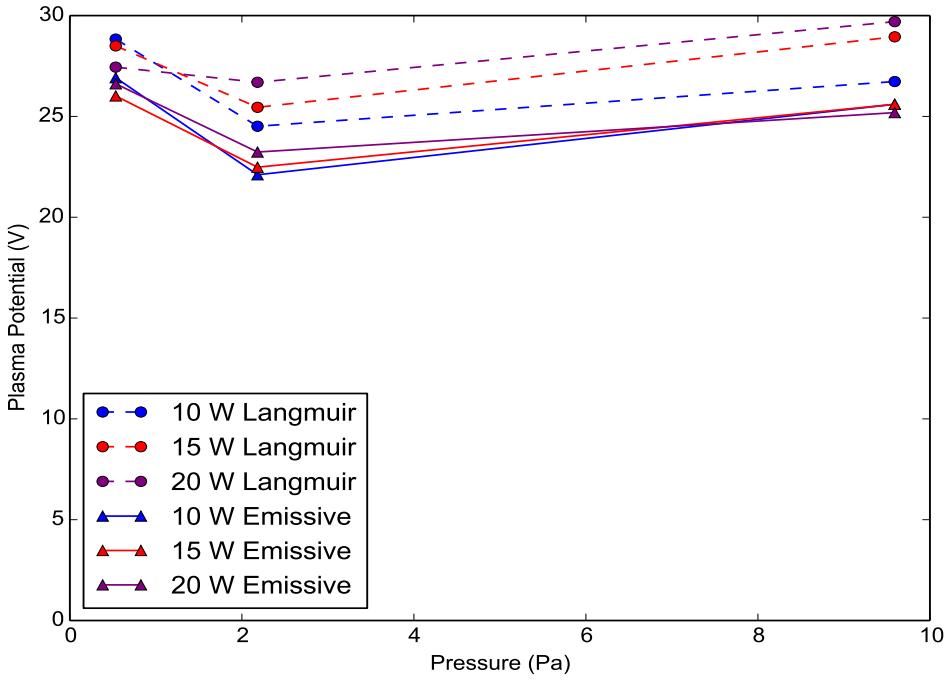

FIGURE 6.7: The plasma potential as measured by the emissive probe and the Langmuir probe for a variety of plasma powers and pressures.

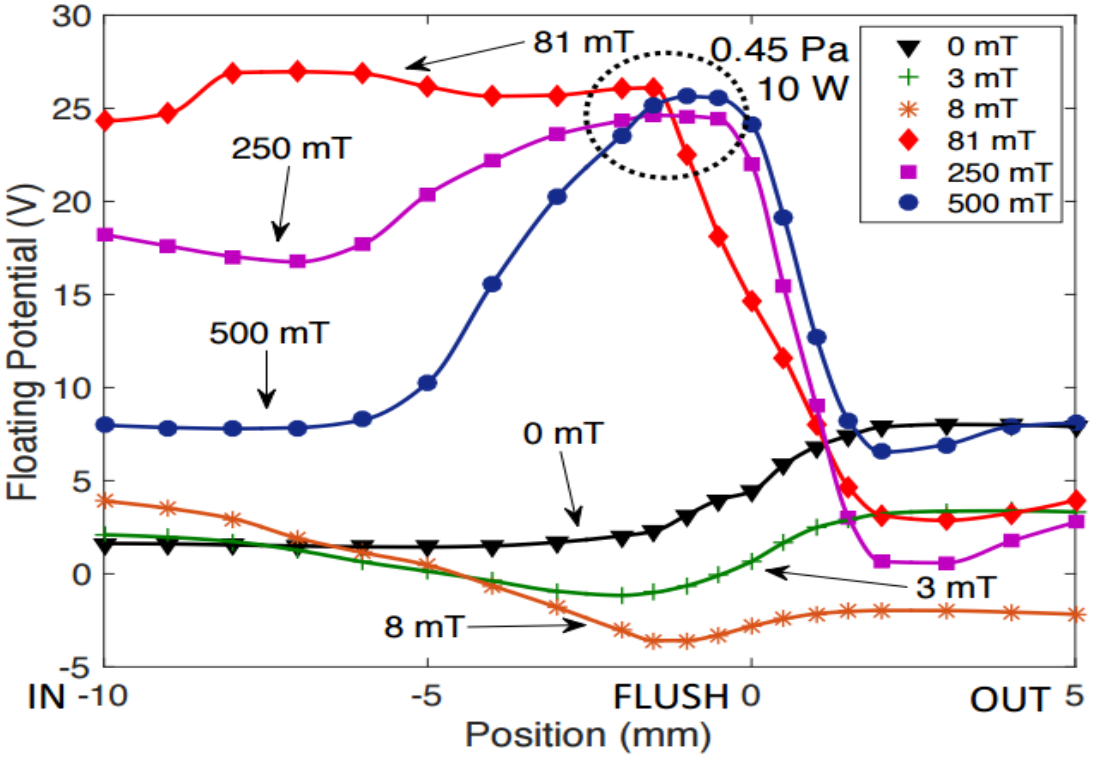

FIGURE 6.8: The floating potential of the 2 mm tapered BPP collector as a function of recession depth for different field strengths. The circled region represents the peak potential reached by the probe for the magnetic field strengths equal to or above 81 mT. The probe does not operate as a BPP below this field strength.

is recessed inside the tunnel there is a decrease in the floating potential and little variation with further recession. The probe is also unable to operate successfully for the low field runs. In this regime the electrons are magnetised but the ions are not. The electron Larmor radius is approximately 0.5 mm for the 8 mT case (assuming $T_e = 3$ eV), the tunnel diameter is then 4 ρ_e and so the probe is unable to effectively screen out the electron current to the collector. The probe begins to exhibit BPP behaviour on increasing the field strength to 81 mT. Now the ions as well as the electrons are magnetised, with an ion Larmor radius of approximately 1.2 mm. The collector potential begins to climb as the collector is recessed, reaching a peak potential at ≈ 25 V for the three highest field strengths. The 81 mT case shows a large plateau region in which there is little variation of the floating potential with probe recession. The length of this plateau region decreases with increasing field strength. As discussed in Chapter 5, in order for ions to reach the collector their motion around the field lines must bring them to the collector before their parallel motion brings them to a tunnel wall. Their perpendicular motion is assisted by E x B drifts. As the field strength increases, the Larmor radius decreases. Once the probe is recessed beyond $\approx 10\rho_i$ only a limited portion of the ion population current can reach the collector, the collector then floats more negatively to repel electrons which are still capable of reaching it by E x B drift motion and reflecting off the sheaths of the tunnel wall. It would appear that the depth of the collector is an important design constraint in strongly magnetised, low temperature plasmas where the Larmor radius of the ions is much smaller than that of an ion in a fusion plasma. In fusion plasmas T_i is approximately equal to T_e which is on the order of tens of eV. The probe depth is not an important parameter for the intermediate 81 mT case.

The experiment was then repeated for the 2 mm flat collector. The plasma had to be switched off so that the new collector could be inserted into the vacuum chamber. As a result, the plasma conditions may vary for the different collectors, although both were operated at the same power and pressure. Figure 6.9 shows the results of the identical experiment with the flat collector as well as the results under a higher operating pressure of 9.6 Pa.

For the low pressure run, the flat collector exhibits the same behaviour as the tapered collector, only operating as a BPP once the ions become magnetised. The 81 mT case again has the largest plateau region, although there is a decrease in the floating potential once the flat collector is deeply recessed. This drop was also observed for the tapered collector but to a lesser extent. Higher magnetic field strengths (i.e. the 250 and 500 mT cases) are required to maintain BPP behaviour once the pressure is increased to 9.6 Pa. In a fusion plasma the neutral gas pressure is on the order of 10^{-6} Pa and the effect of collisions on charged particle motion in the BPP tunnel can be neglected. However, at high neutral pressures, the ions undergo multiple collisions in a gyro-orbit destroying their magnetisation. The 81 mT, 9.6 Pa case (8.4 mT/Pa) falls short of the minimum 10 mT/Pa required for the probe to operate as a BPP [107] which reduces the peak floating potential. While the 81 mT, 0.45 Pa case (180 mT/Pa), far exceeds

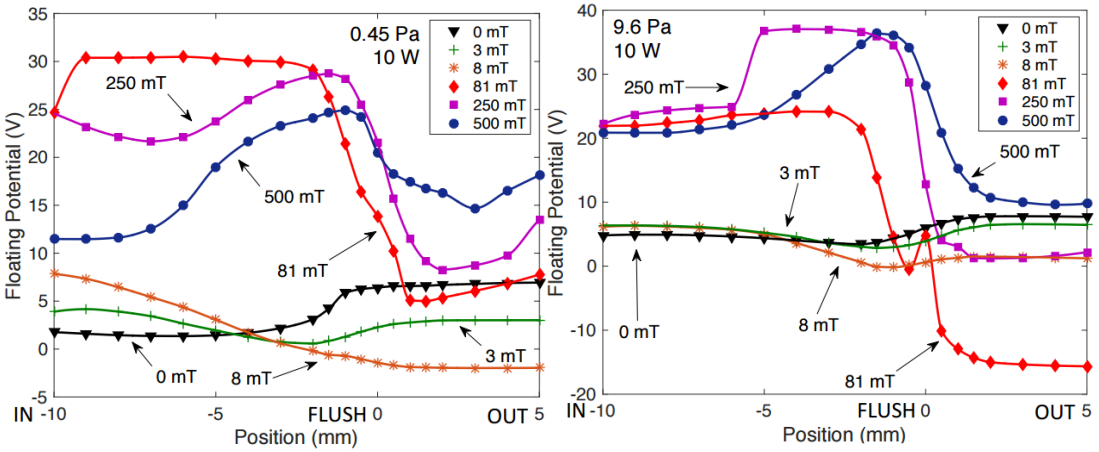

FIGURE 6.9: The floating potential of the 2 mm flat BPP collector as a function of recession depth for different field strengths. The plasma pressure was 0.45 Pa and 9.6 Pa for the left and right plots respectively.

Magnetic field strength B	0 T or 0.25 T
Magnetic field inclination θ	10°
Plasma density n	$1. \times 10^{15}$ m^{-3}
Electron temperature T_e	3 eV
Ion temperature T_i	0.025 eV
Ion Larmor radius ρ_i	0.4 mm
Electron Mass m_e	9.11×10^{-31} kg
Ion Mass m_i	6.63×10^{-26} kg
Ion Charge Z	1.6×10^{-19} C

TABLE 6.1: Typical plasma parameters used in the simulations of the BPP.

this threshold value. An increase in the peak potential of 5 V is observed in the high pressure case as compared to the low pressure case. This increase was also observed in the emissive probe floating potential.

Particle-In-Cell simulations of the 2 mm flat collector were carried out using the model introduced in Chapter 5. The reduction in plasma density of more than a factor of 100 from the MAST SOL enabled the use of much larger grid cells and therefore larger probe depths could be explored. For these runs, singly charged ions were assumed with realistic ion masses. The simulation parameters are given in table 6.1. Two sets of simulations were carried out, an unmagnetised set and a magnetised set in which the magnetic field strength was set to 250 mT. The probe was operated in floating mode in these simulations and the plasma potential was set to 25 V. Collisions are neglected in the simulations. The results of these simulations are shown in figure 6.10.

As observed in experiments, the simulated probe doesn't operate as a BPP in the unmagnetised case as it unable to screen the electron current. The collector then floats at approximately the same potential as a standard Langmuir probe. Once the simulated collector is recessed beyond 1 mm in the 250 mT case, it reaches a peak potential approximately 1 V lower than the plasma potential. This plateau extends up to depths

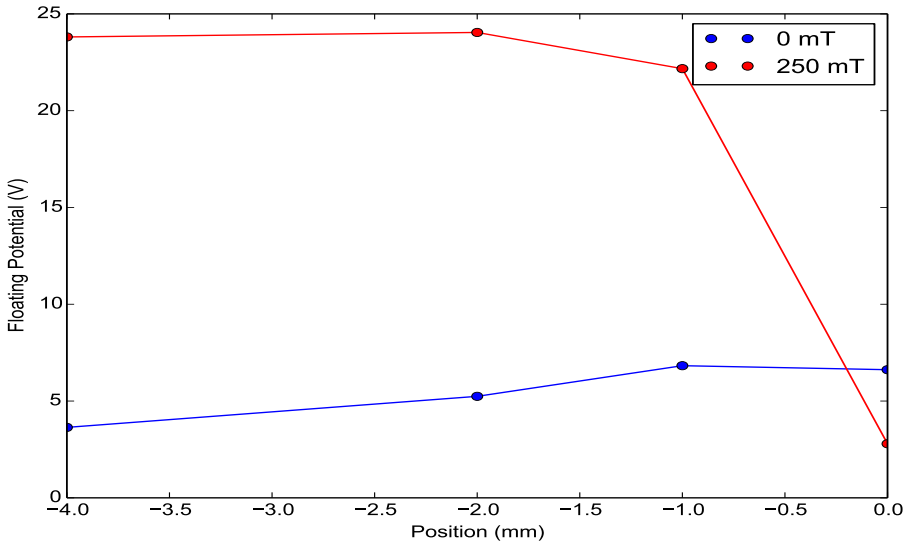

FIGURE 6.10: The results of PIC simulations of the BPP with the 2 mm, flat collector.

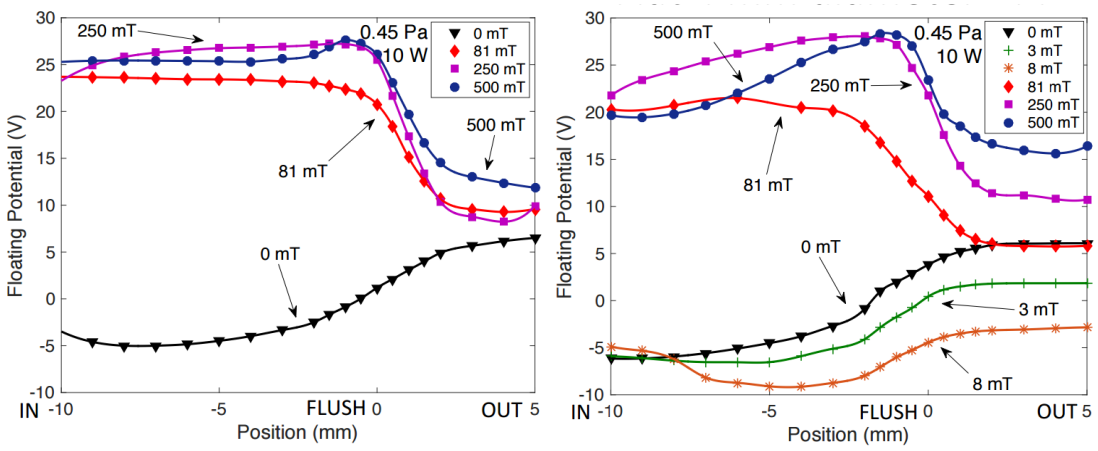

FIGURE 6.11: The floating potential of the two 4 mm BPP collectors as a function of recession depth for different field strengths. On the left - floating potentials of the tapered collector. On the right - floating potentials of the flat collector.

of 4 mm which is a larger region than in the experiments. This suggests there is some mechanism not accounted for in the simulation, possibly ion-neutral collisions. A larger simulation was carried out in the unmagnetised case for a probe recessed by 7 mm and it was found to float at $\approx 4V$. Once recessed inside the tunnel, the collector potential doesn't vary sufficiently with recession depth in experiments or simulations. The magnetic field restricts particle motion, therefore, simulations with a magnetic field take longer to reach a steady state. As a result, the 7 mm run for the 250 mT case could not be completed.

In order to investigate the effects of probe size, the same experiments were carried out for a larger BPP with a collector diameter of 4 mm. The results are presented in figure 6.11.

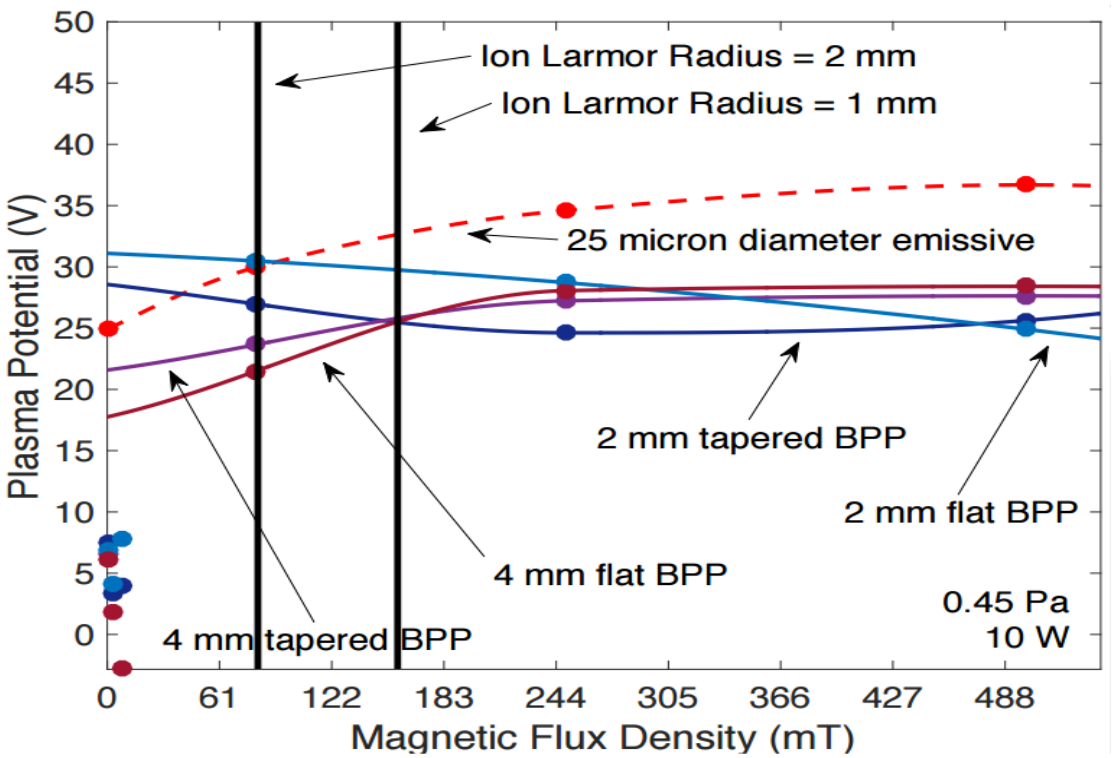

FIGURE 6.12: The peak floating potential of the various BPP collectors and the emissive probe at different magnetic flux densities.

The 4 mm probe exhibits a larger plateau region for the stronger field cases as the ions have more time to travel down the tunnel to the collector before hitting a tunnel wall. This larger plateau effect is especially evident with the tapered collector, suggesting this could be a better design for highly magnetised, low temperature plasmas as the measured plasma potential is less dependent on the recession depth of the collector. The probe exhibits BPP behaviour in the intermediate case of 81 mT but does not reach the same peak potential, suggesting that the probe is only partially screening out the electron current. This suggests the BPP is sensitive to the ratio of λ_D/D_{BPP} as found in [105]. The maximum floating potential reached by each collector for a given field strength is shown in figure 6.12 along with floating potential values of the emissive probe. The 2 mm diameter design seems to be more effective for intermediate field strengths. In terms of the peak potential reached, there is no significant difference between the various designs of the collector, the peak value does not seem to depend on shape or size of collector for the sizes investigated here.

The emissive probe values do not appear to agree well with the BPP values, the BPPs are consistently found to float at lower potentials, varying by more than 1 T_e. Lower floating potentials may be expected as collisions between ions and neutral particles in the BPP tunnel will hinder the collection of ions. However, with increasing field strength, the effects of collisions should be reduced, yet the peak floating potential reached by the BPP remains constant. This observation suggests collisions are not causing the BPP to float below the emissive probe potential. The relative position of the two probes

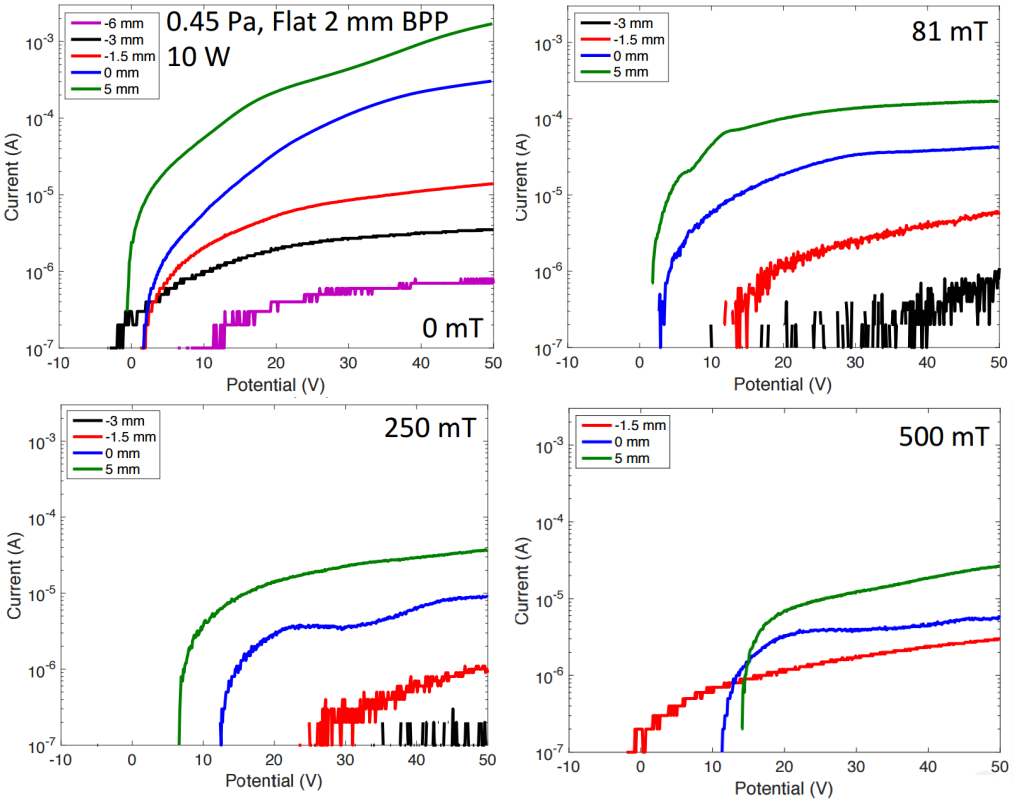

FIGURE 6.13: The current reaching the 2 mm collector at different recession depths for various magnetic field strengths.

could play a role in the potential measured. The two probes were on different field lines so the probes would have sampled different plasma flux tubes. These may have been at different potentials. Scans of the plasma potential at different positions inside the apparatus are required to determine the impact that probe position has on the readings.

I-V curves were created by sweeping the potential applied to the BPP collector. As shown in figure 6.13, the current to the collector for both electrons and ions was seen to decrease as the collector was recessed further into the tunnel, as more particles are absorbed by the tunnel wall before they can reach the collector. Increasing the field strength, significantly reduces the current reaching the recessed collector as the reduced Larmor radius of the particles inhibits transport down the tunnel.

In high temperature fusion plasmas, the I-V curves can be used to obtain α_{BPP} values by measuring the ratio of the electron saturation current to the ion saturation current. In these plasmas, non-saturation of the current for both species is observed but the increase is linear with applied bias voltage and so the saturation current at the floating potential can be measured by a linear fit to the data. As detailed in Chapter 5, each current is linearly extrapolated to the floating potential of the BPP, the ratio of the electron and ion currents at this potential is assumed to be α_{BPP}. Non-saturation of the currents was also observed for the BPP collector in these low temperature experiments, as can be seen in figure 6.14. The increase in current with increasing bias voltage is highly non-linear, this was also observed in other low temperature plasma experiments

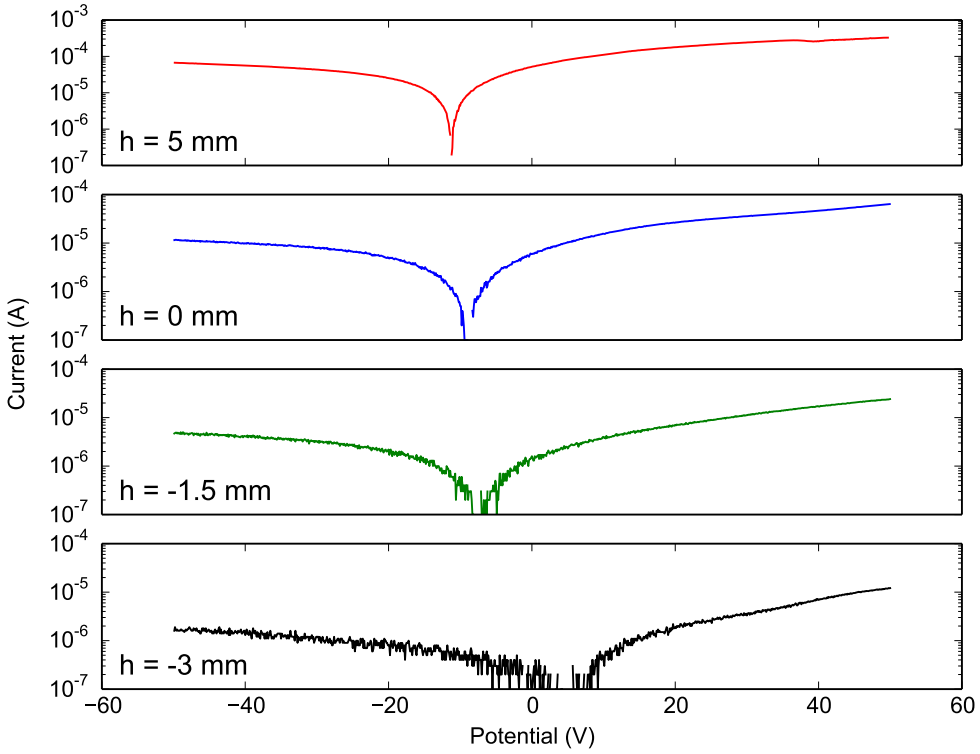

FIGURE 6.14: I-V curves for the 2 mm collector at different recession depths with a magnetic field strength of 81 mT. Absolute values for the current have been taken.

with the BPP [107]. A BPP partially shields the collector from electrons, reducing the ratio of the saturation currents. With these I-V curves, a reduction in the ratio of the saturation currents is not evident, despite a clear change in the measured floating potential of the BPP at different recession depths. Due to the non-linear relationship, a complete understanding of the non-saturation is required in order to determine the true ratio of the saturation currents. The currents cannot be extrapolated back to the floating potential of the BPP to obtain a ratio without understanding the dependence of the collected current on the bias voltage applied to the probe. It is currently not possible to determine the influence of tunnel diameter on α_{BPP} for a BPP in a low temperature plasma.

6.5 Conclusions

A discrepancy has been observed in the potential measured by the emissive probe compared to that of all four BPPs. The BPPs are found to float at a peak potential which is lower than the emissive probe floating potential, with the difference in potential exceeding 1 T_e. An emissive probe is known to float $\approx 1.5T_e$ V below the plasma potential. The BPPs would then be floating at a potential $\approx 2.5T_e$ V less than the plasma potential. It is inconclusive if the BPP is truly measuring a potential significantly below the

plasma potential or if the difference in position of the probes results in them sampling flux tubes at different plasma potentials. In the experiments with a strong magnetic field, both species are magnetised, the BPPs are then operating in a different regime to [105] in which the large BPPs were unable to effectively screen out the electron current and hence floated significantly below the plasma potential. If collisions in the BPP tunnel are responsible for the reduction of the floating potential, it would be expected that their effect would be less significant for higher magnetic field strengths, causing the floating potential of the collector to rise. No rise in the peak potential between the 250 and 500 mT cases was observed, suggesting collisions are not having this effect on the floating potential. In experiments, a glow around the insulating tube of the BPP was observed, this may have perturbed the local plasma potential. This seems to be an inherent side effect of introducing insulating objects into a magnetised plasma and may be more significant for low density plasmas, as a larger λ_D increases the spatial scale of the perturbation. Simulations of the BPP, without collisions, suggest the BPP collector should float at $\approx$ 1 V less than the plasma potential. From [28], the mean free path (λ_i) for charge exchange collisions between an argon ion and atom is given by $\lambda_i = \frac{1}{330p}$ cm, where p is the pressure in Torr. At a pressure of 0.45 Pa, $\lambda_i \approx 9$ mm, the ions should be able to reach the collector without undergoing collisions. If collisions are not affecting the floating potential of the probe in experiments, this could suggest probe position is the cause of this discrepancy. Horizontal and vertical scans of the apparatus are required, obtaining floating potential measurements, ideally for both probes, to investigate the effects of probe position.

In terms of the maximum potential reached by each BPP collector, no significant difference between the collector shapes or diameters was observed. Even if α_{BPP} varies for each collector, the electron temperature is low and therefore differences in the floating potential values reached will be small. The current collected by the collectors was found to increase non-linearly with applied voltage, without understanding this non-linear behaviour it is not possible to estimate α_{BPP}. The differences in α_{BPP} obtained in the simulations from chapter 5 for a 3.2 mm collector and a 4 mm collector were slight, $\alpha_{BPP} = 1.1$ and $\alpha_{BPP} = 1.04$ respectively. With an estimated electron temperature of 3 eV in these experiments, a slight variation of less than 0.18 V would be expected in the peak potential reached by the different collectors. This is less than one percent of the measured voltages and cannot be determined from the results. It would be desirable to complete this comparison of different collector shapes and sizes in a fusion plasma where the non-saturation of the I-V curves is linear and so α_{BPP} values can be estimated. Variations of α_{BPP} will also be more evident from floating potential measurements in these plasmas due to the high electron temperatures.

The 4 mm collectors were found to have a larger plateau region for the 250 mT and 500 mT cases compared to the 2 mm collectors. This is expected from the transport mechanism, the larger the diameter of the probe tunnel, the more time an ion has to reach a collector before its parallel motion along the field brings it to the tunnel

wall. In practical applications of the BPP, a collector that is in a fixed position is desirable to simplify the implementation of the diagnostic. For strong fields $\geq$ 250 mT, a 4 mm diameter collector recessed by 3-4 mm would be suitable for plasma potential measurements. The 4 mm tapered probe observed a larger plateau region for the highly magnetised cases suggesting this design would be preferable over the flat collector so that the floating potentials are less sensitive to recession depth. The tapered collector protrudes outwards to a tip. The electric field at the tip will be larger than that for a flat probe, so the tapered collector is able to draw current to it from further up the tunnel. This may provide an explanation for the larger plateau region observed compared to the flat collector. For intermediate field strengths such as the 81 mT case, the 4 mm probe was found to not effectively screen out the electron current. The 2 mm probe was more effective at this field strength and the floating potential was not very sensitive to recession depth. A 2 mm diameter collector recessed by at least 3 mm would be suitable for plasma potential measurements in low temperature plasmas with field strengths on the order of 100 mT. The tapered design may be preferable to the flat collector as the flat design showed enhanced variation of the potential at a recession depth of 9 mm compared to the tapered collector results.

In the two strong field cases (250 and 500 mT), where the field strengths are comparable to that of a tokamak, the BPP exhibited behaviour similar to that seen in fusion plasmas. The diameter did not seem to affect the probe measurements suggesting that a diameter of 2 mm is sufficient to allow ions to reach the collector. The main difference in the behaviour of the probe in these two plasmas, is a high sensitivity to recession depth in low temperature plasmas. This is likely due to the lower temperature of the ions, leading to a smaller ρ_i which restricts the depth ions can penetrate into the tunnel. Collisions will further restrict the maximum depth an ion can reach. At the intermediate field strength of 81 mT, the probe diameter started to become important. The 4 mm probe was found to ineffectively screen the electron current to the collector, suggesting the ratio of λ_D/D_{BPP} should be maximised at intermediate field strengths, as previously reported in [105]. Measurements made with the BPP under a pressure of 9.6 Pa provide further evidence that the probe can only operate as a BPP once the threshold 10 mT/Pa has been met. As the pressure increases, so must the magnetic field strength for successful plasma potential measurements. The emissive probe would therefore be a better diagnostic for high pressure, weakly magnetised plasmas. Although, the BPP proved to be a more resilient diagnostic as the emissive probe wire melted on a few occasions.

Chapter 7

Conclusions and Future Work

7.1 Conclusions

Reliable measurements of the plasma parameters at the boundaries of tokamaks are vital for understanding plasma transport in the edge region as well as to assess the potential for damage to occur to the material surfaces. Accurate measurements also provide insight into the physics of the sheath in magnetised plasmas. Measurements of T_e and n_e are crucial to determining the heat and power impinging upon the divertor tiles. Fast measurements of the plasma potential, on the order of microsecond time resolution are required to track the evolution of the potential during filament events.

Flush mounted Langmuir probes are a key diagnostic to make measurements of the plasma parameters at the plasma-surface boundary. Their use in tokamaks is widespread and they will be increasingly relied upon as tokamaks reach higher powers, leading to divertor conditions in which protruding probes will not survive. Due to the grazing angles of incidence between the magnetic field and the divertor surface, flush-mounted probes (FMP) exhibit behaviour that deviates from standard Langmuir probe theory. For low field line angles (θ), the projected area of the probe can become comparable to the area of the probe sheath, the collection area of the probe is then a function of the applied voltage to the probe and as a result the ion current does not saturate as the probe bias is increased. The FMPs on MAST were studied using particle-in-cell (PIC) simulations. The simulations found the presence of a gap, of length g, in between a divertor tile and a FMP, increases the effective collection area of the probe by an amount $g \sin\theta$. For MAST this increases the overall collection area for a FMP by 20%.

A finite electron Larmor orbit effect has been observed in two-dimensional simulations of FMPs for oblique angles of incidence between the magnetic field and the probe surface. Electrons were observed to penetrate into the sheath, reaching a distance $1\rho_e$ from the probe surface before undergoing a reflection away from the surface, due to the negative probe potential. At this distance, the motion of electrons around field lines allows them to reach the probe surface without the parallel energy required to overcome the negative probe potential. Measuring the electron temperature from the gradient of a log plot of the electron current against probe bias voltage results in a measurement

of the electron temperature that is higher than that specified by the source function. The effect was explored further in one dimensional simulations. It was found the ratio $T_e^{measured}/T_e^{source}$ depended on the ratio of the Debye length to the electron Larmor radius. Higher densities increase the extent of the overestimation of the electron temperature. Stronger magnetic fields reduce the overestimation. This effect was observed in simulations which enable the electron current reaching the probe to be completely isolated from the ion current. Extracting just the electron current from experimental data is complicated by the non-saturation of the ion current.

The ball-pen probe (BPP) was initially designed to make direct measurements of the plasma potential from the floating potential of the probe, without having to sweep the voltage across the probe. Floating measurements can be made at sufficient speed to resolve the potential fluctuations that occur during filament events. However, previous experiments indicated that the BPP floated at a potential offset from the plasma potential by the equation

$$V_{LP} = \Phi - T_e \alpha_{BPP} \tag{7.1}$$

where $\alpha_{BPP} = 0.6 \pm 0.3$. Three-dimensional PIC simulations of the BPP were carried out. Simulations verified the capability of the probe to partially screen the electron current to the collector. Simulations confirmed the floating potential was well described by equation 7.1 but a value of $\alpha_{BPP} = 1.04$, for the simulated probe was obtained, which is above the range of values observed in experiments. Secondary electron emission that can occur when an ion is incident on the probe collector, was not included in the simulations. The current to the probe from an emitted electron is equivalent to a collected ion so this effect would enhance the observed ion current and lower α_{BPP}. The floating potential of the BPP is sensitive to the electron temperature and so will deviate significantly from the plasma potential for large T_e values. However, simulations have verified that fast measurements of T_e can be obtained from floating potentials of both a Langmuir probe and a BPP. This measurement of T_e can be combined with the floating potential of the BPP to obtain plasma potential measurements with high temporal resolution. The transport mechanism of charged particles down the tunnel of the BPP was investigated. Electrons were found to undergo multiple reflections off the sheath in front of the probe tunnel wall, whilst being driven down the tunnel by E x B drift motion. Ions were able to reach the collector directly due to their larger Larmor orbits, assisted by E x B drifts. Ions perpendicular speed must exceed their parallel speed for them to make it to the collector before being absorbed by the tunnel wall.

The BPP was implemented in a low temperature, low density, strongly magnetised plasma ($T_e \approx 3$ eV, $n_e \approx 10^{15}$ m^{-3} and B ranged from 0-500 mT). This allowed the capabilities of the BPP to be tested in a new regime. A discrepancy was observed as the floating potential of the BPP was consistently lower than that of an emissive probe operated in the limit of large emission. Causes of this discrepancy are inconclusive, the probes sampled different flux tubes which may have been at different potentials. Scans of the floating potential, obtained with at least one of the probes, are necessary in order

to investigate the effect of probe position on inferred plasma potential. The effects of the collector diameter were investigated by obtaining floating potentials for a 2 mm and 4 mm collector. For strong magnetic fields, relevant to fusion plasmas, the BPP results were insensitive to probe diameter, suggesting a 2 mm probe is sufficiently large to allow ions to reach the collector. Due to the low ion temperatures in this plasma, the floating potential of the probe was sensitive to probe recession depth at these field strengths. The larger collector diameter and tapered designs were less sensitive to the recession depth. At intermediate field strengths, the probe diameter did have an effect. The larger probe was unable to effectively screen out the electron current. The 2 mm probe was more suited to the low temperature plasma for the 81 mT case.

7.2 Future Work

The PIC simulations for magnetised plasma could be improved generally by removing the Larmor buffer region from the simulation domain. This would reduce the number of grid cells in the domain. Simulations will therefore take less time to complete. In order to do this, an improvement to the particle deletion algorithm is necessary. The algorithm should selectively remove particles from the simulation based on their parallel velocity. Only particles with parallel velocity directed out of the simulation domain should be deleted.

The simulations of Chapter 4 identified a source of error in the temperature measurements made by a flush-mounted Langmuir probe. A model based on first principles, that can take into account the additional electrons reaching the probe due to finite electron Larmor orbit effects is required. By expanding the simulations to three-dimensions, the influence of E x B drifts on the finite Larmor effect could be investigated. The development of a three-dimensional model for a FMP in VSim is simple, it can easily be adapted from the BPP simulations. However, the high densities and low temperatures in the divertor region, enhances the number of grid cells required. These runs would be possible with sufficient number of cores on a super computer (≈ 256 or more on the N8 HPC).

The simulations of Chapter 5 could be expanded to include secondary electron emission (SEE) from the probe surface. This emission could reduce the values of α_{BPP} obtained in simulations. VSim has the capability to include SEE, so incorporating this into the simulation model should be straightforward. Simulations with a conical collector could also be carried out to determine if this shape is more effective at reducing the ratio of the saturation currents. This work would benefit from a thorough experimental analysis for BPPs, of different size and shape, in a fusion plasma, measuring both the floating potential of the probe and the value of α_{BPP}. A BPP is to be installed on MAST-Upgrade, so this work could be carried out once operations resume in 2018.

Simulations of BPPs in low temperature plasmas could be used to understand the non-linear increase in saturation current with applied bias voltage, as observed in the

experiments of Chapter 6. Understanding this behaviour would allow α_{BPP} values to be extracted. In order for simulations to better represent the experiments, the inclusion of collisions between charged and neutral particles is necessary. This is not currently possible in VSim. Performing vertical and horizontal scans of the apparatus with an emissive probe is on going work. This will determine how the plasma potential depends on the position of the probe.

Bibliography

[1] I. E. Authority. *World energy outlook 2016*. 2016. URL https://www.iae.org.

[2] BP. *Bp statistical review of world energy 2016*. 2016. URL https://www.bp.com/content/dam/bp/pdf/energy-economics/statistical-review-2016/bp-statistical-review-of-world-energy-2016-full-report.pdf.

[3] V. Fthenakis and H. Kim. *Greenhouse-gas emissions from solar electric- and nuclear power: A life-cycle study. Energy Policy*, 35(4):2549–2557, 2007. URL http://www.sciencedirect.com/science/article/pii/S0301421506002758.

[4] O. NEA. *Uranium: Resources, production and demand*. 2014. URL https://www.oecd-nea.org/ndd/pubs/2014/7209-uranium-2014.pdf.

[5] B. W. Brook, A. Alonso, D. A. Meneley, J. Misak, et al. *Why nuclear energy is sustainable and has to be part of the energy mix. Sustainable Materials and Technologies*, 12:8 – 16, 2014. URL http://www.sciencedirect.com/science/article/pii/S2214993714000050.

[6] J. Ongena and G. Van Oost. *Energy for future centuries - will fusion be an inexhaustible, safe and clean energy source? Fusion Science and Technology*, 45(2T):3–14, 2004.

[7] M. Keilhacker, A. Gibson, C. Gormezano, P. Lomas, et al. *High fusion performance from deuterium-tritium plasmas in jet. Nuclear Fusion*, 39(2):209, 1999. URL http://stacks.iop.org/0029-5515/39/i=2/a=306.

[8] N. Walkden. *Properties of intermittent transport in the mega ampere spherical tokamak. PhD Thesis*, University of York(2014).

[9] F. Wagner, G. Becker, K. Behringer, D. Campbell, et al. *Regime of improved confinement and high beta in neutral-beam-heated divertor discharges of the asdex tokamak. Phys. Rev. Lett.*, 49:1408–1412, 1982. URL http://link.aps.org/nodoi/10.1103/PhysRevLett.49.1408.

[10] P. Stangeby and G. McCracken. *Plasma boundary phenomena in tokamaks. Nuclear Fusion*, 30(7):1225, 1990. URL http://stacks.iop.org/0029-5515/30/i=7/a=005.

[11] J. Knaster, A. Moeslang, and T. Muroga. *Materials research for fusion. Nat Phys*, 12(5):424–434, 2016. URL `http://dx.nodoi.org/10.1038/nphys3735`. Review.

[12] G. Fishpool, J. Canik, G. Cunningham, J. Harrison, et al. *MAST-upgrade divertor facility and assessing performance of long-legged divertors. Journal of Nuclear Materials*, 438:S356–S359, 2013.

[13] E. Havlkov, W. Fundamenski, M. Wischmeier, G. Fishpool, and A. W. Morris. *Investigation of conventional and super-x divertor configurations of mast upgrade using scrape-off layer plasma simulation. Plasma Physics and Controlled Fusion*, 56(7):075008, 2014. URL `http://stacks.iop.org/0741-3335/56/i=7/a=075008`.

[14] F. Chen. *Introduction to Plasma Physics and Controlled Fusion.* Springer International Publishing, 2015. ISBN 9783319223094. URL `https://books.google.co.uk/books?id=mFg-CwAAQBAJ`.

[15] G. F. Matthews. *Tokamak plasma diagnosis by electrical probes. Plasma Physics and Controlled Fusion*, 36(10):1595, 1994. URL `http://stacks.iop.org/0741-3335/36/i=10/a=002`.

[16] C. Lasnier, S. Allen, J. Boedo, and M. Groth. *Chapter 10: First wall and operational diagnostics. Fusion Science and Technology*, 53(2):640, 2008.

[17] I. Langmuir. *Positive ion currents from the positive column of mercury arcs. Science*, 58(1502):290–291, 1923.

[18] H. M. Mott-Smith and I. Langmuir. *The theory of collectors in gaseous discharges. Phys. Rev.*, 28:727–763, 1926. URL `http://link.aps.org/nodoi/10.1103/PhysRev.28.727`.

[19] V. Demidov, S. V. Ratynskaia, and K. Rypdal. *Electric probes for plasmas: The link between theory and instrument. Review of scientific instruments*, 73(10):3409–3439, 2002.

[20] E. V. Shun'ko. *Langmuir Probe in Theory and Practise.* Universal Publishers, 1 edition, 2009.

[21] P. C. Stangeby. *A tutorial on some basic aspects of divertor physics. Plasma Physics and Controlled Fusion*, 42(12B):B271, 2000. URL `http://stacks.iop.org/0741-3335/42/i=12B/a=321`.

[22] K.-U. Riemann. *The bohm criterion and sheath formation. Journal of Physics D: Applied Physics*, 24(4):493, 1991.

[23] I. H. Hutchinson. *Principles of plasma diagnostics. Plasma Physics and Controlled Fusion*, 44(12):2603, 2002.

[24] D. Bohm. *The characteristics of electrical discharges in magnetic fields. A Guthry and R K Wakerling ch 3, pg 77.*

[25] P. C. Stangeby. *The Plasma Boundary of Magnetic Fusion Devices.* IoP, 2000.

[26] R. B. Lobbia and A. D. Gallimore. *Temporal limits of a rapidly swept langmuir probe. Physics of Plasmas*, 17(7):073502, 2010. URL `http://scitation.aip.org/content/aip/journal/pop/17/7/10.1063/1.3449588`.

[27] R. D. Monk. *Langmuir probe measurements in the divertor plasma of the jet tokamak.* 1996.

[28] M. A. Lieberman and A. J. Lichtenberg. *Principles of plasma discharges and materials processing.* John Wiley & Sons, 2005.

[29] R. Chodura. *Plasma wall transition in an oblique magnetic field. Physics of Fluids*, 25(9), 1982.

[30] S. Riyopoulos. *Unstable particle drift across a magnetic field caused by oblique electric field gradients. Physics of Plasmas*, 3(12), 1996.

[31] P. Stangeby. *The chodura sheath for angles of a few degrees between the magnetic field and the surface of divertor targets and limiters. Nuclear Fusion*, 52(8):083012, 2012. URL `http://stacks.iop.org/0029-5515/52/i=8/a=083012`.

[32] A. Kuang, D. Brunner, B. LaBombard, R. Leccacorvi, and R. Vieira. *Design and operation of a high-heat flux, flush-mounted rail langmuir probe array on alcator c-mod. Nuclear Materials and Energy*, pages –, 2016. URL `http://www.sciencedirect.com/science/article/pii/S2352179116300916`.

[33] D. Coulette and G. Manfredi. *Kinetic simulations of the chodura and debye sheaths for magnetic fields with grazing incidence. Plasma Physics and Controlled Fusion*, 58(2):025008, 2016. URL `http://stacks.iop.org/0741-3335/58/i=2/a=025008`.

[34] P. C. Stangeby. *Effect of bias on trapping probes and bolometers for tokamak edge diagnosis. Journal of Physics D: Applied Physics*, 15(6):1007, 1982. URL `http://stacks.iop.org/0022-3727/15/i=6/a=011`.

[35] McGraw-Hill. *The characteristics of electrical discharges in magnetic fields. National nuclear energy series*, 5, 1949.

[36] J. A. Tagle, P. C. Stangeby, and S. K. Erents. *Errors in measuring electron temperatures using a single langmuir probe in a magnetic field. Plasma Physics and Controlled Fusion*, 29(3):297, 1987. URL `http://stacks.iop.org/0741-3335/29/i=3/a=001`.

[37] P. C. Stangeby. *Determination of t_e from a langmuir probe in a magnetic field by directly measuring the probe's sheath drop using a pin-plate probe. Plasma Physics and Controlled Fusion*, 37(11):1337, 1995. URL `http://stacks.iop.org/0741-3335/37/i=11/a=011`.

[38] R. A. Pitts and P. C. Stangeby. *Experimental tests of langmuir probe theory for strong magnetic fields. Plasma Physics and Controlled Fusion*, 32(13):1237, 1990. URL `http://stacks.iop.org/0741-3335/32/i=13/a=004`.

[39] I. G. Brown, A. B. Compher, and W. B. Kunkel. *Response of a langmuir probe in a strong magnetic field. Physics of Fluids (1958-1988)*, 14(7), 1971.

[40] A. Carlson, V. Rohde, and M. Weinlich. *The separation of angle and size effects on langmuir characteristics. Journal of Nuclear Materials*, 241:722 – 727, 1997. URL `http://www.sciencedirect.com/science/article/pii/S0022311597801298`.

[41] M. Dimitrova, T. K. Popov, P. Ivanova, E. Vasileva, et al. *Evaluation of the scrape-off-layer plasma parameters by a horizontal reciprocating langmuir probe in the compass tokamak. Journal of Physics: Conference Series*, 514(1):012049, 2014. URL `http://stacks.iop.org/1742-6596/514/i=1/a=012049`.

[42] T. K. Popov, P. Ivanova, J. Stckel, and R. Dejarnac. *Electron energy distribution function, plasma potential and electron density measured by langmuir probe in tokamak edge plasma. Plasma Physics and Controlled Fusion*, 51(6):065014, 2009. URL `http://stacks.iop.org/0741-3335/51/i=6/a=065014`.

[43] M. Jaworski, M. Bell, T. Gray, R. Kaita, et al. *Modification of the electron energy distribution function during lithium experiments on the national spherical torus experiment. Fusion Engineering and Design*, 87(10):1711 – 1718, 2012. URL `http://www.sciencedirect.com/science/article/pii/S0920379611006302`. The 2nd International Symposium of Lithium Application for Fusion Devices.

[44] S. Elmore, S. Allan, A. Kirk, A. Thornton, et al. *Scrape-off layer ion temperature measurements at the divertor target in mast by retarding field energy analyser. Journal of Nuclear Materials*, 438:S1212–S1215, 2013.

[45] G. V. Oost. *Advanced probe edge diagnostics for fusion devices. Journal of Physics: Conference Series*, 666(1):012001, 2016. URL `http://stacks.iop.org/1742-6596/666/i=1/a=012001`.

[46] J. P. Gunn, R. Schrittwieser, P. Balan, C. Ioni, et al. *Tunnel probes for measurements of the electron and ion temperature in fusion plasmas. Review of Scientific Instruments*, 75(10):4328–4330, 2004. URL `http://dx.nodoi.org/10.1063/1.1787581`.

[47] P. Balan, R. Schrittwieser, J. Admek, O. Baina, et al. *Measurements of the parallel and perpendicular ion temperatures by means of an ion-sensitive segmented tunnel probe. Contributions to Plasma Physics*, 44(7-8):683–688, 2004. URL `http://dx.nodoi.org/10.1002/ctpp.200410101`.

[48] I. Katsumata. *A review of ion sensitive probes. Contributions to Plasma Physics*, 36(S1):73–79, 1996. URL `http://dx.nodoi.org/10.1002/ctpp.19960360112`.

[49] J. Adámek, J. Stöckel, M. Hron, J. Ryszawy, et al. *A novel approach to direct measurement of the plasma potential. Czechoslovak Journal of Physics*, 54(3):C95–C99. URL `http://dx.nodoi.org/10.1007/BF03166386`.

[50] J. M. Dawson. *Thermal relaxation in a onespecies, onedimensional plasma. Physics of Fluids*, 7(3), 1964.

[51] H. C. Kim, F. Iza, S. S. Yang, M. Radmilovi-Radjenovi, and J. K. Lee. *Particle and fluid simulations of low-temperature plasma discharges: benchmarks and kinetic effects. Journal of Physics D: Applied Physics*, 38(19):R283, 2005. URL `http://stacks.iop.org/0022-3727/38/i=19/a=R01`.

[52] E. Westerhof and J. Pratt. *Closure of the single fluid magnetohydrodynamic equations in presence of electron cyclotron current drive. Physics of Plasmas*, 21(10):102516, 2014.

[53] P. Sturrock. *Plasma Physics: An Introduction to the Theory of Astrophysical, Geophysical and Laboratory Plasmas*. Stanford-Cambridge program. Cambridge University Press, 1994. ISBN 9780521448109. URL `https://books.google.co.uk/books?id=jsMFNi2xQzkC`.

[54] V. Hrubỳ and R. Hrach. *Selected techniques for langmuir probe modelling in low-temperature plasmas*. In *WDS 2010-Proceedings of Contributed Papers. Part II-Physics of Plasmas and Ionized Media (ISBN 978-80-7378-140-8) MATFYZ-PRESS, Prague, 2010., p. 38-41*, volume 1, pages 38–41. 2010.

[55] J. Krek, N. Jeli, and J. Duhovnik. *Particle-in-cell (pic) simulations on plasmasheath boundary in collision-free plasmas with warm-ion sources. Nuclear Engineering and Design*, 241(4):1261 – 1266, 2011. URL `http://www.sciencedirect.com/science/article/pii/S002954931000258X`. International Conference on Nuclear Energy for New Europe 2009.

[56] D. Nunn. *A novel technique for the numerical simulation of hot collision-free plasma; vlasov hybrid simulation. J. Comput. Phys.*, 108(1):180–196, 1993. URL `http://dx.nodoi.org/10.1006/jcph.1993.1173`.

[57] G. Snchez-Arriaga and D. Pastor-Moreno. *Direct vlasov simulations of electron-attracting cylindrical langmuir probes in flowing plasmas. Physics of Plasmas*,

21(7):073504, 2014. URL http://scitation.aip.org/content/aip/journal/pop/21/7/10.1063/1.4889732.

[58] J. P. Boris. *Relativistic plasma simulation-optimization of a hybrid code,. Proceedings of the Fourth Conference on Numerical Simulations of Plasmas*, 20, 1970.

[59] H. Qin, S. Zhang, J. Xiao, J. Liu, et al. *Why is boris algorithm so good? Physics of Plasmas*, 20(8):084503, 2013. URL http://scitation.aip.org/content/aip/journal/pop/20/8/10.1063/1.4818428.

[60] C. K. Birdsall and A. B. Langdon. *Plasma physics via computer simulation*. Series in plasma physics. Taylor & Francis, New York, 2005. ISBN 0-7503-1025-1. URL http://opac.inria.fr/record=b1121477. Originally published: New York ; London : McGraw-Hill, 1985.

[61] J. Harrison. *Characterisation of detached plasmas on the mast tokamak. PhD Thesis*, 2010.

[62] G. Lapenta. *Particle In Cell Methods With Application to Simulations in Space Weather*. Cambridge University Press, New York, NY, USA, 1992. ISBN 0-521-43108-5.

[63] G. Emmert. *Electric sheath and presheath in a collisionless, finite ion temperature plasma. Physics of Fluids*, 23(803), 1980.

[64] M. Komm. *Studies of tokamak edge plasma and its interaction with the first wall. PhD Thesis*, 2007.

[65] J. Wesson and J. Connor. *Tokamaks / John Wesson ; with contributions from J.W. Connor et al.* Clarendon Press Oxford ; New York, 1987. ISBN 0198563280. URL http://www.loc.gov/catdir/enhancements/fy0635/86012725-t.html.

[66] J. P. Gunn. *The influence of magnetization strength on the sheath: Implications for flush-mounted probes. Physics of Plasmas*, 4(12):4435–4446, 1997. URL http://scitation.aip.org/content/aip/journal/pop/4/12/10.1063/1.872608.

[67] C. D. Child. *Discharge from hot cao. Phys. Rev. (Series I)*, 32:492–511, 1911. URL https://link.aps.org/nodoi/10.1103/PhysRevSeriesI.32.492.

[68] I. Langmuir. *The effect of space charge and residual gases on thermionic currents in high vacuum. Phys. Rev.*, 2:450–486, 1913. URL https://link.aps.org/nodoi/10.1103/PhysRev.2.450.

[69] J. P. Gunn, C. Boucher, B. L. Stansfield, and S. Savoie. *Flushmounted probes in the divertor plates of tokamak de varennes. Review of Scientific Instruments*, 66(1):154–159, 1995. URL http://scitation.aip.org/content/aip/journal/rsi/66/1/10.1063/1.1145249.

[70] G. F. Matthews, S. J. Fielding, G. M. McCracken, C. S. Pitcher, et al. *Investigation of the fluxes to a surface at grazing angles of incidence in the tokamak boundary. Plasma Physics and Controlled Fusion*, 32(14):1301, 2004. URL `http://stacks.iop.org/0741-3335/32/i=14/a=004`.

[71] J. Myra, D. D'Ippolito, and M. Gerver. *Faraday screen sheaths and impurity production during ion cyclotron heating. Nuclear Fusion*, 30(5):845, 1990. URL `http://stacks.iop.org/0029-5515/30/i=5/a=004`.

[72] M. Weinlich and A. Carlson. *Flush mounted probes in asdex upgrade - can they be operated as triple probes? Contributions to Plasma Physics*, 36(S1):53–59, 1996. URL `http://dx.nodoi.org/10.1002/ctpp.19960360109`.

[73] A. Bergmann. *Two-dimensional particle simulation of Langmuir probe sheaths with oblique magnetic field. Physics of Plasmas*, 1:3598–3606, 1994.

[74] M. Weinlich and A. Carlson. *Flush mounted langmuir probes in an oblique magnetic field. Physics of Plasmas*, 4(6):2151–2160, 1997. URL `http://dx.nodoi.org/10.1063/1.872379`.

[75] J. A. Tagle, P. C. Stangeby, and S. K. Erents. *Errors in measuring electron temperatures using a single langmuir probe in a magnetic field. Plasma Physics and Controlled Fusion*, 29(3):297, 1987. URL `http://stacks.iop.org/0741-3335/29/i=3/a=001`.

[76] G. F. Matthews. *Tokamak plasma diagnosis by electrical probes. Plasma Physics Controlled Fusion*, 36(10):1595, 1994. URL `http://stacks.iop.org/0741-3335/36/i=10/a=002`.

[77] E. Havlkov, J. Harrison, B. Lipschultz, G. Fishpool, et al. *Solps analysis of the mast-u divertor with the effect of heating power and pumping on the access to detachment in the super-x configuration. Plasma Physics and Controlled Fusion*, 57(11):115001, 2015. URL `http://stacks.iop.org/0741-3335/57/i=11/a=115001`.

[78] G. Van Rooij, V. Veremiyenko, W. Goedheer, B. De Groot, et al. *Extreme hydrogen plasma densities achieved in a linear plasma generator. Applied physics letters*, 90(12):121501, 2007.

[79] B. LaBombard, J. Goetz, C. Kurz, D. Jablonski, et al. *Scaling and transport analysis of divertor conditions on the alcator cmod tokamak. Physics of Plasmas*, 2(6):2242–2248, 1995. URL `http://dx.nodoi.org/10.1063/1.871248`.

[80] S. Murphy-Sugrue, J. Harrison, N. R. Walkden, P. Bryant, and J. W. Bradley. *Improved understanding of the ball-pen probe through particle-in-cell simulations. Plasma Physics and Controlled Fusion*, 59(5):055007, 2017. URL `http://stacks.iop.org/0741-3335/59/i=5/a=055007`.

[81] P. Stangeby and G. McCracken. *Plasma boundary phenomena in tokamaks. Nuclear Fusion*, 30(7):1225, 1990. URL http://stacks.iop.org/0029-5515/30/i=7/a=005.

[82] J. Adámek, V. Rohde, H. Müller, A. Herrmann, et al. *Direct measurements of the plasma potential in ELMy h-mode plasma with ball-pen probes on ASDEX upgrade tokamak. J. Nucl. Mater.*, 390 391:1114 – 1117, (2009). URL http://www.sciencedirect.com/science/article/pii/S0022311509003110.

[83] D. A. D'Ippolito, J. R. Myra, and S. J. Zweben. *Convective transport by intermittent blob-filaments: Comparison of theory and experiment. Physics of Plasmas*, 18(6):060501, 2011. URL http://scitation.aip.org/content/aip/journal/pop/18/6/10.1063/1.3594609.

[84] F. Militello, P. Tamain, W. Fundamenski, A. Kirk, et al. *Experimental and numerical characterization of the turbulence in the scrape-off layer of mast. Plasma Physics and Controlled Fusion*, 55(2):025005, 2013. URL http://stacks.iop.org/0741-3335/55/i=2/a=025005.

[85] R. Schrittwieser, J. Adámek, P. Balan, M. Hron, et al. *Measurements with an emissive probe in the castor tokamak. Plasma Physics Contr Fusion*, 44(5):567, 2002. URL http://stacks.iop.org/0741-3335/44/i=5/a=305.

[86] R. Schrittwieser, C. Ionita, P. Balan, R. Gstrein, et al. *Laser-heated emissive plasma probe. Review of scientific instruments*, 79(8):083508, 2008.

[87] K. Kovařík, I. Ďuran, J. Stöckel, J. Brotánková, et al. *U-probe for the compass tokamak.* In *WDS*, volume 11, pages 227–232. 2011.

[88] J. J. Adámek, J. Horacek, V. Rohde, H. Müller, et al. *ELM studies with ball-pen and Langmuir probes on ASDEX Upgrade.* In M. Mateev and E. Benova, editors, *36th European Physical Society Conference on Plasma Physics. Contributed Papers*, volume 33E of *ECA*. European Physical Society, Sofia, 2009. ISBN 2-914771-61-4.

[89] R. Pánek, J. Adámek, M. Aftanas, P. Bílková, et al. *Status of the compass tokamak and characterization of the first h-mode. Plasma Phys Contr Fusion*, 58(1):014015, 2016. URL http://stacks.iop.org/0741-3335/58/i=1/a=014015.

[90] N. R. Walkden, J. Adámek, S. Allan, B. D. Dudson, et al. *Profile measurements in the plasma edge of mega amp spherical tokamak using a ball pen probe. Review of Scientific Instruments*, 86(2):023510, 2015.

[91] J. Adámek, M. Peterka, T. Gyergyek, P. Kudrna, et al. *Application of the ball-pen probe in two low-temperature mag-netised plasma devices and in torsatron tj-k. Contributions to Plasma Physics*, 53(1):39–44, 2013. URL http://dx.nodoi.org/10.1002/ctpp.201310007.

[92] R. Schrittwieser, C. Ionitá, J. Adámek, J. Stöckel, et al. *Direct measurements of the plasma potential by katsumata-type probes. Czechoslovak Journal of Physics*, 56(2):B145–B150, 2006. URL `http://dx.nodoi.org/10.1007/s10582-006-0190-7`.

[93] J. Adámek, C. Ionita, R. Schrittwieser, J. Stöckel, et al. *Direct measurements of the electron temperature by a ball-pen/langmuir probe. 32nd EPS Conference on Plasma Physics Contr Fusion*, 29, 2005.

[94] J. Adamek, H. W. Mller, C. Silva, R. Schrittwieser, et al. *Profile measurements of the electron temperature on the asdex upgrade, compass, and isttok tokamak using thomson scattering, triple, and ball-pen probes. Review of Scientific Instruments*, 87(4):043510, 2016. URL `http://dx.nodoi.org/10.1063/1.4945797`.

[95] J. Adamek, J. Horacek, H. Mller, V. Rohde, et al. *Ball-pen probe measurements in l-mode and h-mode on asdex upgrade. Contributions to Plasma Physics*, 50(9):854–859, 2010. URL `http://dx.nodoi.org/10.1002/ctpp.201010145`.

[96] J. Horacek, J. Adamek, H. Mller, J. Seidl, et al. *Interpretation of fast measurements of plasma potential, temperature and density in sol of asdex upgrade. Nuclear Fusion*, 50(10):105001, 2010. URL `http://stacks.iop.org/0029-5515/50/i=10/a=105001`.

[97] J. Adámek, J. Horacek, J. Seidl, H. W. Müller, et al. *Direct Plasma Potential Measurements by Ball-Pen Probe and Self-Emitting Langmuir Probe on COMPASS and ASDEX Upgrade. Contrib Plasm Phys*, 54(3):279–284, 2014. URL `http://dx.nodoi.org/10.1002/ctpp.201410072`.

[98] J. Adámek, J. Stöckel, I. Ďuran, M. Hron, et al. *Comparative measurements of the plasma potential with the ball-pen and emissive probes on the castor tokamak.* 55(3):235–242. URL `http://dx.nodoi.org/10.1007/s10582-005-0036-8`.

[99] G. Bousselin, J. Cavalier, J.-F. Pautex, S. Heuraux, et al. *Design and validation of the ball-pen probe for measurements in a low-temperature magnetized plasma. Review of Scientific Instruments*, 84(1):013505, 2013.

[100] M. Komm, J. Adamek, Z. Pekarek, and R. Panek. *Particle-in-cell simulations of the ball-pen probe. Contributions to Plasma Physics*, 50(9):814–818, 2010. URL `http://dx.nodoi.org/10.1002/ctpp.201010137`.

[101] M. Komm, J. Adámek, R. Dejarnac, J. P. Gunn, and Z. Pekarek. *Transport of electrons in the tunnel of an ion sensitive probe. Plasma Phys Contr Fusion*, 53(1):015005, 2011. URL `http://stacks.iop.org/0741-3335/53/i=1/a=015005`.

[102] R. Sullivan, R. Ochoukov, and D. Whyte. *Internal physics of the ion-sensitive probe. Journal of Nuclear Materials*, 438:S1253–S1256, 2013.

[103] F. Militello, W. Fundamenski, V. Naulin, and A. H. Nielsen. *Simulations of edge and scrape off layer turbulence in mega ampere spherical tokamak plasmas. Plasma Physics and Controlled Fusion*, 54(9):095011, 2012. URL `http://stacks.iop.org/0741-3335/54/i=9/a=095011`.

[104] J. Adámek, J. Seidl, R. Pánek, M. Komm, et al. *Fast measurements of the electron temperature in divertor region of the compass tokamak using ball-pen probe. 42nd EPS Conference on Plasma Phys*, 39, 2015.

[105] G. Bousselin, J. Cavalier, J. F. Pautex, S. Heuraux, et al. *Design and validation of the ball-pen probe for measurements in a low-temperature magnetized plasma. Review of Scientific Instruments*, 84(1):013505, 2013. URL `http://dx.nodoi.org/10.1063/1.4775491`.

[106] R. Schrittwieser, C. Ionita, J. Adámek, J. Stöckel, et al. *Direct measurements of the plasma potential by katsumata-type probes. Czechoslovak Journal of Physics*, 56(2):B145–B150, 2006. URL `http://dx.nodoi.org/10.1007/s10582-006-0190-7`.

[107] M. Zanka, J. Admek, M. Peterka, P. Kudrna, and M. Tich. *Comparative measurements of plasma potential with ball-pen and langmuir probe in low-temperature magnetized plasma. Physics of Plasmas*, 22(3):033516, 2015. URL `http://dx.nodoi.org/10.1063/1.4916572`.

[108] J. Loureiro and J. Amorim. *Applications of Low-Temperature Plasmas*, pages 413–440. Springer International Publishing, Cham, 2016. ISBN 978-3-319-09253-9. URL `http://dx.nodoi.org/10.1007/978-3-319-09253-9_11`.

[109] H. Ibach. *Solid-State Physics (Advanced Texts in Physics (Paperback))*. Springer, 2013. URL `https://www.amazon.com/Solid-State-Physics-Advanced-Texts-Paperback-ebook/dp/B00DGEQU6U?SubscriptionId=0JYN1NVW651KCA56C102&tag=techkie-20&linkCode=xm2&camp=2025&creative=165953&creativeASIN=B00DGEQU6U`.

[110] Y. P. Raizer and J. E. Allen. *Gas discharge physics*, volume 2. Springer Berlin, 1997.

[111] J. P. Sheehan, Y. Raitses, N. Hershkowitz, I. Kaganovich, and N. J. Fisch. *A comparison of emissive probe techniques for electric potential measurements in a complex plasma. Physics of Plasmas*, 18(7):073501, 2011. URL `http://dx.nodoi.org/10.1063/1.3601354`.

[112] J. R. Smith, N. Hershkowitz, and P. Coakley. *Inflectionpoint method of interpreting emissive probe characteristics. Review of Scientific Instruments*, 50(2):210–218, 1979. URL `http://dx.nodoi.org/10.1063/1.1135789`.

[113] S. Tierno, J. Domenech-Garret, J. Donoso, D. Jennewein, et al. *Emissive langmuir probes in the strong emission regime for the determination of the plasma properties. IEEE Transactions on Plasma Science*, 41(4):695–700, 2013.

[114] J. P. Sheehan and N. Hershkowitz. *Emissive probes. Plasma Sources Science and Technology*, 20(6):063001, 2011. URL `http://stacks.iop.org/0963-0252/20/i=6/a=063001`.

[115] J. W. Bradley, S. Thompson, and Y. A. Gonzalvo. *Measurement of the plasma potential in a magnetron discharge and the prediction of the electron drift speeds. Plasma Sources Science and Technology*, 10(3):490, 2001. URL `http://stacks.iop.org/0963-0252/10/i=3/a=314`.

[116] P. Balan, R. Schrittwieser, C. Ioniţă, J. Cabral, et al. *Emissive probe measurements of plasma potential fluctuations in the edge plasma regions of tokamaks. Review of scientific instruments*, 74(3):1583–1587, 2003.

[117] L. Schwager. *Effects of secondary and thermionic electron emission on the collector and source sheaths of a finite ion temperature plasma using kinetic theory and numerical simulation. Physics of Fluids B: Plasma Physics*, 5(2):631–645, 1993.

[118] J. Bradley, S. Karkari, and A. Vetushka. *A study of the transient plasma potential in a pulsed bi-polar dc magnetron discharge. Plasma Sources Science and Technology*, 13(2):189, 2004.